Theoretical prediction of τ_E and $\overline{\beta}$ in a large aspect ratio LDX

by
Alexei Kouznetsov
M.S. Physics, Michigan State University (2001)

Submitted to the Department of Nuclear Science and Engineering
in partial fulfillment of the requirements for the degree of
Doctor of Philosophy in Applied Plasma Physics
at the

MASSACHUSETTS INSTITUTE OF TECHNOLOGY
June 2007

Author……
Department of Nuclear Science and Engineering
March 13, 2007

Certified by……
Jeffrey P. Freidberg
Professor of Nuclear Science and Engineering Department
Thesis Supervisor

Certified by……
Jay Kesner
Senior Research Scientist, Physics Research Group Leader, LDX
Thesis Supervisor

Accepted by……
Jeffrey A. Coderre
Professor of Nuclear Engineering
Chairman, Department Committee on Graduate Students

Theoretical prediction of τ_E and $\overline{\beta}$ in a large aspect ratio LDX

by
Alexei Kouznetsov
M.S. Physics, Michigan State University (2001)

Submitted to the Department of Nuclear Science and Engineering on March 13th, 2007
in partial fulfillment of the requirements for the degree of
Doctor of Philosophy in Applied Plasma Physics

Abstract

The Levitated Dipole Experiment (LDX) is a novel experiment to study the confinement of a high-temperature plasma in the magnetic field of a superconducting ring of wire. The levitated magnet produces a poloidal closed-line magnetic field characteristic of an ideal point dipole or a hard core Z-pinch magnetic configuration. The point dipole and hard core Z-pinch configurations share similar physics and may be respectively considered to be the zero and large aspect ratio approximations to LDX. The present work focuses on a hard-core Z-pinch magnetic configuration. An analysis is presented that theoretically predicts (1) the maximum pressure $p_{\max}$, (2) the energy confinement time τ_E and (3) the average beta $\overline{\beta}$ by solving a proposed self-consistent model of plasma. The model makes the optimistic assumption that transport is purely classical in the region of the profile that is magnetohydrodynamically (MHD) stable against interchange modes. For the interchange unstable region, a quasilinear MHD transport model is developed. The analysis of MHD quasilinear transport starts with an assessment of stability corrections due to axial flows. The axial flows are taken as an approximation to the LDX toroidal flows, expected to appear due to non-ambipolar transport. It is shown that the subsonic axial flows create only negligible correction to the plasma stability and the MHD transport analysis is performed for a static plasma. The evolution of the particle density, energy and magnetic field in the MHD unstable region is investigated using the quasilinear approximation. The exact transport equations are derived for a static plasma in the hard core Z-pinch magnetic configuration. The equations are generalized to an arbitrary axisymmetric closed-filed line magnetic configuration. It is shown that violation of the marginal stability criterion leads to a rapid time-scale transport (i.e. much faster than classical transport), which brings the pressure profile back to marginal stability and forces particle density to be inversely proportional to $V \equiv \oint d\ell / B$. The applicability of the quasilinear approximation is numerically tested in a hard core Z-pinch magnetic configuration using a non-linear numerical code. The numerical results confirm the theoretical conclusions that the plasma maintains its marginally stable pressure profile through anomalous transport. The requirement of the marginally stable pressure profile plus $\rho \sim V^{-1}$ density profile completes the model and provides sufficient information to calculate τ_E and $\overline{\beta}$ in the hard core Z-pinch magnetic configuration. The predictions

show that the performance of a large-aspect ratio LDX is strongly coupled to the maximum achievable edge temperature with relatively good performance achieved when $T_w > 10\ eV$. Performance should be further improved by the finite aspect ratio in the real experiment. Analytic and numerical calculations lead to explicit scaling relations for τ_E and $\overline{\beta}$ that can be tested in future LDX experiments.

Thesis Supervisor: Jeffrey P. Freidberg
Title: Professor of Nuclear Science and Engineering Department

Thesis Co-Supervisor: Jay Kesner
Title: Senior Research Scientist, Physics Research Group Leader, LDX

Acknowledgments

A long journey to Ph.D. now comes to a close. Looking forward to start a new chapter of my life, I realize how fortunate I have been to be here. The dynamic and open atmosphere at MIT was the perfect place that gave me an opportunity to broaden the knowledge and open myself to new ideas and perceptions. Along the way I have been fortunate to meet many great people who taught me new skills, gave their support and made my life so much more interesting.

I would like to express my sincerest gratitude to my research advisor Professor Freidberg. Without his support, understanding and the vast knowledge and expertise this work would never have been possible. Above that all, I would like to thank him for his enthusiasm for science and being an unlimited source of inspiration to do a research. That was one of the main reasons why I was always coming back to MIT from my turbulent forays.

I am also extremely grateful to my second advisor, Dr. Jay Kesner. Jay was always available, always ready to listen and help. His knowledge, ideas and help were absolutely crucial from the formulation of a research topic and along the way to the last letter in the thesis itself. Thank you, Jay!

I would like to thank Peter Catto for teaching me fundamentals of plasma transport and giving me with a benchmark of the toughest courses.

Special thanks go to my friends and fellow students at PSFC: Kirill Zhurovich, Antoine Cerfon, Grisha Kogan, Vincent Tang and Natalia Krasheninnikova for their friendship and support.

Finally, I want to thank Marina. I know you can see this and you are happy for me.

This work was supported by the U.S. Department of Energy grant No. DE-FG02-91ER-54109 at the Plasma Science and Fusion Center of the Massachusetts Institute of Technology.

CONTENTS

List of Figures

Chapter 1

1 Introduction

The motivation behind this work is the continuing operation of the Levitated Dipole Experiment (LDX) at the Massachusetts Institute of Technology. LDX has been built by Columbia University and MIT to investigate the physics of plasmas contained in a closed-field line magnetic configuration, such as a dipole configuration. The LDX plasma is confined in the closed field line poloidal magnetic field produced by a superconducting ring of wire carrying current up to 1.3MA.

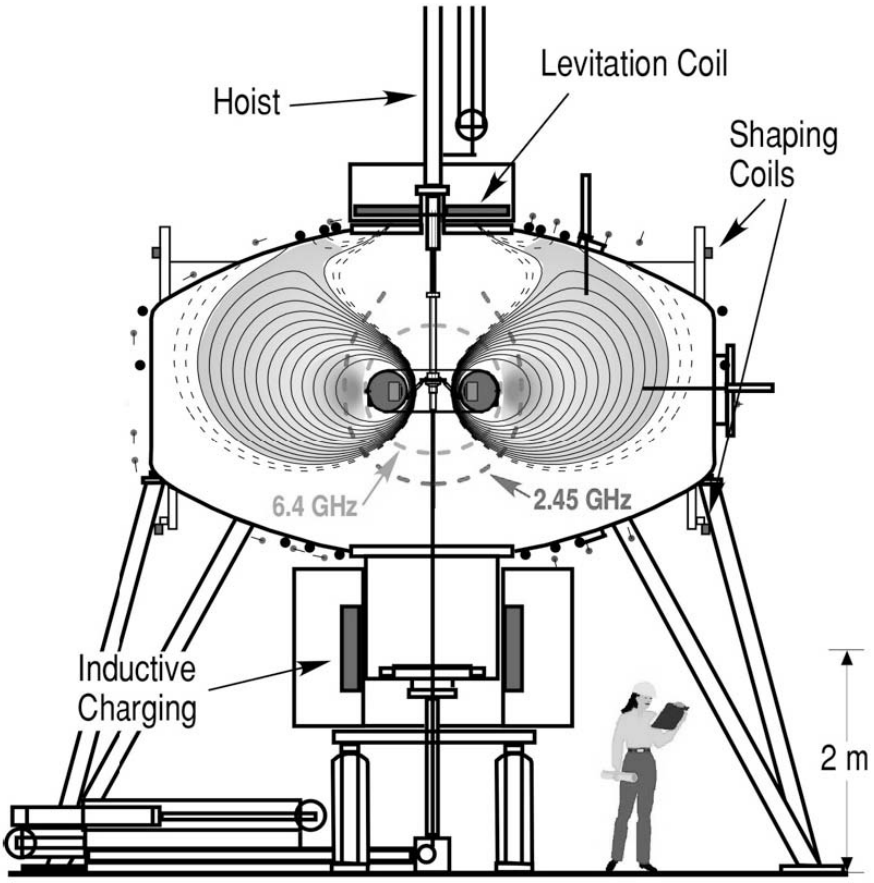

Figure 1-1 A schematics of the Levitated Dipole Experiment

LDX is shown schematically in Fig. 1.1. It has a magnetic coil levitated inside a vacuum vessel of radius of about 2.5m [1]. Up to date, all LDX experiments have been conducted in the ”supported mode”, where the coil is mechanically supported by the launcher. The losses on the support structure made experiments with a high-density plasma impossible. Instead a low-density plasma is created which is characterized by high anisotropy and consists of three clearly defined species: cold background ions, cold electrons and hot electrons.

The levitated experiments, scheduled to start in the spring of 2007, will open an opportunity to study the confinement of an isotropic high-density magnetohydrodynamic (MHD) plasmas in a closed-field line configuration, and it is anticipation of these experiments that provide the motivation for this work.

The present study has as one of its major goals the derivation of an equivalent to the “empirical” scaling relation used by tokamak community to predict the energy confinement time τ_E at given values of experimental parameters.

To put the problem in perspective recall that the tokamak community has been working for decades to obtain a first principles understanding of anomalous heat transport, an effort that has only recently come close to fruition. With a much newer and much smaller program one might ask how the LDX community expects to achieve the same end goal in such a short time. The answer is that in some ways the LDX physics, although anomalous, is simpler than that of the tokamak. Specifically, tokamaks typically operate in a regime that is MHD stable and the anomalies are due to weaker instabilities such as the ion temperature gradient mode, the electron temperature gradient mode, and the trapped electron mode [2]. The operation of a tokamak close to MHD

"Troyon stability limit" is inherently dangerous experimentally due to potential plasma disruptions and is very limiting on large, next generation machines such as ITER.

The stability of the levitated dipole on the other hand will likely be dominated by the stronger MHD interchange mode. It will be shown later that the violation of MHD stability limit will likely produce a "soft-landing", thereby safeguarding the machine against violent plasma disruptions. Therefore a simpler model, accompanied by a simpler analysis may hopefully lead to a reasonably accurate prediction in a relatively short time.

The thesis is based on the physics of the one-fluid collisional MHD model. All kinetic and electrostatic modes are omitted. In addition, we have assumed that the plasma adiabatic condition is valid with the standard adiabatic constant $\gamma = 5/3$. Even with the significant simplification of focusing only on the strongest instabilities, the creation of the self-consistent plasma model and subsequent calculation of the energy confinement time is a challenging problem. To further simplify the problem, the calculations of the energy confinement times τ_E and average beta $\overline{\beta}$ have been carried out in the cylindrical jhard core Z-pinch geometry. A hard core Z-pinch magnetic geometry a simple closed-field line magnetic configuration that can be considered to be a large aspect ratio approximation to LDX. Both configurations have the interchange mode as the dominating restriction on the stability of plasma, though the geometrical differences may lead to quantitative differences in the numerical predictions.

However, before attempting the calculations of τ_E and $\overline{\beta}$, several other important steps have to be performed. It is well known that a static (i.e. $\mathbf{v} = 0$) closed field line configuration, such as a levitated dipole, or a hard-core Z-pinch, can be stabilized against ideal interchange modes when the edge pressure gradient is sufficiently weak. The stabilizing effect is provided by plasma compressibility. However, many laboratory

plasmas exhibit a sheared velocity flow, (i.e. $\mathbf{n}\cdot\nabla\mathbf{v}\neq 0$), and this flow may affect the marginal stability boundary. The LDX is expected to develop toroidal flows either due to the natural electrostatic bias of the coil or due to non-ambipolar transport effects. The first step in creating self-consistent MHD stable plasma profiles requires addressing the issue of the stability with sheared toroidal flows. Towards this goal we analyze the effect of axially sheared flow on the ideal MHD stability limit of the interchange ($m=0$) mode in a hardcore Z-pinch. Specifically, the goal is to learn whether sheared flow is favorable, unfavorable, or neutral with respect to MHD stability.

Analytic calculations of marginal stability for several idealistic velocity profiles in the slab limit show that all three options are possible depending on the shape of the shear profile. This variability reflects the competition between the destabilizing Kelvin-Hemholtz effect and the fact that velocity shear makes it more difficult for interchange perturbations to form at short wavelengths. Numerical calculations have been presented for more realistic experimental profiles and compared with the results for the idealized analytic profiles. The numerical results were used to predict the change in critical β due to realistic velocity shear profiles. It was found that to generate noticeable changes in the stability limits and resulting β, the flow must have a specific profile shape and be supersonic. While it is conceivable that the LDX toroidal flows could be large, they are unlikely reach supersonic speeds. Hence, for the most of this work we neglect flow effects and develop the MHD quasilinear transport model for a plasma without a background flow.

The MHD stability limit of a static plasma is easily calculated with linear theory. Linearized MHD equations allows us to calculate both the stability boundary and to find the growth rate of the unstable modes when the marginal stability criteria is violated. At

the same time, to achieve the optimal performance of the machine, it is desirable to operate the machine close to marginal stability limit. The heating evolution, impurities or random fluctuations can push the system beyond the stability boundary. While there exists a good knowledge of the stability limits, understanding of the dynamics of the unstable system is sketchy at best. It is well known that the excitations of MHD unstable modes often leads to a violent restructuring of the plasma profiles and may cause a complete loss of plasma.

The typical approach to understand the behavior of an unstable system includes detailed, often time consuming numerical simulations to track the evolution of the system on the Alfven time scale. An alternative approach, employed in this study, is to create an analytical model, which predicts the energy and particle transport of a plasma in the region weakly unstable to the interchange mode.

To do this we employ a quasilinear approximation to derive transport equations in this region. We show that a violation of the marginal stability condition leads to quasilinear time scale transport, which is must faster than classical transport but slower than the ideal MHD growth time. The end result of the quasilinear transport is to bring the pressure profile back to its marginal stability form and to force the particle density to be inversely proportional to $V(\psi) \equiv \oint d\ell / B$.

The calculations were initially performed for the hard core Z-pinch geometry and later generalized to an arbitrary axisymmetric closed field line configuration. The quasilinear transport model, applicable in the interchange unstable region of plasma, and the MHD model with Braginskii classical collisional terms used in MHD stable region, are connected across the stability-instability boundary to complete the self-consistent model of plasma.

It is important to note that the self-consistent model of plasma does not include potentially unstable electrostatic and kinetic modes in the MHD stable region. The only transport allowed in the region of good magnetic curvature is the classical cross-field conduction, which is an optimistic assumption.

Based on this self-consistent model, we have numerically calculated τ_E and $\overline{\beta}$ for a hard-core Z-pinch magnetic configuration at values of the experimental parameters close to those expected in LDX. As the last step, an explicit "empirical" scaling relation for the hard-core Z-pinch magnetic configuration has been obtained by repeating numerical experiments for different values of externally changeable parameters, such as coil current, particle density, location and power of the heat source, etc.

The resulting scaling relations show reasonably good performance of the large aspect ratio LDX at the expected experimental parameters, but only if the edge temperature can be maintained at a reasonably high level - $T_{wall} \sim 10 - 100\ eV$. The quasilinear transport model also shows that a closed-field line system is unlikely to experience violent plasma disruptions. Instead all excess energy should be transported away by increased anomalous transport.

Here the predictions are similar to the results of earlier non-linear numerical simulations by several authors [3-4], though the quasilinear transport remains a more desirable mechanism for energy transport. Our attempts to numerically demonstrate which type of the transport (quasilinear or non-linear) is prevalent in the unstable plasma does produce conclusive results due to inherent difficulties in the numerical codes to capture microturbulence dynamics. However, it is shown that both transport mechanisms lead to identical plasma profiles in the MHD unstable region of the plasma. Both models show that the plasma is safeguarded against disruptions.

On the other hand, the quasilinear model and resulting “empirical” scaling relations raise concerns with respect to the inefficient use of heating beyond a certain, relatively low power of the heating source. Specifically, the model shows that in LDX most of the power above 1-3kW will be lost by quasilinear transport and is therefore unlikely to contribute to an improvement in machine performance.

Also, the results of the study question the sustainability of ECRH heating for high particle density. The quasilinear model demonstrates the build up of the particle density in the plasma core that would lead to a shut down of the ECRH heating even for very modest densities at the chamber wall.

Even so, our results show that relatively good performance of the hard-core Z-pinch version of LDX should be possible assuming that reasonably high edge temperatures can be maintained experimentally. Performance should be further improved by the tight aspect ratio and bigger compression factor of the real experiment.

The thesis is organized as follows: the second chapter contains a brief overview of the historical motivation behind the LDX experiment, the recent experimental results and an overview of the key concepts. Chapter 3 presents an analysis of the effect of axial flows on the stability of the interchange mode in a hard-core Z-pinch. Particularly, we have derived the full eigenmode equation for the interchange mode in a hard core Z-pinch magnetic configuration with axial flows. The eigenmode equation is simplified to a slab geometry limit and then analytically solved to obtain marginal stability criteria for several idealized velocity profiles.

The intuition generated in slab calculation is used to interpret the numerical results for the more realistic velocity profiles in the cylindrical geometry. Chapter 4 contains the derivation of the quasilinear transport model for a static unstable plasma in a hard core Z-

pinch and general axisymmetric closed-field line configuration. A simple procedure is described that shows how to connect the quasilinear transport model in the unstable portion of the profile to the stable region of plasma described by classical transport. The resulting self-consistent plasma profiles across the whole plasma volume are also discussed. The last topic discussed in Chapter 4 involves non-linear numerical simulations of a hard-core Z-pinch plasma. We show the "self-organization" process of the plasma profiles after the excitation of the interchange mode and show the difficulty of demonstrating whether the quasilinear or non-linear anomalous transport is prevalent in the plasma.

Chapter 5 analyzes in detail the self-consistent model for the hard core Z-pinch plasma profiles in both stable and unstable regions. To create benchmarks we run several reference cases, comparing the results for purely classical conduction energy transport, Bohm diffusion, and quasilinear diffusion transport. At the end of Chapter 5, the self-consistent quasilinear diffusion model equations are solved numerically to obtain τ_E and $\overline{\beta}$ for various plasma parameters. The resulting "empirical" scaling relations represent the major practical result of this work. The last chapter summarizes the results of previous chapters, discusses the implications of the scaling relations and other findings for the LDX experiment, and suggests the venue for future research.

Chapter 2

2 The LDX experiment

2.1 Historical motivation and the key concepts

The dipole magnetic field is the simplest and most common magnetic configuration in nature. Most of celestial objects have internally generated magnetic fields that look like the field of a circular current loop. The Voyager-2 experiment helped to amass huge amount of data on the behavior of the plasma in the magnetosphere of the planets and thus helped to increase the interest in the confinement properties of a dipole magnetic field.

The initial idea behind the Levitated Dipole Experiment is attributed to Akira Hasegawa, who was the first to propose a laboratory experiment involving dipole plasma confinement [1]. Hasegawa recognized that the inward diffusion and adiabatic heating that accompanied strong magnetic and electric fluctuations in planetary magnetospheres represented a fundamental property of strongly magnetized plasmas not yet observed in laboratory fusion experiments.

The proposed laboratory experiment should have the dipole field generated by the superconducting ring of wire, magnetically levitated in the vacuum chamber in order to avoid spurious contact with any support structure. Unlike tokamaks, where the confinement is provided by a carefully chosen magnetic shear profile, the key confinement property of the dipole field is plasma compression. The dipole confinement

concept is based on the idea of generating pressure profiles near marginal stability for low-frequency magnetic and electrostatic fluctuations.

In the ideal MHD framework, marginal stability requires the plasma pressure to fall off gradually in the outer portion of the plasma. The pressure *p* must satisfy the adiabatic condition, $pV^{\gamma} = const.$, where V is the differential flux tube volume ($V = \oint dl / B_p$) and $\gamma = 5/3$. This condition leads to a pressure profile that scales with radius as $p \propto r^{-20/3}$ in a toroidal dipole and $p \propto r^{-10/3}$ in a cylinder. The toroidal result is similar to the energetic particle pressure profiles observed in the Earth's magnetosphere.

However, one clear advantage of the LDX experiment, as compared to a planet's magnetosphere, is the absence of losses to magnetic poles. This may lead to potentially good energy confinement times and high temperatures in the plasma core. Additionally, the absence of the magnetic shear allows the formation of the convective cells, which may give rise to unique ways of advance fueling and ash removal.

The earlier studies supported the possibility of creating a dipole-based fusion reactor that utilizes D-He3 advanced fuel to reduce the energy of neutrons bombarding the superconducting magnet [2,3]. More recent studies have demonstrated that D-D fuel would be more efficient in powering the self-sustaining fusion reaction [4].

The simple and elegant dipole approach must face serious technical challenge- the requirement to levitate the superconducting ring within a high temperature plasma environment. Advances in high temperature superconductors coupled with an innovative design concept due to Dawson [5] on the maintenance of an internal superconducting ring in the vicinity of a fusion plasma led to the belief that this issue is technologically

solvable. These considerations motivated the construction of LDX, a joint project by Massachusetts Institute of Technology and Columbia University, started in 1998.

2.2 LDX overview

The LDX consists of three superconducting coils and a large vacuum vessel (Fig 1.1). The vacuum vessel is made of stainless steel and has a radius of approximately 5 m, with an internal volume of $\sim 80m^3$. The three superconducting coils are the floating coil (F-coil), the charging coil (C-coil) and the levitating coil (L-coil). The floating coil is the levitated magnet that produces the dipole-like magnetic field. The doughnut-shaped F-coil has a major radius of about 40cm and an outer radius of 58.5 cm. The magnet can carry up to 1.5 MA current and produce a peak magnetic field in plasma of greater than 3 Tesla. Due to it's innovative heat shielding design [6,7] the floating coil can withstand significant heat flux and remain superconducting for more than 2 hours.

At the beginning of the experiment the floating coil is charged by a large charging coil, located at the bottom of the vacuum vessel. As the floating coil is charged, it is cooled with the liquid helium to trap the magnetic flux going through the F-coil. Both floating and charging coils are traditional low-temperature superconducting magnets. The charged floating coil is raised by the mechanical launcher to the middle of the vacuum vessel and is then levitated by the levitating coil. The L-coil, located on the top of the vessel, creates the magnetic filed necessary to levitate the F-coil. The current in the L-coil is controlled by a feedback system measuring the exact location of the F-coil. In addition, there are several Helmholtz coils used to correct the shape of the magnetic flux surfaces, as illustrated in Fig. 2.1.

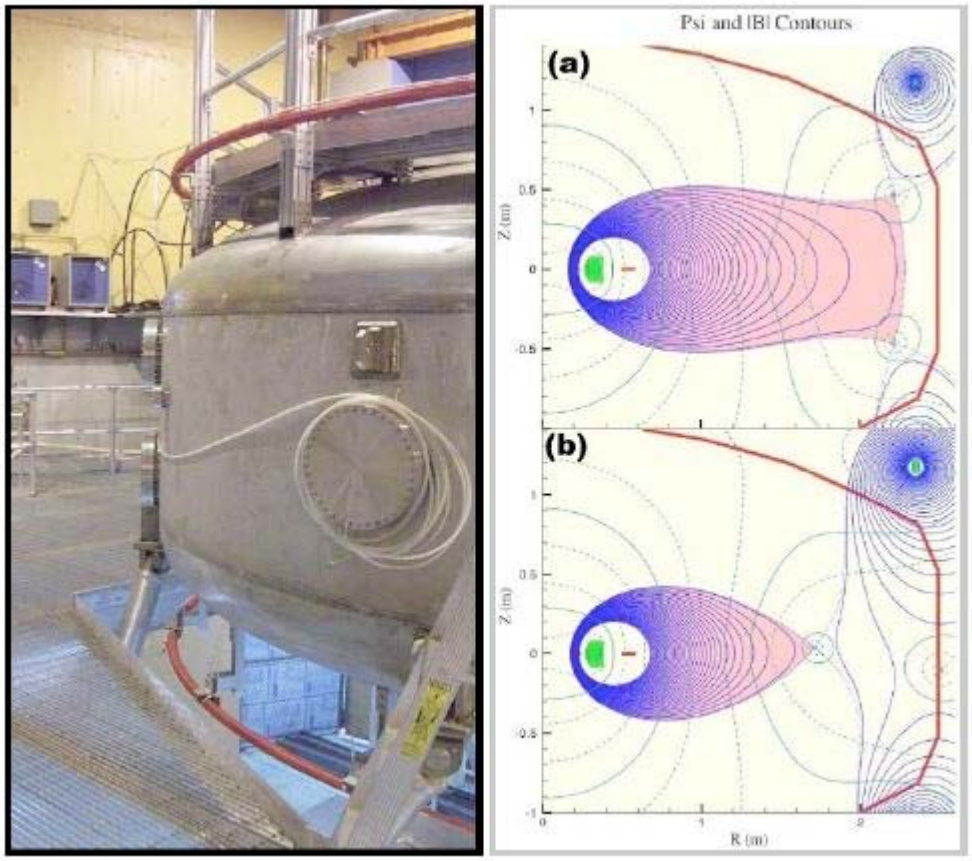

Figure 2-1[1] LHS- The LDX Helmholtz coils are shown above wrapped in red tape. RHS- The magnetic geometry for a Helmholtz field created with (a) 30 kA turns and (b) 50 kA turns.

The resulting system has purely poloidal magnetic field with an upper null point and can contain up to 30 m^3 of plasma. The plasma is heated by electron cyclotron resonance heating (ECRH) at heating frequencies of 2.45GHz and 6.4GHz. The LDX team is working to add a 28GHz gyrotron to compliment the lower frequency sources of energy. The multiple energy sources will give the flexibility to run experiments with different input energies and locations of the heating sources [8-9]. The first LDX plasma experiments started in August of 2004, following 5 years of constructions.

[1] Courtesy of the LDX team.

2.3 Theoretical research and recent experimental results

A dipole fusion confinement concept was initially presented in "A white paper for the fusion community" in April of 1998 [10]. It was immediately recognized that, as with any other magnetic configuration, MHD stability poses the most important restriction on the potential macroscopic operation of any future experiment. Garnier, Kesner and Mauel investigated the MHD stability of the levitated dipole in 1999 [11]. They found a high-beta LDX equilibrium stable to interchange modes and demonstrated that this equilibrium was stable as well to all ballooning modes.

Later that year Kesner analyzed the electrostatic interchange mode in a collisional plasma and came to the conclusion that the optimal pressure profile is achieved when the temperature gradient parameter $\eta = d\ln T / d\ln n$ is equal to 2/3[12]. In a later study, Kesner and Hastie found a strong dependence on the stability of electrostatic drift waves on the parameter η [13]. It had been pointed-out earlier that a plasma that satisfies the MHD interchange stability requirement may be intrinsically stable to drift waves [14].

These calculations were performed for the real LDX geometry, which differs from the approach adopted by Krasheninnikov, Catto and Hazeltine [15-16]. Krasheninnikov *et. al*. have investigated and derived a series of equilibria for the ideal point magnetic dipole. On the basis of one of these equilibria, Simakov, Catto *et. al.* showed that the ideal point dipole is always stable to ballooning modes [17] and also investigated the kinetic and resistive stability of a magnetic dipole and other axisymmetric closed field line configurations [18, 19]. They have shown that the resistive mode in the ideal MHD stable plasma has a weak growth rate and exists only in the toroidal dipole geometry. For a hard core Z-pinch configuration, the ideal modes always dominate resistive instabilities.

While there exists a large body of research on the MHD stability boundary, the understanding of the dynamics of the unstable LDX plasma is very limited. Following the study by Pastukhov and Chudin [20] for a hard core Z-pinch, J. Kesner has adapted the set of reduced MHD equation for low-beta LDX plasma and found a special time-independent solution with convective cell structure [21].

More recently, N. Krasheninnikova and Catto have studied the effects of hot electrons on the stability of a toroidal dipole plasma [22]. They have found that hot electrons modify the classical MHD interchange stability condition due to a weak drift resonance with the slowly moving hot electrons.

The experiments have not yet confirmed or refuted most of the theoretical predictions described above. At the time of this writing, all plasma experiments have been performed in the "supported mode". The three spokes, supporting the F-coil behave like a sink of energy and plasma particles. Since the plasma can flow freely along the magnetic lines, even the smallest toroidal flows lead to significant parallel losses. The remaining plasma has a very low particle density and a high level of anisotropy. The low particle density leads to a low collisionality regime and a corresponding separation of the plasma into three distinctive species: cold ions, cold electrons and hot electrons. Indeed, the latest experiments show that the reconstructed pressure has a high anisotropy factor $p_{\perp} / p_{\parallel} \sim 5$[23]. The hot electrons provide a large portion of the pressure and the particle density of the hot species is $n \sim 10^{16} m^{-3}$.

Confirming the predictions of Krasheninnikova and Catto [22], the LDX team has clearly observed the hot electron interchange instability. However, the predictions of other theoretical studies described in this chapter can be verified only in the levitated experiments, which are scheduled to start in the spring of 2007.

Levitation of the F-coil should eliminate parallel losses and make the plasma more isotropic. The MHD one-fluid model, valid for isotropic high-collisional plasmas, would then provide a relatively accurate description of the underlying physics. The levitated experiments are expected to demonstrate a much higher plasma temperature and the LDX team will then face the question of improving the energy confinement time, a critical parameter for any fusion experiment.

This raises the question of scaling the confinement time as a function of the experimentally controlled parameters and machine properties. The tokamak community uses empirically obtained scaling relations to calculate the expected τ_E and $\overline{\beta}$ at given values of experimental parameters. This thesis has as a primary goal the construction of similar "empirical" scaling relations using numerical experiments with the self-consistent quasilinear model of the LDX plasma. The approach and steps to obtain an "empirical" scaling relation for the large aspect ratio LDX model will be described in the next three chapters.

Chapter 3

3 Effect of the sheared axial flows on the stability of a hard-core Z-pinch[2]

3.1 Introduction

The goal of this chapter is to theoretically investigate the effect of sheared axial flow on the magneto-hydro-dynamical (MHD) stability of a closed line configuration. The motivation is as follows. The toroidal LDX configuration can be modeled theoretically as a cylindrical hardcore Z-pinch. It is well known [3] that a simple Z-pinch without an equilibrium flow (i.e. $\mathbf{v} = 0$) is potentially unstable to two MHD modes - the $m = 1$ helical mode and the $m = 0$ interchange mode. The hardcore stabilizes the $m = 1$ mode. In a closed line configuration the $m = 0$ interchange mode (i.e. the sausage instability) can be stabilized by a sufficiently weak pressure gradient near the edge of the column. The maximum allowable pressure gradient directly sets the β limit of the plasma, whose value is critical to the ultimate viability of the concept.

However, many laboratory plasmas exhibit a substantial equilibrium sheared velocity flow, (i.e. $\mathbf{n} \cdot \nabla \mathbf{v} \neq 0$) and it is believed that LDX may develop substantial toroidal flows. The flows may be originated by the natural bias of the floating coil or due to non-ambipolar transport. This flow may affect the $m = 0$ marginal stability boundary, and hence the maximum value of β. The present chapter directly addresses this issue by an

[2] A significant portion of this chapter is reused from A. Kouznetsov *et. al.*, Physics of Plasmas, **14**, 012503 (2007). Copyright 2007, American Institute of Physics. Permission license number 1647250065654

analysis of the effect of axially sheared flow on the ideal MHD stability limit of the $m = 0$ mode in a hardcore Z-pinch. Specifically, the goal is to learn whether sheared flow is favorable, unfavorable, or neutral with respect to MHD stability. Analytic calculations of marginal stability for several idealistic velocity profiles in the slab limit show that all three options are possible depending on the shape of the shear profile. This variability reflects the competition between the destabilizing Kelvin-Hemholtz effect and the fact that shear makes it more difficult for interchange perturbations to form at short wavelengths. Numerical calculation are presented for more realistic experimental profiles and compared with the results for the idealized analytic profiles. The numerical results are also used to predict the change in critical β due to realistic velocity shear profiles.

The effects of flow on MHD stability have been studied for many years and as such it is useful to review some of the most relevant studies to put the present work in perspective. As is well know the highly desirable property of self-adjointness in the linear stability equations vanishes when flow is included [4]. This has caused a large part of the effort to focus on simple geometries such as a slab or cylinder. Even then, the resulting problems remain quite complicated mathematically, often requiring numerical solutions for the eigenvalues and eigenfunctions.

Some early studies involved the effect of rotation on a pure θ-pinch. Taylor [5] showed that centrifugal effects could drive rotational instabilities for $m \geq 2$ modes for $k_{\|} = 0$, presumably the worst mode in terms of minimizing the stabilizing effects of line bending. Freidberg and Wesson [6] showed the counter-intuitive result that $m = 1$ could also be driven unstable, but only for a finite, non-zero value of $k_{\|}$. This unexpected result arose from the non-self adjointness of the MHD force operator. A similar situation arises in the present work.

Several authors have investigated the effect of sheared axial flow on a general screw pinch. Bondeson, Iacono and Bhattacharjee [7] studied the effects of flows on the Suydam criterion. They found that the flow decreases the maximum stable pressure gradient. E. Hameri [8] came to the similar conclusions using analytical approximations.

The effect of toroidal rotation on the stability of ballooning modes was considered by E. Hameri and P. Laurences [9] in mid the mid-80s. They found that the toroidal rotation had a destabilizing effect on the plasma β limit . However, ideal ballooning modes are of limited interest to LDX because of the absence of magnetic shear [10,11]. They do not exist in a cylindrical Z-pinch.

Recent interest in Z-pinch plasmas has led to several numerical studies of the stability of plasmas with sheared flows. V. Sotnikov et al [12] and Zhang and Ding [13] showed that supersonic flows could decrease the growth rate of macroscopic perturbations. Also, partial stabilization of the plasma column by axial sheared flows was reported by Desouza-Machado, Hassam and Ramin Sina[14]. The Rayleigh-Taylor instability, a close analog of the interchange instability, has also been of interest to the geophysics community. Kuo [15] in 1963 and Guzdar *et. al.*[16] in 1982 found that velocity shear decreases the growth rate of the Rayleigh-Taylor mode and showed that unlike the static case, the most unstable wavenumber is finite. An analytic slab geometry calculation carried out by A.Hassam[17] demonstrated that velocity shear decreases the growth rate of the Rayleigh-Taylor instability and non-linearly positively stabilizes marginally stable profiles. In a similar calculation Hassam [18] also showed that for the short wavelength interchange mode in an elongated plasma, sheared flows stabilize the plasma.

At the same time the introduction of sheared flows may give rise to KH (Kelvin-Helmholtz) instability [19]. Experimental observations and the relative importance of the

KH mode versus flow shear stabilization near a plasma limiter were reported by Brochard et al [20]. Many previous studies, often motivated by short-lived Z-pinches, typically concentrated on the effect of sheared flows on highly unstable plasma profiles, but did not consider the effect of an axial flow on weakly unstable or marginally stable plasma pressure profiles.

The net result is that while considerable progress has been made, at the present time there is no clear and unique understanding of whether or not an axial sheared flow would be favorable, unfavorable, or neutral with respect to the important question of β limits in a hardcore Z-pinch, modeling the LDX configuration. This is the main objective of the present chapter.

The chapter is organized as follows: In Section 2 the standard second order radial eigenvalue equation for the m = 0 interchange mode in a static Z-pinch is modified to include non-zero axial flows. In Section 3 we consider the slab limit of the LDX configuration. Section 4 presents an analytical derivation of new local stability criteria for several idealistic velocity shear profiles. In section 5 we return to the cylindrical geometry and present numerical calculations, which determine the stability boundaries using more realistic experimental profiles for the plasma pressure and the flow velocity.

3.2 Eigenmode equation for a general Z-pinch with an axial flow

This section discusses the eigenvalue equation for a cylindrical screw pinch configuration, including an axial flow. The starting point is the ideal MHD model

$$\frac{\partial \rho}{\partial t} + \nabla \cdot (\rho \mathbf{v}) = 0$$
$$\rho\left(\frac{\partial \mathbf{v}}{\partial t} + \mathbf{v} \cdot \nabla \mathbf{v}\right) = \mathbf{J} \times \mathbf{B} - \nabla p$$
$$\frac{d}{dt}\left(\frac{p}{\rho^{\gamma}}\right) = 0 \qquad (3.1)$$
$$\nabla \times \mathbf{B} = \mu_0 \mathbf{J}$$
$$\frac{\partial \mathbf{B}}{\partial t} = \nabla \times (\mathbf{v} \times \mathbf{B})$$

The non-trivial quantities entering the analysis are as follows: the pressure $p = p_0 + p_1$, the magnetic field $\mathbf{B} = B_{0\theta}\mathbf{e}_\theta + B_{0z}\mathbf{e}_z + \mathbf{B_1}$, and the axial velocity $\mathbf{v} = V_0\mathbf{e}_z + \mathbf{v_1}$. Here all equilibrium quantities are functions only of r [i.e. $Q_0 = Q_0(r)$] and all perturbed quantities have the standard normal mode dependence $Q_1 = Q_1(r)\exp\left[i\left(-\omega t + m\theta + kz\right)\right]$. For simplicity the "zero" subscript is hereafter suppressed on all equilibrium quantities. Note that with an axial flow the eigenvalue ω is in general complex. The next step is to introduce the displacement vector $\boldsymbol{\xi}$, defined as $\mathbf{v}_1 = -i\omega\boldsymbol{\xi} + \mathbf{V} \cdot \nabla\boldsymbol{\xi} - \boldsymbol{\xi} \cdot \nabla\mathbf{V}$. Following the usual MHD stability procedure [21] it is straightforward to show that the full eigenmode equation for the general screw pinch in the presence of an axial flow has exactly the same form as without flow if we make the formal substitution $\omega \to \omega - kV(r)$.

The general eigenvalue equation reduces considerably for interchange modes in a hard-core Z-pinch. The simplified equation is obtained by setting $B_z(r) = 0$ and $m = 0$. Also, further simplification arises by making the well satisfied approximation that the unstable eigenvalues of interest are much smaller in magnitude than the compressional Alfven frequency: $|\omega| \ll kV_A$. This assumption prohibits very short wavelengths. (i.e. $k^2r^2 \geq \beta$).

The assumption is necessary to simplify the inertia term $\frac{\rho(\omega - kV)^2}{r}\xi$, which has a small correction inversely proportional to $k^2 r^2$. Given that the interchange instability can develop only in a region of bad curvature, where the coordinate r is typically large, the condition $k^2 r^2 \geq \beta$ is easily satisfied. Under these assumptions the final eigenmode equation is given by

$$\frac{d}{dr}\left[\frac{\rho}{k^2 r}(\omega - kV)^2 \frac{d\psi}{dr}\right] + \frac{\rho}{r}\left[\omega_S^2 K - (\omega - kV)^2\right]\psi = 0 \tag{3.2}$$

where $\omega_S^2(r) = 2V_s^2 / r^2$, $V_S^2(r) = \gamma p / \rho$ is the square of the adiabatic sound speed,

$$K(r) = \frac{rp'}{\gamma p} + \frac{2B_\theta^2}{B_\theta^2 + \gamma \mu_0 p} \tag{3.3}$$

is the Kadomtsev stability function [3] and $\psi = r\xi_r(r)$ is proportional the radial component of the perturbation. Kadomtsev showed that $K(r) > 0$ is a necessary and sufficient local stability criterion against the $m = 0$ interchange mode for static equilibrium.

The appropriate boundary conditions on Eq. (3.3) require that the function ψ vanish at the plasma boundaries.

$$\psi(r_c) = \psi(r_w) = 0 \tag{3.4}$$

Here, r_c is the radius of the hard core and r_w is the radius of the outer shell. See Fig.1. The usual experimental situation has $r_w \gg r_c$.

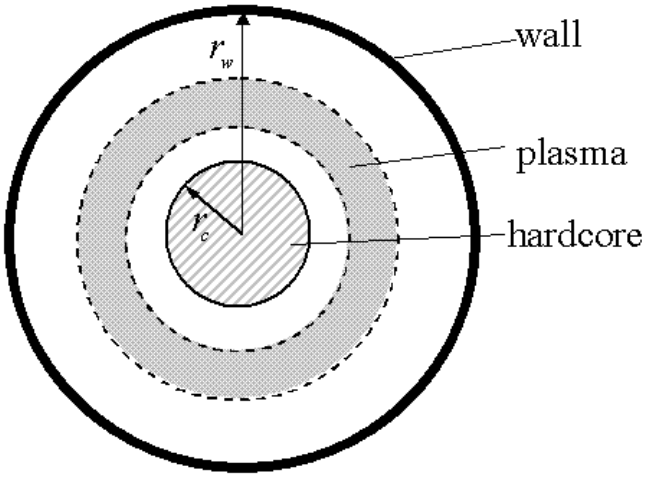

Figure 3-1 Hardcore Z-pinch model of LDX

The normal mode approach requires solving equation (2) subject to the boundary conditions given by Eq. (3.4) for given plasma and velocity profiles. The full solution for arbitrary profiles can only be found numerically.

This section closes with an interesting suggestive, but misleading intuition, about the effect of flow on stability resulting from a quadratic integral relation obtained by multiplying Eq. (3.2) by $\psi *$ and averaging over the plasma volume. The requirements that both real and imaginary parts vanish yield the following expression for the growth rate ω_i: $\omega_i^2 = -\left\langle \omega_s^2 K \right\rangle_0 + \left\langle k^2 V^2 \right\rangle_1 - \left\langle kV \right\rangle_1^2$. Here

$$\left\langle Q \right\rangle_n = \frac{\int Q(\rho/r)\left(n|\psi'|^2 + k^2|\psi|^2\right)dr}{\int (\rho/r)\left(|\psi'|^2 + k^2|\psi|^2\right)dr} \tag{3.5}$$

Clearly the condition for stability is given by

$$\left\langle \omega_s^2 K \right\rangle_0 \geq \left\langle k^2 V^2 \right\rangle_1 - \left\langle kV \right\rangle_1^2 \tag{3.6}$$

Note that for uniform or zero axial flow the right hand side of Eq. (3.6) vanishes and the stability criterion is reduced to that given by Kadomtsev. When there is shear in the flow,

Schwartz's inequality implies that the right hand side is always positive. The implication would seem to be that it is now more difficult to achieve stability and therefore flow shear is always destabilizing. This conclusion is not correct for the following reason. Since the problem is not self-adjoint the Energy Principle does not apply. Thus, while substituting the eigenfunction for the static case into Eq. (3.5) as a trial function suggests a more unstable situation, there is no guarantee that the actual eigenvalue is always approached from the stable side of the spectrum. In fact, in certain important examples discussed shortly it is found that just the opposite occurs, demonstrating that velocity shear can be a stabilizing effect in spite of misleading intuition generated by Eq. (3.6).
In the next section we derive a slab geometry approximation that leads to an analytically solvable equation.

3.3 The slab geometry model

The counter intuitive effect just described as well as a more general view of the effects of flow shear can be obtained by taking a simple slab limit of the eigenvalue equation, which allows an analytic solution. The slab limit is somewhat artificial with respect to the actual experimental situation in LDX but still makes good sense physically. The limit is obtained by assuming the hard-core radius and outer boundary surface are close to one another so that the plasma resembles a thin shell. Specifically, we assume that $(r_w - r_c)/(r_w + r_c) \ll 1$. We then expand $r = r_0 + x$ where $r_0 = (r_c + r_w)/2$. The range of the new independent variable x is defined by $-a \le x \le a$ where $a = (r_w - r_c)/2$ and $a \ll r_0$. The eigenvalue equation reduces to

$$\frac{d}{dx}\left[\left(V_p - V\right)^2 \frac{d\psi}{dx}\right] + \left[\omega_S^2 K - k^2\left(V_p - V\right)^2\right]\psi = 0 \qquad (3.7)$$

where $V_p = \omega / k$ is the phase velocity, $\omega_S^2 = \omega_S^2(r_0) = 2V_S^2(r_0)/r_0^2$ and $V = V(x), K = K(x)$ are the spatially varying velocity and Kadomtsev profiles. Introducing $\psi(x) = U(x)/(V - V_p)$, leads to the final desired form of the slab eigenvalue equation:

$$U'' - \left[k^2 - \frac{\omega_S^2 K}{(V - V_P)^2} + \frac{V''}{V - V_p} \right] U = 0 \tag{3.8}$$

In the next section this equation is solved analytically for several idealistic velocity profiles to determine the effect of sheared axial flow on marginal stability.

3.4 Marginal stability for the slab model

Equation (8) can be solved analytically for a variety of profiles consisting of constant and linear velocity segments. The case of a purely constant velocity is uninteresting. It does not change the self-adjointness of the MHD force operator and the stability analysis immediately reduces to that of the static case by the introduction of a Doppler shifted frequency.

The more interesting cases considered treat three specific velocity profiles, each with axial shear: (a) a constant shear velocity profile, (b) a triangle-shaped velocity profile with velocity shear positive in one region and negative in the other and (c) an “S” shaped profile where the shear is constant in a narrow region and connects to constant velocity regions at each edge with equal but opposite sign velocities. For each of these models the full dispersion relation is derived leading to a determination of the marginal stability criterion.

3.4.1 The case of constant velocity shear

This configuration models the situation where the Kadomtsev function is negative (i.e. $K < 0$) over a narrow region of the plasma (i.e. is destabilizing) and the velocity shear is a smooth function over this region. An illustration of the smooth cylindrical profiles and the corresponding slab approximation is shown in Fig. 3-2.

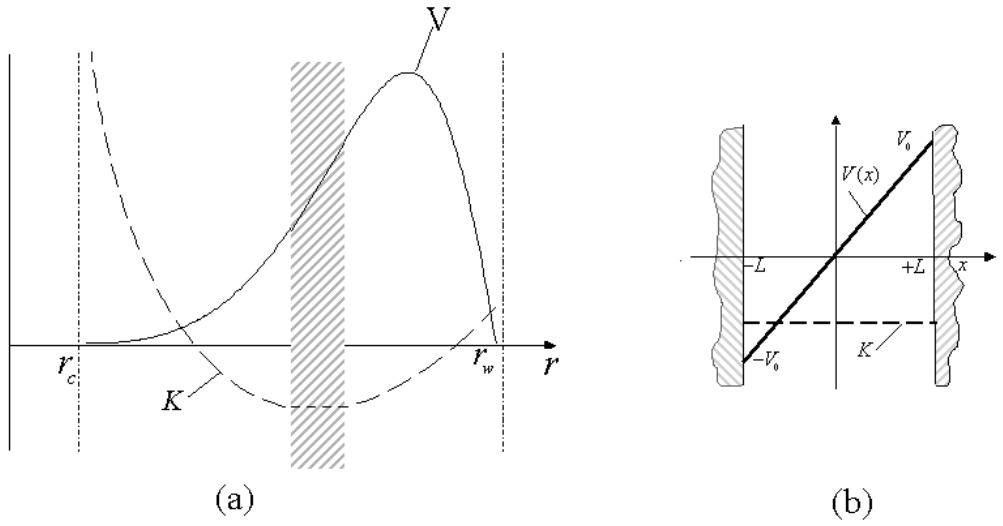

Figure 3-2 (a) Cylindrical model showing constant velocity shear near $K = K_{\min}$ (b) it's slab approximation

The slab model is further simplified by assuming that $-K_{\max} / K_{\min} \gg 1$ with $K_{\max} > 0$ and $K_{\min} < 0$. In this limit the outer solutions in the regions $L < |x| < a$ decay very rapidly, a behavior that is accurately approximated by modifying the boundary conditions such that $\psi(-L) = \psi(L) = 0$ where $L^2 \approx -K_{\min} / K''_{\min}$. As is shown shortly the marginal stability boundary is independent of L. For this model we assume that in the region $0 < |x| < L$ the Kadomtsev function is a constant, $K(x) = K_{\min} < 0$, and the velocity profile is smooth, $V(x) = V'(0)x = V'x$. Under these assumptions the eigenvalue equation reduces to

$$U'' - \left[k^2 - \frac{\omega_S^2 K_{\min}}{(V'x - V_P)^2} \right] U = 0 \tag{3.9}$$

The general solution is easily found in terms of modified Bessel functions and is given by $U(z) = z^{1/2}\left[\hat{C}_1 K_\nu(z) + \hat{C}_2 I_\nu(z) \right]$ or in terms of ψ

$$\psi(z) = z^{-1/2}\left[C_1 K_\nu(z) + C_2 I_\nu(z) \right] \tag{3.10}$$

Here $z = kx - \omega / V'$ is a complex coordinate and the order ν is a function of $K_{\min}$:

$$\nu = \sqrt{\frac{1}{4} - \frac{\omega_S^2 K_{\min}}{V'^2}} \tag{3.11}$$

The boundary conditions lead to a simple dispersion relation:

$$\det \begin{vmatrix} I_\nu(z_+) & K_\nu(z_+) \\ I_\nu(z_-) & K_\nu(z_-) \end{vmatrix} = 0 \tag{3.12}$$

where $z_\pm = \pm kL - \omega / V'$

The eigenvalue ω as a function of wave number k is illustrated in Fig. 3 for a typical unstable case, $\nu = 3/2$. For this value the Bessel functions reduce to simple exponentials and algebraic terms from which the dispersion relation reduces to

$$\frac{\omega}{\omega_S} = i\left[\kappa \coth(2\kappa) - \frac{\kappa^2 + 1}{2} \right]^{1/2} \left(-K_{\min} \right)^{1/2} \tag{3.13}$$

where $\kappa = kL$. Also shown the growth rate curve for the static case $V' = 0$ whose growth rate is given by

$$\frac{\omega}{\omega_S} = i \frac{\kappa}{\left(\kappa^2 + \pi^2 / 4 \right)^{1/2}} \left(-K_{\min} \right)^{1/2} \tag{3.14}$$

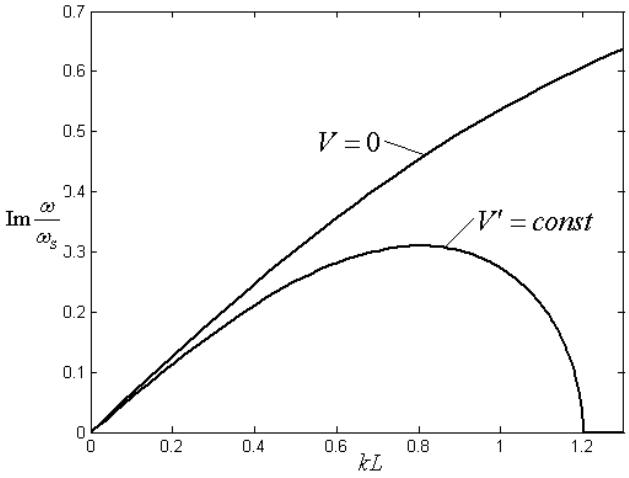

Figure 3-3 Eigenfrequency ω/ω_S vs. wavenumber kL for static case and constant velocity shear model with $\nu = 3/2$

Observe that the growth rate of the mode with a sheared flow increases with *k* starting at the origin, reaches a maximum, and finally decreases to zero at the maximum stable wave number $k = k_{\max}$. As ν decreases towards the value unity (corresponding to $K_{\min}$ increasing from the negative direction) the region of unstable wave numbers shrinks to zero; that is $k_{\max} \to 0$ as $\nu \to 1$.

The marginal stability boundary can be found analytically [see Appendix A] by focusing attention on the behavior of the dispersion relation for small kL. Specifically, we write $\omega = \omega_r + i\omega_i$, expand $\nu = 1 + \delta\nu$, and assume the following ordering scheme: $\omega_i / V' \ll kL \ll \delta\nu \ll 1$. Also, $\omega_r = 0$ by symmetry. Under these assumptions the small argument expansion of the Bessel functions can be used and the dispersion relation reduces to

$$\omega = \frac{i\pi}{2}\left(-\frac{K_{\min}}{K''_{\min}}\right)^{1/2} kV'(\nu - 1) \tag{3.15}$$

Note that for $\nu > 1$, there always exists an exponentially growing solution to the eigenmode equation. After a transformation of variables, it can be shown that this result overlaps with the early result of Kuo [15] who was interested in the geophysical problem of Rayleigh-Taylor instabilities in stratified fluids.

The conclusion is that a constant shear flow has a stabilizing effect on the interchange mode. The intuition is that flow shear inhibits the ability of the plasma to form very short wavelength instabilities, which are the most unstable modes for the case without flow. Specifically, the marginal stability boundary $K_{\min} \geq 0$ for the case of zero flow relaxes to $K_{\min} \geq -(3/4)V'^2/\omega_S^2$ for a constant shear flow. In terms of the physical variables the modified stability criterion can be written as

$$\frac{rp'}{\gamma p} + \frac{2B_\theta^2}{B_\theta^2 + \gamma\mu_0 p} > -\frac{3}{4}\frac{V'^2}{\omega_S^2} \tag{3.16}$$

When the flow velocities become comparable to the sound speed then the stability modifications become substantial.

3.4.2 The case of a velocity profile with no-slip boundary conditions

The situation modeled here corresponds to a plasma confined between rigid boundary surfaces with no-slip boundary conditions at each surface. Sketches of the actual cylindrical problem and the slab approximation are illustrated in Fig.3-4. Note that we again assume that $K_{\min} < 0$. The axial velocity profile is similar to that of a liquid flowing between two pipes of different radii.

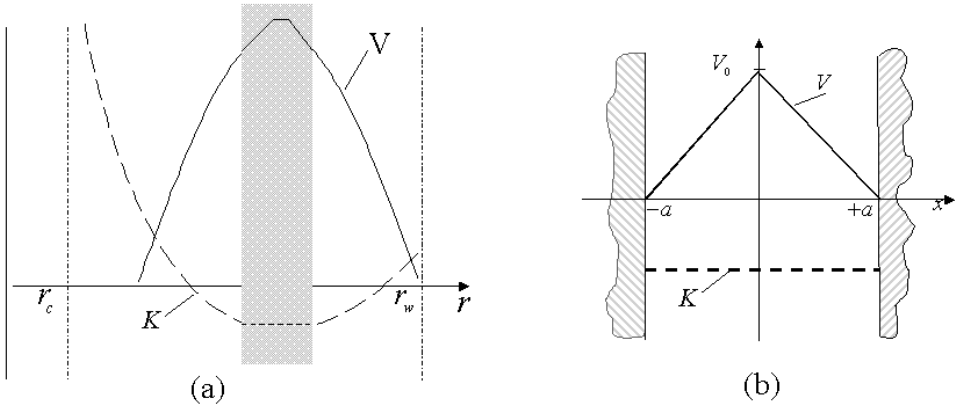

Figure 3-4 (a) Cylindrical model showing a no-slip velocity profile in a region where K<0 (b) it's slab approximation

The solution to the eigenvalue problem can be simplified by noting that the velocity has even symmetry: $V(x)=V(-x)$. This implies that the eigenfunctions are either purely even or purely odd. The most unstable case corresponds to an eigenfunction with no radial nodes. Therefore, the appropriate boundary conditions on ψ can be written as $\psi'(0)=0$ and $\psi(a)=0$. Since the shear in the region $0\le x\le a$ is constant the solution can again be written as a sum of Bessel functions: $\psi(z)=z^{-1/2}\left[C_1K_\nu(z)+C_2I_\nu(z)\right]$. Here, $z=k(a-x)-\omega/V'$ with $V'>0$ and ν is again given by Eq.(3.11). Applying the boundary conditions leads to the following dispersion relation

$$\det\begin{vmatrix}\left[I_\nu(z_0)/z_0^{1/2}\right]' & \left[K_\nu(z_0)/z_0^{1/2}\right]' \\ I_\nu(z_a) & K_\nu(z_a)\end{vmatrix}=0 \qquad (3.17)$$

where $z_0=z(0)=ka-\omega/V'$ and $z_a=z(a)=-\omega/V'$.

The qualitative properties of the instability can be obtained by examining the dispersion relation for the unstable case $\nu=3/2$. For this case the dispersion relation reduces to a third order polynomial in the variable $\Omega=\omega/V'-ka$ given by

$$\Omega^3+(\kappa+\tanh\kappa)\Omega^2+2\kappa\Omega+2(\kappa-\tanh\kappa)=0 \qquad (3.18)$$

where $\kappa = ka$. The real and imaginary parts of the Doppler shifted frequency are plotted in Fig. 3-5. Note that in this case the mode is unstable even as $ka \to \infty$. In fact the $ka \to \infty$ limiting value of the unstable eigenfrequency is easily found and can be written as

$$\frac{\omega}{V'} - ka = 1 + i \tag{3.19}$$

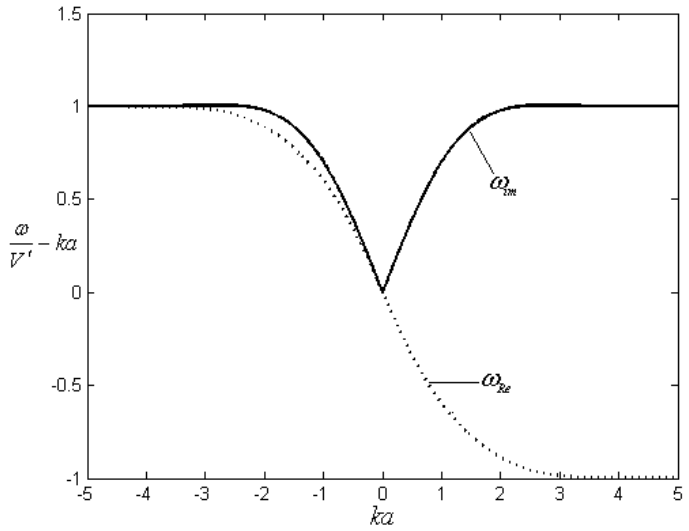

Figure 3-5 Eigenfrequency ω / ω_S vs. wavenumber ka for the no-slip velocity profile and $\nu = 3/2$

Further numerical studies show that instability persists until ν decreases to its marginal value $\nu = 1/2$. The marginal stability boundary can also be found analytically by focusing on the region of small ka. Applying the ordering scheme $\omega_i / V' \ll ka \ll \delta\nu \ll 1$ and using the small argument expansion of the Bessel functions leads to

$$\frac{\omega}{V'} = ka\,\delta\nu\left[1 + i\frac{\pi}{2}\left(\delta\nu + \left|\delta\nu\right|\right)\right] \tag{3.20}$$

where $\nu = 1/2 + \delta\nu$. For $\nu > 1/2$ there is always an unstable solution. The marginal stability limit $\nu = 1/2$ corresponds to the value $K_{\min} = 0$. In other words a no-slip

velocity flow does not affect the stability boundary, which reduces to the original Kadomtsev stability limit

$$\frac{rp'}{\gamma p}+\frac{2B_\theta^2}{B_\theta^2+\gamma\mu_0 p}>0 \tag{3.21}$$

The physical explanation for this behavior is as follows. In the limit of zero flow the unstable eigenfunctions tend to be localized in the region where $K=K_{\min}<0$. With a no-slip velocity flow of the type considered here there is by definition always a region where $V'=0$. If $K_{\min}<0$ in this region then localized modes will not feel the stabilizing effects of velocity shear and the stability boundary reduces to the no-flow limit.

3.4.3 The case of a counter-streaming velocity profile

The last model of interest involves a flow pattern consisting of two regions of plasma counter-streaming with respect to one another. The regions are connected by a thin of layer of plasma with a constant shear profile. The profiles for the cylindrical geometry and slab approximation are illustrated in Fig. 3-6. Because the flow pattern has an "S-like" shape the second derivative changes sign somewhere in the plasma suggesting that the Kelvin-Helmholtz instability may be excited.

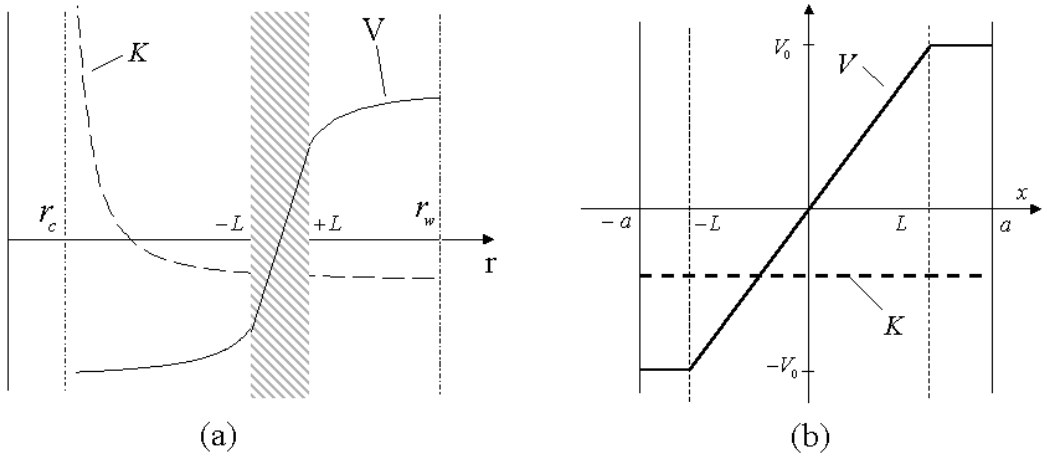

(a) (b)

Figure 3-6 (a) Cylindrical model showing a counter-streaming velocity profile in a region where $K<0$ (b) it's slab approximation

The analysis of this configuration is similar to case (A). The main difference is that the boundary conditions at $x=\pm L$ must be modified as follows. In the constant velocity regions $L\le|x|\le a$ the solution to the eigenvalue equation reduces to simple exponential functions: exp($\pm\alpha kx$) where $\alpha^2=1-\omega_S^2K_{\min}/\left(\omega-kV'L\right)^2$. The perturbed displacement is again required to vanish at $x=\pm a$. The solutions in these regions reduce to $\psi\left(\pm x\right)=C_\pm\sinh\left[\alpha k\left(x\mp a\right)\right]$, leading to boundary conditions at $x=\pm L$ given by $\psi'\left(\pm L\right)\pm\alpha k\coth\left[\alpha k\left(a-L\right)\right]\psi\left(\pm L\right)=0$ where 'prime' denotes x differentiation.

In the region of sheared flow the solutions again reduce to Bessel functions: $\psi(z)=z^{-1/2}\left[C_1K_\nu(z)+C_2I_\nu(z)\right]$, where as before $z=kx-\omega/V'$. For the interesting regime corresponding to a thin shear layer we assume that $kL\sim1$ and $L\ll a$. Applying the boundary conditions then leads to the following dispersion relation.

$$\det\begin{vmatrix}\left[z_+^{-1/2}e^{\alpha z_+}I_\nu(z_+)\right]' & \left[z_+^{-1/2}e^{\alpha z_+}K_\nu(z_+)\right]'\\ \left[z_-^{-1/2}e^{-\alpha z_-}I_\nu(z_-)\right]' & \left[z_-^{-1/2}e^{-\alpha z_-}K_\nu(z_-)\right]'\end{vmatrix}=0 \qquad (3.22)$$

where $z_\pm=\pm kL-\omega/V'$ and 'prime' now denotes z differentiation.

The dispersion relation for a typical unstable case corresponding to $\nu=1/2$ is illustrated in Fig. 3-7.

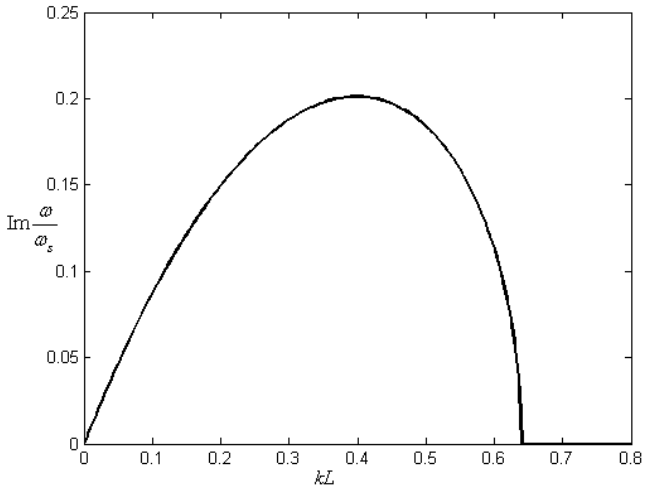

Figure 3-7 Eigenfrequency ω/ω_S vs. wavenumber kL for the counter-streaming velocity profile and $\nu = 1/2$

Note that this value of ν is equivalent to $K_{\min} = 0$ so that the instability is a pure fluid dynamics mode, not dependent on plasma physics. Observe that the mode is unstable for a finite range of wave numbers $k_{\min} < k < k_{\max}$. The values of $k_{\min}$ and $k_{\max}$ are easily found by solving the dispersion relation which reduces to the following simple analytic form

$$\frac{\omega}{V'} = i\left[\left(\kappa - \frac{1}{2}\right)^2 - \frac{1}{4}\exp(-4\kappa)\right]^{1/2} \tag{3.23}$$

with $\kappa = kL$. We find that the critical wave numbers are given by $k_{\min} = 0$ and $k_{\max} \approx 0.64$. Also, by symmetry, $\mathrm{Re}(\omega) = 0$.

As the value of ν decreases the system remains unstable, although the two critical values of k start to coalesce. Eventually, when ν decreases below a critical value, $k_{\min}$ and $k_{\max}$ overlap. This corresponds to the marginal stability point of the system. Numerically, marginal stability occurs when $\nu = 0$ at the fully coalesced value of wave number $kL \approx 0.60$. This result can be verified analytically by setting $\omega = 0$ and $\nu = 0$ in

the dispersion relation. The result, after a short calculation, is a transcendental equation for the marginal κ that can be written as

$$\frac{\kappa I_0'(\kappa)}{I_0(\kappa)} = \frac{1}{2} - \left(\kappa^2 - \frac{1}{4}\right)^{1/2} \tag{3.24}$$

It has a single real solution for κ given by $\kappa \approx 0.60$ thereby confirming the numerical results.

Observe that the marginal stability condition $\nu = 0$ corresponds to $K_{\min} = V'^2 / 4\omega_S^2$. As compared to the case of no flow, the value of $K_{\min}$ has increased from zero to a positive value; that is the system is more unstable. In terms of the physical variables the stability condition has the form

$$\frac{rp'}{\gamma p} + \frac{2B_\theta^2}{B_\theta^2 + \gamma\mu_0 p} > \frac{1}{4}\frac{V'^2}{\omega_S^2} \tag{3.25}$$

The physical explanation for the increased instability is associated with the "S-like" shape of the velocity profile. As is well known from fluid dynamics this can drive the Kelvin-Helmholtz instability. To prevent the mode from being excited the Kadomtsev function, which characterizes the plasma properties, must be even more stabilizing than without flow. Thus, from the point of view of the plasma the velocity shear has led to a decrease in stability.

3.5 Cylindrical results

The goal of this section is to determine the effect of flow shear on the MHD marginal stability boundaries using the full cylindrical model with realistic LDX-like profiles. Achieving this goal requires a combination of cylindrical numerical studies and physical intuition based on the simple slab results of the previous section.

The starting point of the analysis is the specification of LDX-like equilibrium profiles. The pressure and density are chosen in accordance with expected experimental profiles as follows

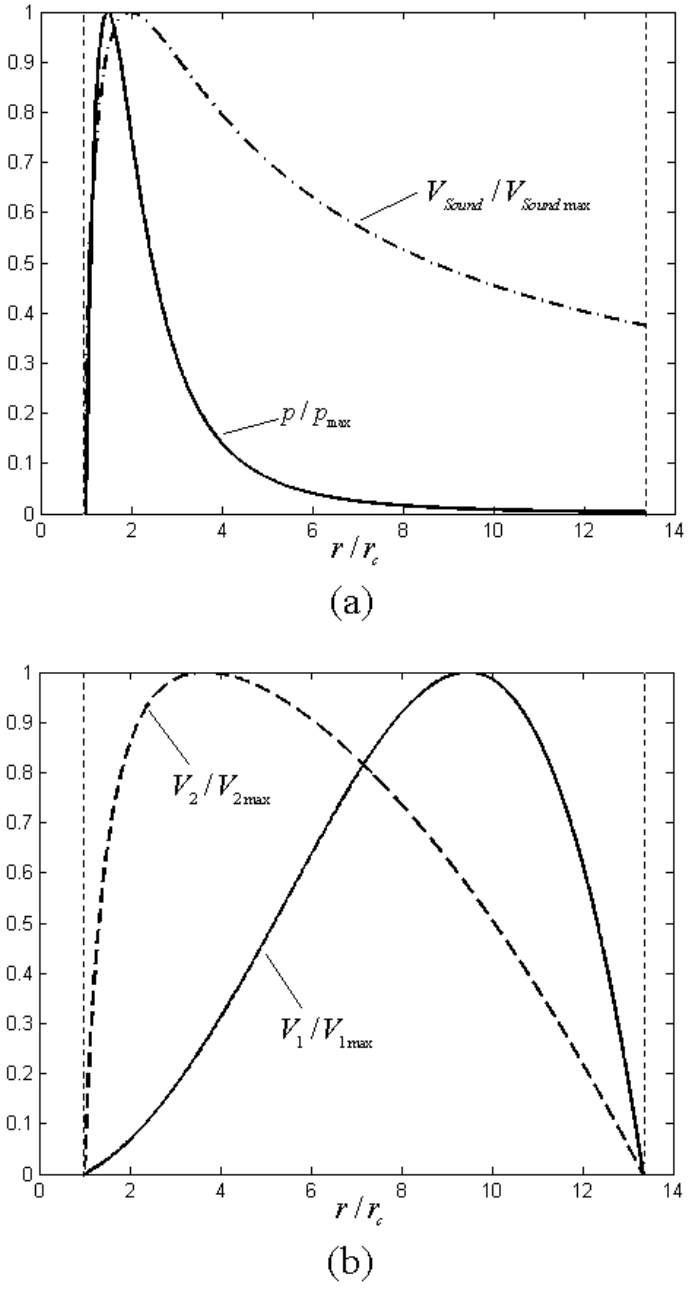

Figure 3-8 Cylindrical LDX profiles for (a) pressure and sound speed (b) analyzed velocity profiles

$$p(r) = p_w \left[\frac{(w+1)^\alpha}{w-1} \right] \left[\frac{x-1}{(x+1)^\alpha} \right]$$
$$\rho(r) = \rho_{\max} \left(\frac{2}{1+x} \right) \tag{3.26}$$

and are illustrated in Fig. 3-8a. Here $x = r^2 / r_c^2$, $w = r_w^2 / r_c^2$, and the plasma exists in the region $1 \le x \le w$. For LDX $r_w = 2m$ and the minor radius of the coil $r_c = 0.15m$, implying that $w \approx 178$. The quantity p_w is the edge pressure, which is assumed to be held fixed by the wall properties during all simulations. The quantity α is a profile parameter that determines how gradually the pressure profile decays to zero far from the coil. For a fixed edge pressure, high α implies a high peak pressure and a corresponding high value of β. The density decays as $\rho \propto 1/r^2$ at large distances and has the value $\rho = \rho_{\max}$ at the surface of the coil. The $1/r^2$ decay accounts for the fact that flux tubes can be randomly exchanged when the interchange mode is excited, usually near the outer portion of the plasma. Therefore, each flux tube must have the same number of particles implying that $\rho \propto 1/r^2$. In fact, Pastukhov and Chudin [22, 23] show that this scaling persists even during the nonlinear phase of the evolution of the interchange instability.

Next, note that the peak pressure occurs at $x_{\max} = (\alpha+1)/(\alpha-1)$ and is related to the edge pressure by

$$\frac{p_{\max}}{p_w} = \left[\frac{(\alpha-1)}{2\alpha} \right]^{\alpha-1} \left[\frac{(w+1)^\alpha}{\alpha(w-1)} \right] \tag{3.27}$$

To keep the number of free parameters manageable we assume that the plasmas of interest have low $p_{\max}$ and hence, low β. This is consistent with the experimental conditions on LDX and yields results that are very insensitive to the value of p_w except

as it appears in simple scaling relations. The low β assumption enters the analysis by allowing us to accurately approximate the magnetic field by its vacuum value. Thus, the B_θ profile is given by

$$B_\theta(r) = \left(\frac{\mu_0 I_c}{2\pi r_c}\right)\frac{1}{x^{1/2}} \tag{3.28}$$

where I_c is the coil current.

The last profile of interest is that of the equilibrium flow velocity. In the analysis that follows two cases are considered:

$$\begin{aligned} V_1(r) &= \frac{4V_{\max}}{(w-1)^2}(x-1)(w-x) \\ V_2(r) &= \frac{V_{\max}}{\left(w^{1/2}-1\right)^2}\frac{(x-1)(w-x)}{x} \end{aligned} \tag{3.29}$$

Both profiles satisfy the no slip condition as illustrated in Fig. 8b. The first profile reaches a maximum at $x_{\max} = (w+1)/2$, well beyond the pressure peak. Qualitatively, this profile might be generated by the $\mathbf{E}\times\mathbf{B}/B^2$ drift, which peaks far out because of the rapidly decreasing value of B. The second profile peaks at $x_{\max} = w^{1/2}$ which is much closer to the pressure maximum. Such a profile might be generated in a beam driven system. We emphasize that at present there is no detailed experimental data to motivate the choice of velocity profile and the two cases discussed should just be viewed as plausible possibilities.

The profiles have now been specified. The next step is to solve the cylindrical differential equation to determine the marginal stability boundary. In particular, in the low β limit we wish to determine the marginally stable value of the profile parameter α as a function of the maximum velocity $V_{\max}$. The strictest marginal α is determined by

numerically searching for the marginal α at fixed k and $V_{\max}$, and then repeating the procedure by varying k until the lowest marginal α is found; that is, the strictest marginal α is defined as $\alpha(V_{\max}) = \min_k \left[\alpha_{mar}(k, V_{\max}) \right]$. Knowing $\alpha(V_{\max})$ it is then straightforward to calculate the increase or decrease in critical β as a function of flow velocity. The critical figure of merit is defined as

$$\eta \equiv \frac{\beta_{\max}(V_{\max})}{\beta_{\max}(V_{\max}=0)} \tag{3.30}$$

where

$$\begin{aligned} \beta &= \frac{2\mu_0}{B_\theta^2(r_w)} \left(\frac{2}{r_w^2 - r_c^2} \int_{r_c}^{r_w} pr dr \right) \\ &= \frac{8\pi^2 r_c^2}{\mu_0 I_c^2} \left(\frac{r_w^2}{r_w^2 - r_c^2} \right) \int_1^w p\, dx \\ &\approx \frac{8\pi^2 r_c^2}{\mu_0 I_c^2} \int_1^\infty p\, dx \end{aligned} \tag{3.31}$$

and $\beta_{\max}$ is the largest value of β that is stable (the value corresponding to the marginal α). The last approximate expression corresponds to the interesting limit $w \gg 1$. For our profiles it follows that

$$\begin{aligned} \eta &= \left[\frac{(\alpha_0 - 1)(\alpha_0 - 2)}{(\alpha - 1)(\alpha - 2)} \right] \left\{ \frac{1 - \left[(\alpha - 1)w - (\alpha - 3) \right] / \left[2^{2-\alpha} (w+1)^{\alpha - 1} \right]}{1 - \left[(\alpha_0 - 1)w - (\alpha_0 - 3) \right] / \left[2^{2-\alpha_0} (w+1)^{\alpha_0 - 1} \right]} \right\} \left(\frac{w+1}{2} \right)^{\alpha - \alpha_0} \\ &\approx \left[\frac{(\alpha_0 - 1)(\alpha_0 - 2)}{(\alpha - 1)(\alpha - 2)} \right] \left(\frac{w}{2} \right)^{\alpha - \alpha_0} \end{aligned} \tag{3.32}$$

Here, $\alpha_0 = \alpha(V_{\max} = 0)$ is the marginal value for zero flow and $\alpha = \alpha(V_{\max})$ is the marginal value for finite flow. Observe that for $w \gg 1$ even a small increase in the marginal α due to flow can substantially increase the critical β since $\eta \propto w^{\alpha - \alpha_0}$.

The final preparatory step is to calculate the explicit conditions for marginal stability for the no-flow case $V_{\max} = 0$. This will serve as the reference case when analyzing marginal stability for the two different velocity profiles. For $V_{\max} = 0$, marginal stability in the cylindrical case occurs when $k \to \infty$ and requires that the Kadomtsev function be positive for all r. In other words marginal stability occurs when $\min_r \left[K\left(r, \alpha_0\right) \right] = 0$. For the profiles under consideration this condition reduces to

$$\min_x \left\{ \frac{x\left[\left(\alpha_0 + 1\right) - \left(\alpha_0 - 1\right) x \right]}{\gamma\left(x^2 - 1\right)} + 1 \right\} = 0 \tag{3.33}$$

The function in the brackets is plotted as a function of x in Fig. 3-9 and is labeled "K_0".

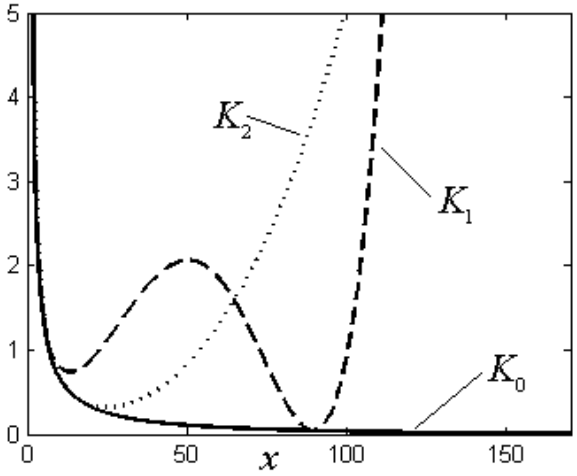

Figure 3-9 Kadomtsev function K_0 and modified stability criteria K_1 and K_2 for two velocity profiles

Observe that the function is a monotonically decreasing function of x implying that the most unstable point is $x = w$. The marginal value of α for the reference case is thus given by

$$\alpha_0 = \left(\frac{w+1}{w} \right) \gamma + \left(\frac{w+1}{w-1} \right) \approx \gamma + 1 \tag{3.34}$$

For $\gamma = 5/3$ and $w = (2/0.15)^2$ we find that $\alpha_0 = 2.687$.

We now turn to the cylindrical stability results for the two velocity profiles of interest.

3.5.1 The first model velocity profile

Some insight into the effect of the first velocity profile (the one that peaks far out) can be obtained by noting the following points. First, since $V'' < 0$ everywhere, there is no "S-like" behavior and the Kelvin-Helmholtz instability, as described by slab model (C), should not be excited. Second, over the major part of the profile the velocity shear is non-zero and in these regions, slab model (A) should apply, implying increased stability. Third, near the peak of the velocity, $V' = 0$ by definition, and in this region slab model (B) should apply in which case there should be very little change in stability. Fourth, the marginal stability criteria for slab models (A) and (B) just happen to coincide when $V' = 0$. The fifth and critical point is that when the velocity peaks far out (at $x_{\max} \approx w/2$), the ratio of xp'/p is very nearly a constant over the entire region $x_{\max} < x < w$. Therefore, since xp'/p does not change, the marginal α obtained by setting $K(\alpha, x_{\max}) = 0$ is almost identical to the static value derived from $K_0(\alpha_0, w) = 0$.

The overall stability picture can be understood by examining the curve of $K_1(\alpha, S, x)$ vs. x also illustrated in Fig. 3-9. This curve corresponds to the local velocity shear stabilized Kadomtsev criterion given by Eq. (3.16), plotted for the case $\alpha = \alpha_0$ and $S = 1$. Here, S is an equivalent Mach number defined as a ratio of the maximum flow speed to the maximum sound speed of the static marginally stable plasma. The sound speed of the static plasma reaches it's maximum at $x = \alpha_0/(\alpha_0 - 2)$ and has the value

$$V_{S\max} = \sqrt{\left(\gamma p_{static}/\rho\right)_{\max}} = \left[\frac{\gamma p_w}{\rho_{\max}} \frac{\left(\alpha_0 - 2\right)^{\alpha_0 - 2}}{2^{\alpha_0 - 1}\left(\alpha_0 - 1\right)^{\alpha_0 - 1}} \frac{\left(w+1\right)^{\alpha_0}}{w-1}\right]^{1/2} \tag{3.35}$$

Thus, the parameter S is defined by

$$S = \left[\frac{V_{\max}^2}{V_{S\max}^2}\right]^{1/2} = \left[\frac{\rho_{\max} V_{\max}^2}{\gamma p_w}\right]^{1/2} \cdot \left[\frac{2^{\alpha_0 - 1}\left(\alpha_0 - 1\right)^{\alpha_0 - 1}}{\left(\alpha_0 - 2\right)^{\alpha_0 - 2}} \frac{w-1}{\left(w+1\right)^{\alpha_0}}\right]^{1/2} \tag{3.36}$$

Observe, that as expected $K_1 \geq K_0$, the equality occurring at the point $x_{\max} \approx w/2$ where $V' = 0$. Also, K_1 has a minimum very near $x = x_{\max}$. Technically, $K_1\left(\alpha_0, S, x_{\max}\right)$ is greater than $K_0\left(\alpha_0, w\right) = 0$ implying that with flow, α can be raised above the value α_0 until marginal stability is reached: $K_1\left(\alpha, S, x_{\max)}\right) = K_0\left(\alpha_0, w\right) = 0$. However, because of the flatness of K_0, the gap $K_0\left(\alpha_0, w\right) - K_0\left(\alpha_0, x_{\max}\right)$ is so small that the increase in α is virtually negligible.

The exact marginally stable α as a function of the velocity shear S, as predicted by the local slab model (A), is easily obtained by finding the value of $x = x_A$ that minimizes $K_1\left(\alpha, S, x\right)$:

$$\begin{aligned} &\min_x \left\{\frac{x\left[\left(\alpha+1\right) - \left(\alpha-1\right)x\right]}{\gamma\left(x^2-1\right)} + 1 + g_1 S^2 \left[\frac{x^2\left(x+1\right)^{\alpha-1}\left(w+1-2x\right)^2}{\left(w-1\right)^4\left(x-1\right)}\right]\right\} = 0 \\ &g_1\left(w\right) = \frac{12\left(\alpha_0 - 2\right)^{\alpha_0 - 2}}{2^{\alpha_0 - 1}\left(\alpha_0 - 1\right)^{\alpha_0 - 1}} \approx 1.192 \end{aligned} \tag{3.37}$$

and then setting $K_1\left(\alpha, S, x_A\right) = 0$ to obtain $\alpha = \alpha\left(S\right)$. This curve is plotted in Fig. 3-10.

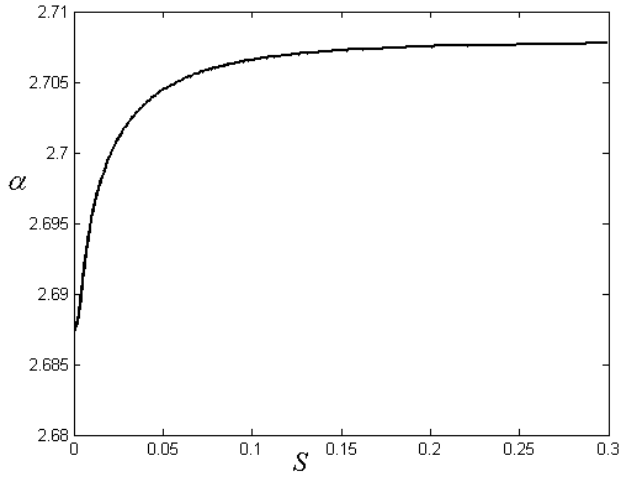

Figure 3-10 Marginal α for the first velocity profile

Note, that α increases with S as expected. Most of the increase occurs for small S as the minimum point of K_1 moves from the plasma edge, when $S = 0$, to its saturated value when the minimum coincides with the peak of the velocity. In any event the total increase is very small, raising α from 2.687 to 2.708. This produces a very modest gain in β given by $\eta = 1.05$.

The net result of this intuition is that the marginally stable values of α as predicted by slab models (A) and (B) are essentially identical and equal to the no-flow value α_0. The final conclusion is that the gain factor $\eta \approx 1$ (i.e. there is virtually no gain in β due to a sheared velocity flow that peaks far beyond the pressure maximum).

This intuition has been tested by numerically solving the full cylindrical eigenvalue equation for the profiles of interest using the LDX parameters and following the procedure described earlier. The details of numerical algorithm are given in Appendix B. The results are similar to those just described. The peak of the eigenfunction moves from the plasma edge to the point where $V' = 0$ as S increases. The eigenfunction for large k

is highly localized in space. The marginal α is very close to α_0. Numerical inaccuracies associated with the use of finite rather than infinite k plus the high localization of the mode make it difficult to precisely calculate the very small differences in the marginal α as S varies. However, since the differences are very small it is not of great interest to pursue the numerical studies for the first velocity profile in any further detail.

3.5.2 Second velocity profile

Consider now the second velocity profile, which peaks much closer to the pressure maximum, at $x = x_{\max} = w^{1/2}$. This profile has a constant velocity shear over almost the entire region of unfavorable magnetic curvature and, consequently, we might expect to see an improvement in stability. This is indeed the case as can be intuitively understood by comparing the similarities and differences with respect to the first profile. The similarities are as follows. Again $V'' < 0$ everywhere so no Kelvin-Helmholtz instability is expected. Because of the large constant shear region, stability should be most similar to slab model (A). There is a small region close to the plasma where $V' = 0$ and in this region slab model (B) should apply. The stability criteria given by slab models (A) and (B) coincide in the region where $V' = 0$.

The critical difference is that the region where the criteria overlap is much closer to the peak pressure for the second velocity profile. In this region the ratio rp'/p is substantially different from its asymptotic value as $r \to \infty$. The implication is that at the overlap point the local stability criterion is satisfied by a substantial margin. Hence, we expect that it should be possible to raise α by a finite amount before reaching the marginal stability point.

This idea can be understood by examining the local stability curve corresponding to case (A) as a function of position. The curve is labeled $K_2 = K_2\left[\alpha, S, x\right]$ and is also illustrated in Fig.9 for the parameters $\alpha = \alpha_0, S = 1$. Observe that K_2 coincides with K_0 at the point where $V_2' = 0$ and has a minimum at $x = x_B$ slightly further out. It is clear from the curve that at this point $K_{2\min} = K_2\left(\alpha_0, S, x_B\right) > K_0\left(\alpha_0, w\right)$. Since raising α lowers curve K_2 when α is raised by a sufficient amount, then $K_2\left(\alpha, S, x_B\right) = K_0\left(\alpha_0, w\right) = 0$ and marginal stability has been achieved. The quantitative prediction of the marginal stability boundary $\alpha = \alpha\left(S\right)$ resulting from slab model (A) is easily obtained by solving

$$\min_x \left\{ \frac{x\left[\left(\alpha+1\right)-\left(\alpha-1\right)x\right]}{\gamma\left(x^2-1\right)} + 1 + g_2 S^2 \left[\frac{\left(x+1\right)^{\alpha-1}\left(w-x^2\right)^2}{\left(w^{1/2}-1\right)^4 x^2 \left(x-1\right)} \right] \right\} = 0$$
$$g_2\left(w\right) = \frac{3}{4}\frac{\left(\alpha_0-2\right)^{\alpha_0-2}}{2^{\alpha_0-1}\left(\alpha_0-1\right)^{\alpha_0-1}} \approx 7.45\cdot 10^{-2} \tag{3.38}$$

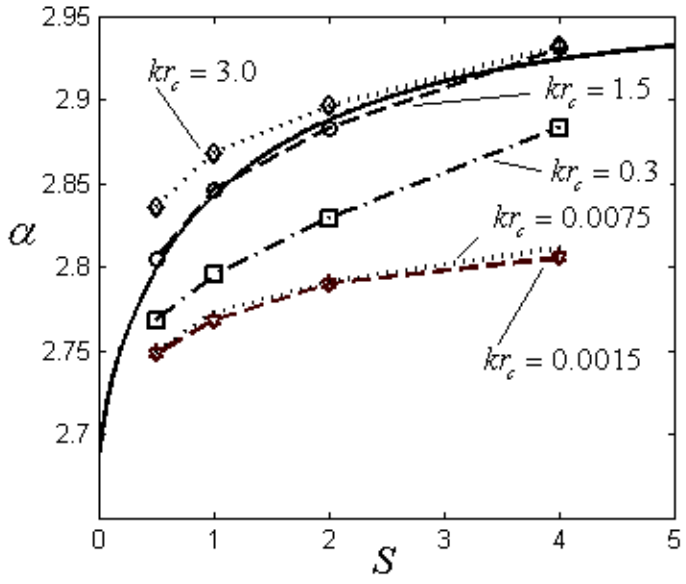

Figure 3-11 Marginal α for the second velocity profile. The theoretical slab result corresponds to the solid curve. The cylindrical simulations results have the data points explicitly shown

The curve of $\alpha = \alpha(S)$ is illustrated as the solid curve in Fig. 3-11. We see that α increases with S and in the limit $S \to \infty$ saturates at the value 2.954 (for the given value of w). As a specific example, for $S = 1$ the marginal α has increased to 2.83, a substantial increase over the no flow limit. For this value of α the gain in β is finite: $\eta = 1.56$. The entire curve of η vs. S is shown as the solid curve in Fig. 3-12.

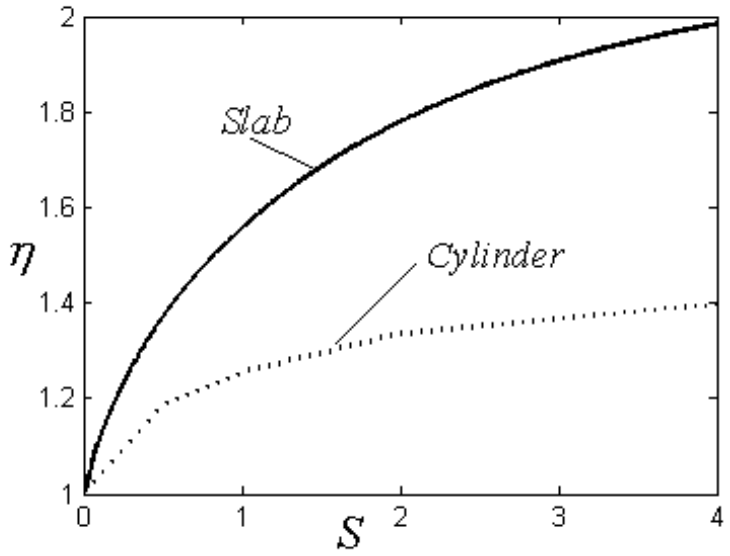

Figure 3-12 The β ratio η vs. parameter S for slab predictions and actual cylindrical results

The overall insight from the slab analysis is that for velocity profiles peaked near the pressure maximum, the stabilizing effects of shear are substantial leading to finite increases in the marginally stable β.

This intuition has been tested by solving the cylindrical eigenvalue equation for the second velocity profile. The details of numerical algorithm are given in Appendix B. Overall, the results are qualitatively similar although, as discussed shortly, there is one important effect that produces finite quantitative changes in the marginal stability boundary.

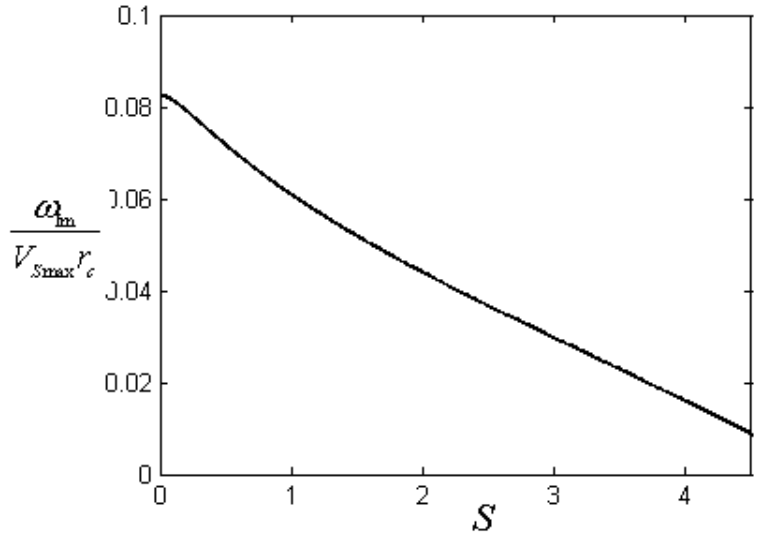

Figure 3-13 Normalized growth rate vs. flow parameter S for $kr_c = 1.5$ and $\alpha = 2.95$

The first indication that shear provides a stabilizing effect is shown in Fig. 3-13 where we plot normalized growth rate $\omega_i / \left(V_{S\max} r_c \right)$ vs. S for the unstable case $kr_c = 1.5, \alpha = 2.95$ and $V_{S\max}$ given by Eq. (3.35). As has been found by several other authors [12, 13, 14], we see that the growth rate decreases as the velocity shear increases.

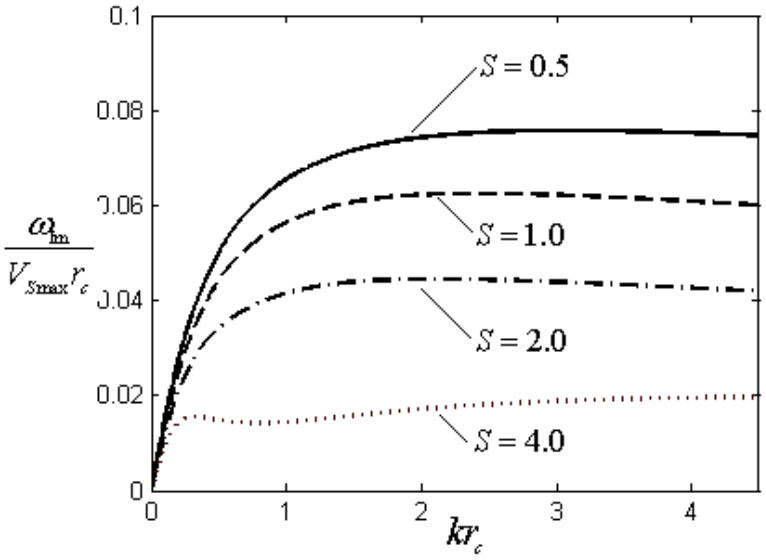

Figure 3-14 Normalized growth rate vs. wavenumber kr_c for several S and $\alpha = 2.95$

A second set of simulations illustrates normalized growth rate vs. wave number for various values of S at a fixed, unstable $\alpha = 2.95$ (See Fig. 3-14). Note that the growth rate decreases as the velocity shear increases. Interestingly, the fastest growth rates occur at very large kr_c. The growth rate initially increases with kr_c, then temporarily decreases and eventually starts to grow at large kr_c again. The explanation may lie in difference between the cylindrical and slab geometry. The interchange mode requires the highest possible wavenumber, while the plasma with velocity shear is most unstable for finite wavenumber. The competition between these two different effects is responsible for the behavior of the growthrate. This behavior has similarities with the growthrate observed by Guzdar *et. al* [16], where the competing effects were due to the KH and Rayleigh-Taylor modes.

The slab model also suggests that large kr_c should be completely stabilized by velocity shear above a critical value $(kr_c)_{crit}$ but this behavior is not observed in the cylindrical case. The reason is again associated with finite cylindrical effects that spread the eigenfunction over a larger portion of the profile when the plasma is unstable. The mode becomes localized only for large kr_c near marginal stability.

The difference in kr_c scaling relations between the slab and cylinder lead to quantitative changes in the marginal stability boundary for the following reason. Intuitively, we expect the slab model to be a reasonably accurate approximation to the cylinder when the modes are localized, which typically occurs for $kr_c \to \infty$. However, the slab model predicts that the most unstable wave numbers near marginal stability correspond to $kr_c \to 0$. This dichotomy can be seen by re-examining Fig. 3-11. Superimposed on the

slab stability predictions are the cylindrical marginal stability results for various kr_c. For large kr_c the cylindrical and slab results are quite similar; as stated, in this regime the slab model is a good approximation. However, as kr_c decreases the marginal stability boundary is lowered (i.e. becomes more restrictive), finally reaching a saturated value when $kr_c \to 0$. For a given value of S the gain in α due to shear is approximately halved as kr_c decreases from infinity to zero. The gain in β due to velocity shear is also plotted in Fig. 12 for the actual cylindrical marginal stability boundary corresponding to $kr_c \to 0$. We see that the cylindrical β gain is more modest as compared to the slab prediction.

3.6 Conclusions

The effect of velocity shear on the MHD interchange stability in a hardcore Z-pinch has been investigated in both slab and cylindrical geometries. The basic question is to determine whether velocity shear improves or worsens stability as compared to the static case. Our slab geometry results indicate that all options are possible, depending upon the precise shape of the velocity profile. A constant velocity shear improves stability. A peaked velocity profile has little effect on stability. A counter-streaming S-shaped velocity profile worsens stability.

The slab results have been used to interpret numerical simulations of a cylindrical hardcore Z-pinch (modeling LDX) with a velocity profile corresponding to no-slip boundary conditions; i.e. the velocity is zero at each boundary and peaks in the middle. When the velocity profile peaks far from the pressure maximum, then the constant shear and peaked velocity criteria overlap. The net result is that there is almost no change in the marginal stability boundary due to the flow. On the other hand, when the velocity

peaks near the pressure maximum, the constant shear slab model is the best approximation. There is a finite improvement in stability due to velocity shear, although quantitatively the cylindrical gains are more modest than the slab predictions.

It is important to notice that the change of the marginal stability limits due to sheared flow becomes noticeable only for the supersonic flows, peaking deeply in the plasma core. The most plausible source of the toroidal flow in the LDX is an $\mathbf{E}\times\mathbf{B}$ drift due to radial electric field. The electric field may be caused by non-ambipolar transport or unintentional electrostatic bias of the floating coil. This type of flow has the flow profile peaking far away from the pressure peak. Also, the likely toroidal flows in LDX will be subsonic making the change in the marginal stability limit negligible. Thus, for simplicity purposes, we will thereafter ignore the effect of the flows on the stability of LDX and a Z-pinch and will consider all plasmas to be static.

In the next chapter we will derive the quasilinear transport equations for the static plasmas in the axisymmetric closed-field line configurations.

Chapter 4

4 Quasilinear ideal MHD transport model for the axisymmetric closed field line magnetic configurations

4.1 Introduction

The goal of this chapter is to make a model of the plasma transport for the axisymmetric closed-line poloidal field line systems when a plasma is weakly unstable to an interchange mode. The primarily experimental application of the analysis is to the Levitated Dipole Experiment (LDX) [1-2]. LDX, a joint MIT and Columbia University experiment, has a plasma confined in a poloidal field created by superconducting current ring, which is magnetically floated in a large vacuum chamber.

There is a key difference between the LDX and tokamak approach to stabilize plasma. The tokamak approach requires a carefully chosen magnetic shear. The shear effectively prohibits all compressible modes and stabilizes incompressible MHD instabilities. LDX, on the other hand, has only a poloidal field, where stability is provided by plasma compressibility. As with any other magnetic configuration, LDX should be operated in a magneto-hydrodynamically (MHD) stable regime. The linear stability of a plasma in a point dipole and the real LDX configurations have been extensively studied by several authors [3-6]. The conventional approach is to consider an MHD stable plasma and to concentrate on weaker instabilities, such as electrostatic and kinetic modes.

At the same time, to achieve an optimal confinement performance, it is desirable to operate the machine close to the MHD marginal stability limit. The heating evolution, impurities or random fluctuations can push the system beyond the stability boundary. While there exists a good knowledge of the stability limits, understanding of the dynamics of the unstable system is sketchy at best. It is well known that the excitation of MHD unstable modes often leads to a violent restructuring of the plasma profiles and may cause a complete loss of plasma.

The typical approach to understanding the behavior of an unstable system includes detailed, often time consuming numerical simulations to track the evolution of the system on the Alfven time scale. An alternative approach, employed in this study, is to create an analytical model, which predicts the energy and particle transport of a plasma in the region weakly unstable to the interchange mode. To understand the advantages of the proposed approach, it is instructive to revisit the previous efforts to study the dynamics of the MHD unstable systems. The majority of this work has been done with numerical simulations.

An example of one of the few codes that solves the system of MHD equations and carries out simulations of the MHD unstable dynamics is a NIMROD [7]. The code is actively used by tokamak community and produce valuable insights into MHD dynamics of a simulated plasma. However, any detailed simulation of MHD instabilities with this code, as with any other, requires significant computational resources.

The simulation of a closed field line system is less likely to be that time-consuming, but have it’s own difficulties. D. Ryutov has showed that the numerical viscosity and diffusivity, necessary for proper numerical conversion, might lead to error accumulations, thus changing the self-consistent marginally stable plasma profiles [8]. Another concern

with any numerical simulation, which has sufficient viscosity and resistivity necessary to provide numerical convergence, is a dampening of the small-scale turbulences in favor of the global modes. The global modes are proven to be less susceptible to viscous energy losses and numerical resolution restrictions.

The simulation of a hard-core Z-pinch magnetic geometry, which could be considered an approximation to a high aspect ratio dipole, is a more doable problem. Both magnetic configurations represent closed filed line systems with the interchange mode imposing the most restrictive MHD stability condition. Pastukhov and Chudin modeled the system of reduced MHD equations for a weakly unstable Z-pinch plasma [9-10]. The key result was that violation of the marginal stability did not lead to a disruption, but resulted in non-local anomalous transport through the global plasma motion. A large-scale convective motion of the plasma enhanced the energy transport to balance heating source, thus keeping the system close to marginal stability. Anomalous transport due to macroscopic convective cells was also separately reported by Makhnin *et al.* [11] and Adler and Hassam [12]. Adler and Hassam forced the convective cells by the asymmetric energy and particle sources, while Makhnin reported short-lived random convective cells that were later replaced by a chaotic turbulence.

Summarizing, the numerical codes do provide valuable insights into the dynamics of an MHD unstable system, but often require significant computational resources and have internal numerical limitations, which may affect the results.

An alternative approach, employed in this study, is to create an analytical model, which predicts the energy and particle transport of a plasma in the region weakly unstable to the interchange mode. It is shown that an excitation of MHD instabilities creates new type of transport, seen in quasilinear approximation. We have employed this approximation to

derive transport equations in the MHD unstable region and have shown that the quasilinear transport relaxes the system back to marginal stability.

The quasilinear approach is routinely used in evaluating plasma response to RF-heating [13]. The perturbation forced by an incoming RF wave is evaluated up to a second order and averaged over time and space. The resulted equations describe the diffusion of absorbed RH heating in a plasma.

This chapter derives the quasilinear transport equations, where the perturbations are due to ideal MHD instability. Following this approach we will not calculate the exact saturated amplitudes of the modes or evaluate a quasilinear diffusion coefficient. However, in the most interesting limit of the MHD instability dominance, the method leads to exact equations of plasma evolution and self-consistent plasma profiles. Contrary to the non-linear numerical models, the quasilinear transport equations are derived with a specific assumption that the system relaxes before any perturbations could reach non-linear phase.

The chapter is organized as follows: Section 2 discusses the basics issues of a quasilinear approach. In chapter 3 the full quasilinear transport equations are derived for a Z-pinch magnetic geometry. Section 4 presents the derivation of a one dimensional steady state transport for a Z-pinch geometry. The full quasilinear transport equations are rewritten in a more transparent form. This form is then reduced for a specific assumption of quasilinear transport dominance. A sample model is used to illustrate the validity of the approximations.

In section 5, the quasilinear transport equations are generalized to a toroidal axisymmetric closed-field line magnetic configuration. Finally, section 6 presents non-linear numerical simulations of the evolution of an unstable plasma in a hard-core Z-

pinch magnetic configuration. We test the applicability of the ideal MHD quasilinear model derived earlier and discuss implications for predicting plasma profiles.

4.2 MHD quasilinear transport – basic issues

In this section we will discuss the basic issues arising in the formulation of MHD quasilinear transport arising from ideal MHD interchange modes in an axisymmetric, closed line, toroidal configuration. This configuration includes the levitated dipole configuration as well as its large aspect ratio limit, the hard core Z-pinch.

For the system under consideration the primary unknowns to be determined are the pressure p, density ρ, poloidal magnetic field $\mathbf{B}_p$, and the diffusion velocity $\mathbf{v}$. Following the standard procedures used in the quasilinear theory of kinetic instabilities [13] we expand all unknowns as

$$Q(\mathbf{r},t) = \bar{Q}(\psi,\varepsilon t) + \tilde{Q}(\psi,\chi,\phi,t) \tag{4.1}$$

Note that we have introduced flux coordinates where the "radial" coordinate ψ is tied to the background magnetic field, χ is an arbitrary poloidal angle, and ϕ is the standard toroidal angle. The various quantities $\bar{Q}(\psi,\varepsilon t)$ represent the background state of the plasma. These are one-dimensional functions, which are allowed to vary slowly with time due to the quasilinear plus classical evolution of the system. It is the evolution of the $\bar{Q}(\psi,\varepsilon t)$ with respect to the background flux that is the primary goal of the analysis.

The quantities $\tilde{Q}(\mathbf{r},t)$ represent the perturbations away from equilibrium due to MHD instabilities and are responsible for driving the quasilinear transport. Their amplitudes are assumed to be small enough (e.g. $\tilde{Q} \ll \bar{Q}$) so that nonlinear effects can be neglected,

but still large enough that the resulting quasilinear diffusion dominates classical transport. Mathematically, the perturbed quantities represent a sum over the unstable linear eigenmodes of the system with each mode calculated by neglecting the slow variation of the background state. In the analysis the perturbations are assumed to arise solely from interchange instabilities.

Collisional effects, such as resistivity and thermal conductivity also lead to transport of energy and particles as well as affecting the growth rates and eigenmodes of the MHD perturbations. These effects are considered in detail the Section V. Qualitatively, these effects are important in regions of the pressure profile where localized interchange modes are stable. In these regions collisional effects then represent the only source of transport. In the unstable regions, the ideal MHD modes typically have a much faster time scale than any collisional transport contributions. Therefore, we assume that collisional effects do not significantly alter the growth rates or change the eigenfunctions of the unstable perturbations.

An important conclusion from the analysis, applicable in the interesting regime where the quasilinear transport coefficients are much larger than those due to classical transport, is the following: The final steady state profiles can be uniquely determined and are independent of the specific details of the quasilinear transport coefficients. There is no need to explicitly calculate the saturated amplitudes of the unstable MHD modes.

With this as background we are now ready to begin the detailed analysis of quasilinear transport in the MHD model.

4.3 Quasilinear transport in a hard core Z-pinch

The first geometry of interest is the hard core Z-pinch, a cylindrically symmetric configuration for which the analysis is highly simplified. The analysis separates into two contributions, one from the MHD stable region that is assumed to obey the laws of classical transport, the other from the region that is unstable to MHD-interchange modes. A general 1-D transport equation is derived that is valid in both regions, followed by a simple calculation that shows how the two regions are connected across the marginal stability boundary.

4.3.1 The general 1-D transport equations

It is well known [14] that a hard-core Z-pinch is potentially unstable to only two ideal MHD modes: the $m = 0$ interchange mode and the $m = 1$ helical mode. Here, m is the azimuthal wave number. The interchange mode imposes the strictest limitations on the plasma profile and sets the value of the maximum achievable local pressure gradient. The fastest growing interchange modes are localized in space and occur for large longitudinal wave numbers (i.e. $k \to \infty$). For the LDX configuration the outer portion of the profile, beyond the location of the pressure peak, is the region likely to be unstable to interchange modes. See Fig. 4-1.

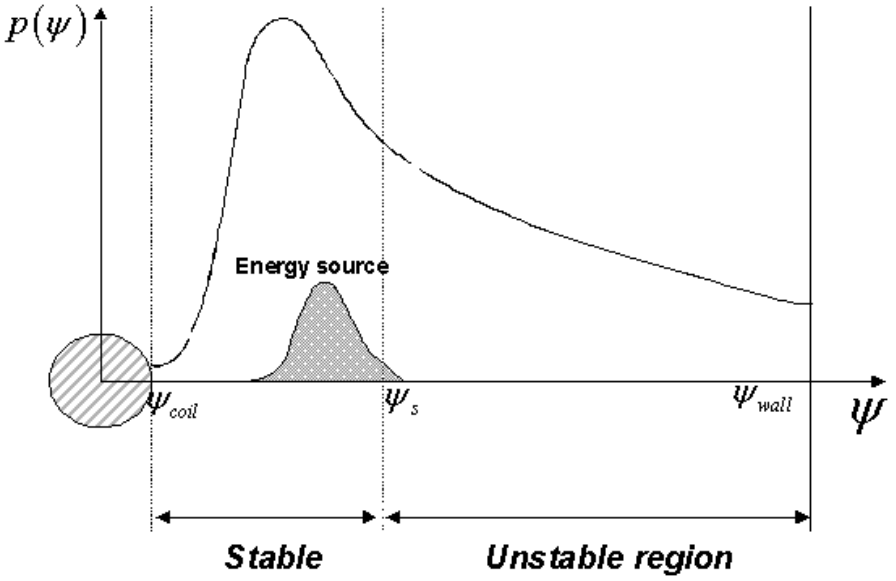

Figure 4-1 The LDX schematic pressure

The inner region, where the pressure gradient is positive, is stable to interchange modes. It is in this region that classical transport is assumed. Our goal here is to derive a set of 1-D transport equations valid in both regions.

The starting point for the analysis is a simplified, nonlinear single fluid model that includes thermal conductivity, resistivity, and the thermal force, but for simplicity neglects viscosity. The starting model is thus given by

$$\begin{aligned}
&\frac{\partial n}{\partial t} + \nabla \cdot (n\,\mathbf{v}) = 0 \\
&m_i n\left(\frac{\partial \mathbf{v}}{\partial t} + \mathbf{v}\cdot\nabla\mathbf{v}\right) = \mathbf{J}\times\mathbf{B} - \nabla p \\
&\frac{d}{dt}\left(\frac{p}{n^\gamma}\right) = \frac{\gamma-1}{n^\gamma}\left[\nabla\cdot\left(n\,\vec{\vec{\chi}}\cdot\nabla T\right) + S\right] \\
&\frac{\partial \mathbf{B}}{\partial t} = \nabla\times\left[\mathbf{v}\times\mathbf{B} - \eta\left(\mathbf{J} - \frac{3}{2}\frac{n\,\mathbf{B}\times\nabla T}{B^2}\right)\right]
\end{aligned} \tag{4.2}$$

Here $S(\mathbf{r},\varepsilon t)$ is the heating source. Note that we have included the thermal force in Faraday's law in order to prevent the simple, but physically unrealistic result that the pressure in the MHD stable region is driven to be uniform in space; that is, the pressure

would be unconfined if the thermal force is neglected. Also, although the thermal diffusivity is written as a tensor, the analysis shows that only the cross-field component enters into the analysis.

The model is reduced as follows. The background quantities $\overline{\rho}(r,\varepsilon t)$, $\overline{p}(r,\varepsilon t)$, $\overline{B}_\theta(r,\varepsilon t)$, and $\overline{v}_r(r,\varepsilon t)$ are the primary unknowns to be determined. For simplicity, we assume that the velocity of the background state of the plasma is due solely to transport (there is no large background flow velocity). This implies that we can neglect inertial effects in the momentum equation for the background state.

Consider next the perturbations. For $m = 0$ interchange modes, the perturbations are, by definition, functions only of (r,z,t). Also, the perturbed magnetic field has only a parallel component: $\tilde{\mathbf{B}} = \tilde{B}_\theta(r,z,t)\mathbf{e}_\theta$. In contrast, the perturbed velocity has no parallel component: $\tilde{\mathbf{v}} = \tilde{v}_r(r,z,t)\,\mathbf{e}_r + \tilde{v}_z(r,z,t)\,\mathbf{e}_z$. All perturbed quantities are assumed to be a sum over unstable interchange eigenfunctions:

$$\tilde{Q}(r,z,t) = \sum_n Q_n(r)\exp(-i\omega_n t + ik_n z) \tag{4.3}$$

where $k = n/R_0$ and R_0 is the major radius of the equivalent torus.

Under the above assumptions the starting equations reduce to

$$\begin{aligned}
&\frac{\partial n}{\partial t} + \nabla\cdot(n\mathbf{v}) = 0\\
&\frac{\partial s}{\partial t} + \nabla\cdot(s\mathbf{v}) = \frac{\gamma-1}{n^{\gamma-1}}\left[\nabla\cdot(n\,\ddot{\boldsymbol{\chi}}\cdot\nabla T) + S\right]\\
&\frac{\partial}{\partial t}\left(\frac{B_\theta}{r}\right) + \nabla\cdot\left(\frac{B_\theta}{r}\mathbf{v}\right) = \nabla\cdot\left[\frac{\eta}{\mu_0 r^2}\nabla(rB_\theta) + \frac{3}{2}\frac{\eta n}{rB_\theta}\nabla T\right]\\
&m_i n\left(\frac{\partial \mathbf{v}}{\partial t} + \mathbf{v}\cdot\nabla\mathbf{v}\right) = -\nabla\left(p + \frac{B_\theta^2}{2\mu_0}\right) - \frac{B_\theta^2}{\mu_0 r}
\end{aligned} \tag{4.4}$$

Here, $s = p/n^{\gamma-1}$ is a function related to the entropy per unit volume and ∇ represents the two-dimensional operator $\nabla = \mathbf{e}_r \partial/\partial r + \mathbf{e}_z \partial/\partial z$.

4.3.2 The magnetic field equation

To proceed we focus on the magnetic field equation. The various quantities are substituted and after a short calculation we obtain the unexpanded but cumbersome equation given by

$$\begin{aligned} &\frac{\partial}{\partial t}\left(\overline{B}_\theta + \tilde{B}_\theta\right) + \frac{\partial}{\partial r}\left(\overline{B}_\theta \overline{v}_r + \overline{B}_\theta \tilde{v}_r + \tilde{B}_\theta \overline{v}_r + \tilde{B}_\theta \tilde{v}_r\right) + \frac{\partial}{\partial z}\left(\overline{B}_\theta \tilde{v}_z + \tilde{B}_\theta \tilde{v}_z\right) \\ &\qquad = \frac{\partial}{\partial r}\left[\frac{\eta}{\mu_0 r}\frac{\partial}{\partial r}\left(r\overline{B}_\theta\right) + \frac{3}{2}\frac{\eta \overline{n}}{\overline{B}_\theta}\frac{\partial \overline{T}}{\partial r}\right] \end{aligned} \tag{4.5}$$

Note that both background and perturbation contributions have been included on the left hand side of the equation. However, the perturbations have been neglected on the right hand side since the classical transport terms are already assumed to be small compared to the MHD terms.

The next step is to average the equation over z to obtain the governing equation for the background magnetic field. The averaging procedure is defined as

$$\langle Q \rangle = \frac{1}{2\pi L}\int_0^{2\pi L} Q\, dz \tag{4.6}$$

where $L = 2\pi/k_1$ is the longest wavelength of the unstable perturbations and by definition $\langle \tilde{Q} \rangle = 0$. After averaging, Eq. (4.5) reduces to

$$\frac{\partial \overline{B}_\theta}{\partial t} + \frac{\partial}{\partial r}\left(\overline{B}_\theta \overline{v}_r\right) = -\frac{\partial}{\partial r}\left[\left\langle \tilde{B}_\theta \tilde{v}_r \right\rangle + \frac{2\eta \overline{T}^{3/4}}{\overline{B}_\theta}\frac{\partial}{\partial r}\left(\overline{n}\overline{T}^{1/4}\right)\right] \tag{4.7}$$

In deriving Eq. (4.7) we have used the background pressure balance relation

$$\frac{\partial \overline{p}}{\partial r} + \frac{\overline{B}_\theta}{\mu_0 r}\frac{\partial}{\partial r}\left(r\overline{B}_\theta\right) = 0 \tag{4.8}$$

obtained by averaging the momentum equation and neglecting inertial effects for the slowly evolving background state. Observe that the first term on the right hand side represents quasilinear transport while the second term corresponds to classical transport. Equation (4.7) can be further simplified by introducing the background flux function $\overline{\psi}\left(r,\varepsilon t\right)$ as follows

$$\overline{B}_\theta = \frac{\partial \overline{\psi}}{\partial r} \tag{4.9}$$

This allows us to integrate the equation yielding

$$\frac{\partial \overline{\psi}}{\partial t} + \overline{v}_r \frac{\partial \overline{\psi}}{\partial r} = -\left\langle \tilde{B}_\theta \tilde{v}_r \right\rangle - \frac{2\eta \overline{T}^{3/4}}{\overline{B}_\theta}\frac{\partial}{\partial r}\left(\overline{n}\overline{T}^{1/4}\right) \tag{4.10}$$

Here, the free integration function has been set to zero under the assumption that there is no external E_z field driving the toroidal current.

4.3.3 Flux coordinates

Equation (4.10) describes the evolution of the magnetic flux. It is useful because it allows us to introduce flux coordinates that define the reference frame with respect to which transport can be measured. The flux surface transformation is defined by

$$\begin{aligned} \overline{\psi} &= \overline{\psi}(r,t) \\ \tau &= t \end{aligned} \tag{4.11}$$

The critical relations required to carry out the analysis are easily calculated and are given by

$$\frac{\partial}{\partial r} = \overline{B}_\theta \frac{\partial}{\partial \overline{\psi}} \qquad \frac{\partial}{\partial t} = \frac{\partial}{\partial \tau} - \overline{B}_\theta r_\tau \frac{\partial}{\partial \overline{\psi}}$$
$$r_{\overline{\psi}} = \frac{1}{\overline{B}_\theta} \qquad r_\tau = -\frac{\overline{\psi}_t}{\overline{B}_\theta} \tag{4.12}$$

When the coordinate transformation is substituted into the flux evolution equation, the result is an explicit expression for the diffusion velocity measured with respect to the reference coordinate system.

$$\overline{v}_r - r_\tau = -\frac{\left\langle \tilde{B}_\theta \tilde{v}_r \right\rangle}{\overline{B}_\theta} - \frac{2\eta \overline{T}^{3/4}}{\overline{B}_\theta} \frac{\partial}{\partial \overline{\psi}} \left(\overline{n} \overline{T}^{1/4} \right) \tag{4.13}$$

This equation contains the essential information required to determine the transport evolution of the plasma particles and energy.

4.3.4 Particle and energy transport

The particle and energy transport equations are determined in a manner completely analogous to the derivation of the magnetic field equation. The expansions are substituted into the nonlinear equations and then averaged over z. The resulting equations are further simplified by eliminating the radial velocity by means of Eq. (4.13). After a straightforward but slightly lengthy calculation we obtain the following evolution equations for $\overline{n}$ and $\overline{s}$.

$$\frac{\partial}{\partial\tau}\left(\frac{r\overline{n}}{\overline{B}_\theta}\right)=-\frac{\partial}{\partial\overline{\psi}}\left\{r\left[\left\langle\tilde{n}\,\tilde{v}_r\right\rangle-\frac{\overline{n}}{\overline{B}_\theta}\left\langle\tilde{B}_\theta\tilde{v}_r\right\rangle-D_C\overline{B}_\theta\left(\frac{\partial\overline{n}}{\partial\overline{\psi}}+\frac{\overline{n}}{4\overline{T}}\frac{\partial\overline{T}}{\partial\overline{\psi}}\right)\right]\right\}$$

$$\frac{\partial}{\partial\tau}\left(\frac{r\overline{s}}{\overline{B}_\theta}\right)=-\frac{\partial}{\partial\overline{\psi}}\left\{r\left[\left\langle\tilde{s}\,\tilde{v}_r\right\rangle-\frac{\overline{s}}{\overline{B}_\theta}\left\langle\tilde{B}_\theta\tilde{v}_r\right\rangle-\frac{D_C\overline{B}_\theta\overline{s}}{n}\left(\frac{\partial\overline{n}}{\partial\overline{\psi}}+\frac{\overline{n}}{4\overline{T}}\frac{\partial\overline{T}}{\partial\overline{\psi}}\right)\right]\right\} \tag{4.14}$$

$$+\frac{\gamma-1}{\overline{n}^{\gamma-1}}\left[\frac{\partial}{\partial\overline{\psi}}\left(r\overline{n}\overline{B}_\theta\chi_C\frac{\partial\overline{T}}{\partial\overline{\psi}}\right)+\frac{r\langle S\rangle}{\overline{B}_\theta}\right]$$

Here, $D_C=2\eta\overline{n}\overline{T}/\overline{B}_\theta^2\sim\rho_e^2/\tau_{ei}$ and $\chi_C=2\overline{T}/m_i\omega_{ci}^2\tau_{ii}\sim\rho_i^2/\tau_{ii}$.

The final step in the derivation is to substitute for the perturbed quantities in order to obtain the quasilinear transport coefficients. This is easily accomplished by noting that the equations for the perturbed quantities are obtained by subtracting the z averaged equations from the exact nonlinear equations. As in the standard quasilinear procedure the nonlinear terms are neglected in the equations for the perturbed equations. Furthermore, as stated previously, the time scale for MHD instabilities is much faster than for classical transport. The implication is that it is a good approximation to neglect the classical transport terms in the perturbation equations. The net result of these considerations is that the perturbations satisfy the equations of ideal MHD. Specifically from the conservation of mass and the conservation of flux we obtain

$$\tilde{n}=-\xi\frac{\partial\overline{n}}{\partial r}-\overline{n}\,\nabla\cdot\boldsymbol{\xi}$$

$$\frac{\tilde{B}_\theta}{r}=-\xi\frac{\partial}{\partial r}\left(\frac{\tilde{B}_\theta}{r}\right)-\frac{\tilde{B}_\theta}{r}\nabla\cdot\boldsymbol{\xi} \tag{4.15}$$

where $\tilde{\mathbf{v}}\approx-i\omega\boldsymbol{\xi}=-i\omega\left(\xi\mathbf{e}_r+\xi_z\mathbf{e}_z\right)$.

From these expressions it follows that

$$\left\langle\tilde{n}\,\tilde{v}_r\right\rangle-\frac{\overline{n}}{\overline{B}_\theta}\left\langle\tilde{B}_\theta\tilde{v}_r\right\rangle=-D_Q\frac{\overline{B}_\theta^2}{r}\frac{\partial}{\partial\overline{\psi}}\left(\frac{r\overline{n}}{\overline{B}_\theta}\right)$$

$$\left\langle\tilde{s}\,\tilde{v}_r\right\rangle-\frac{\overline{s}}{\overline{B}_\theta}\left\langle\tilde{B}_\theta\tilde{v}_r\right\rangle=-D_Q\frac{\overline{B}_\theta^2}{r}\frac{\partial}{\partial\overline{\psi}}\left(\frac{r\overline{s}}{\overline{B}_\theta}\right) \tag{4.16}$$

where D_Q is the quasilinear diffusion coefficient given by

$$D_Q(\bar{\psi},\tau) = \sum_n \gamma_n |\xi_n|^2 \tag{4.17}$$

The final transport equations are obtained by substitution of Eq. (4.16) into Eq. (4.14). Also, since $D_C \sim (m_e/m_i)^{1/2}\chi_C$, it is a good approximation to neglect the D_C terms in the energy equations. This leads to

$$\begin{aligned}
\frac{\partial}{\partial\tau}\left(\frac{rn}{B_\theta}\right) &= \frac{\partial}{\partial\psi}\left[D_Q B_\theta^2 \frac{\partial}{\partial\psi}\left(\frac{rn}{B_\theta}\right) + rD_C B_\theta\left(\frac{\partial n}{\partial\psi} + \frac{n}{4T}\frac{\partial T}{\partial\psi}\right)\right] \\
\frac{\partial}{\partial\tau}\left(\frac{rs}{B_\theta}\right) &= \frac{\partial}{\partial\psi}\left[D_Q B_\theta^2 \frac{\partial}{\partial\psi}\left(\frac{rs}{B_\theta}\right)\right] + \frac{\gamma-1}{n^{\gamma-1}}\left[\frac{\partial}{\partial\psi}\left(r\chi_C n B_\theta \frac{\partial T}{\partial\psi}\right) + \frac{r\langle S\rangle}{B_\theta}\right]
\end{aligned} \tag{4.18}$$

where for simplicity of notation the over-bars have been suppressed on the background variables. These are the desired quasilinear transport equations. The basic unknowns are $p(\psi,\tau), n(\psi,\tau),$ and $r(\psi,\tau)$. The relationships to the variables appearing in Eq. (4.18) are as follows: $p = n^{\gamma-1}s$, $T = n^{\gamma-2}s/2$, and $B_\theta = 1/r_\psi$. One more equation is needed to close the system and this is the pressure balance relation for the background state. This equation determines $r(\psi)$ and in flux coordinates reduces to

$$\frac{\partial^2 r}{\partial\psi^2} = \frac{1}{r}\left(\frac{\partial r}{\partial\psi}\right)^2 + \frac{\partial p}{\partial\psi}\left(\frac{\partial r}{\partial\psi}\right)^3 \tag{4.19}$$

The derivation of the 1-D quasilinear transport equations is now complete.

4.4 One dimensional steady state transport

4.4.1 Reduction of the equations

One practical application of the quasilinear transport equations is to determine the steady state profiles of a hard core Z-pinch in which one portion of the profile is stable to interchange modes while another is unstable. The formulation of multi-region problem is carried out in this Section. It is also shown, by means of a model problem, how the formulation can be substantially simplified in the interesting regime where $D_Q \ll \chi_C$. Interestingly, the final results are closely coupled to the results of linear MHD stability although in the derivation of the quasilinear transport equations described above only the linearized mass and magnetic field equations have been used – no use has been made of the linearized momentum equation.

In steady state (i.e. $\partial / \partial \tau = 0$) the quasilinear equations can be simplified by reverting back to radial rather than flux coordinates since there is a one-to-one relation between ψ and $r: \psi(r,t) \to \psi(r)$. The steady state equations are thus given by

$$\begin{aligned} &\frac{\partial}{\partial r}\left[D_Q B_\theta \frac{\partial}{\partial r}\left(\frac{rn}{B_\theta} \right) + rD_C \left(\frac{\partial n}{\partial r} + \frac{n}{4T}\frac{\partial T}{\partial r} \right) \right] = 0 \\ &\frac{\partial}{\partial r}\left[D_Q B_\theta \frac{\partial}{\partial r}\left(\frac{rs}{B_\theta} \right) \right] + \frac{\gamma - 1}{n^{\gamma - 1}} \left[\frac{\partial}{\partial r}\left(r\chi_C n \frac{\partial T}{\partial r} \right) + r\langle S \rangle \right] = 0 \end{aligned} \tag{4.20}$$

Equation (4.20) can be written in a slightly different form that more closely shows the connection between the quasilinear transport terms and MHD interchange stability. By making use of the background radial pressure balance relation it can be shown that Eq. (4.20) can be rewritten as

$$\begin{aligned} &\frac{\partial}{\partial r}\left[D_Q n \left(K_n + \frac{\mu_0 p}{B_\theta^2} K_p \right) + rD_C \left(\frac{\partial n}{\partial r} + \frac{n}{4T}\frac{\partial T}{\partial r} \right) \right] = 0 \\ &\frac{\partial}{\partial r}\left\{ D_Q \frac{p}{n^{\gamma - 1}} \left[\left(1 + \frac{\mu_0 p}{B_\theta^2} \right) K_p - (\gamma - 1) K_n \right] \right\} + \frac{\gamma - 1}{n^{\gamma - 1}} \left[\frac{\partial}{\partial r}\left(r\chi_C n \frac{\partial T}{\partial r} \right) + r\langle S \rangle \right] = 0 \end{aligned} \tag{4.21}$$

where

$$K_p(r) = \frac{r}{p}\frac{dp}{dr} + \frac{2\gamma B_\theta^2}{B_\theta^2 + \mu_0 \gamma p}$$
$$K_n(r) = \frac{r}{n}\frac{dn}{dr} + \frac{2B_\theta^2}{B_\theta^2 + \mu_0 \gamma p} \tag{4.22}$$

Observe that the condition for stability against localized interchange modes, as first derived by Kadomstev [14], and is given by $K_p(r) > 0$. Intuitively we see that in the limit of a quasilinear diffusion dominance (i.e. $\frac{D_Q}{D_C} \to \infty$) the plasma profiles must relax to a state corresponding to $K_p \to 0$ and $K_n \to 0$. In other words, the profiles relax so as to just hover around the point of marginal stability.

It is also worth emphasizing that D_Q is large only in regions that are unstable to interchange modes. For a hard core Z-pinch only the outer portion of the pressure profile is potentially unstable. The implication is that to take this stable-unstable transition into account D_Q must be of the form

$$D_Q = D_Q(r) H(-K_p) \tag{4.23}$$

where H is the Heaviside step function.

Consider next the solution to the steady state transport equations for large but finite D_Q. In principle, we must solve the equations separately in the stable and unstable regions and then match the density and temperature plus the particle flux and energy flux across the critical radius corresponding to marginal stability. We show below, by means of a model problem, that for large D_Q, the solutions and the matching procedure are greatly simplified if our main goal is to calculate certain average quantities such as the plasma β or the energy confinement time τ_E.

4.4.2 Model problem

A model problem that captures the essential physics of the quasilinear transport analysis is as follows

$$\frac{1}{r}\frac{d}{dr}\left[rD_C \frac{dp}{dr} + rD_Q\left(\frac{dp}{dr}+\frac{2p}{r}\right)\right] + S = 0 \tag{4.24}$$

subject to boundary conditions $p'(0)=0,\ p(1)=p_w$. This simple model is devised only to illustrate the behavior of the system at high values of quasilinear diffusion coefficient $\frac{D_Q}{D_C} \gg 1$. The more realistic models of plasma would have $p(0) \approx 0$ as a boundary condition, instead of $p'(0)=0$. For simplicity we assume that $D_C, D_Q,$ and S are constants. The condition to excite an MHD instability, in analogy with the quasilinear model, is taken to be

$$\frac{dp}{dr}+\frac{2p}{r} \le 0 \tag{4.25}$$

As a reference case we can easily calculate the solution for purely classical transport (i.e. $D_Q = 0$ everywhere). The solution is given by

$$p = p_0\left(1+\varepsilon - r^2\right) \tag{4.26}$$

where $p_0 = S/4D_C$ and $\varepsilon = p_w / p_0$. The heating power is assumed to be sufficiently large so that the edge pressure is much less than the central pressure: $p_w / p_0 = \varepsilon \ll 1$.

It can easily be shown that the classical solution would be MHD unstable in the region $r_s^2 < r^2 < 1$ where $r_s^2 = (1+\varepsilon)/2 \approx 1/2$. Lastly, our end goal is to calculate the volume averaged pressure defined by

$$\langle p \rangle = 2\int_0^1 p\, r dr \tag{4.27}$$

A short calculation shows that for the case of classical transport

$$\langle p \rangle = \frac{p_0(1+2\varepsilon)}{2} \approx \frac{p_0}{2} \tag{4.28}$$

Consider now the model problem including quasilinear transport. We obtain the desired solutions by solving in the inner stable region $0 < r^2 < r_s^2$ using only classical transport (i.e. $D_Q = 0$). In the unstable region $r_s^2 < r^2 < 1$ we use the full equation with $D_Q \neq 0$. Note that at this point the marginally stable transition point r_s^2 is still an unknown quantity to be determined.

The solutions in each region are easily obtained and can be written as

$$\begin{aligned} &\text{Classical:} && p = p_0\left(c_1 - r^2\right) && 0 < r^2 < r_s^2 \\ &\text{Quasilinear:} && p = p_0\left(c_2 + \frac{c_3}{r^{2\alpha}} - \frac{\delta}{1+\delta} r^2\right) && r_s^2 < r^2 < 1 \end{aligned} \tag{4.29}$$

Here, the c_j are free integration constants, $\delta = D_C / 2D_Q \ll 1$, and $\alpha = 1/(1+2\delta)$.

The problem as it now stands has four unknown constants: $c_1, c_2, c_3,$ and r_s^2. These are determined by the following four conditions: (1) the wall condition $p(1) = p_w$, (2) the requirement that the classical solution be marginally stable at $r = r_s^-$, which is equivalent to $\left[p' + 2p/r\right]_{r=r_s^-} = 0$, (3) continuity of the pressure across the marginal stability transition point $\left[\!\left[p \right]\!\right]_{r=r} = 0$, and (4) continuity of the flux across the marginal stability transition point $\left[\!\left[p' \right]\!\right]_{r=r_s} = 0$. Note that the last condition is simplified because r_s corresponds to the point of marginal stability as dictated by condition (2). After a short calculation the unknown constants can be determined and substituted back into Eq. (4.29), yielding

$$\begin{aligned} &\text{Classical:} && p = p_0\left(2r_s^2 - r^2\right) && 0 < r^2 < r_s^2 \\ &\text{Quasilinear:} && p = p_0\left(\frac{1+2\delta}{1+\delta}\frac{r_s^{2+2\alpha}}{r^{2\alpha}} - \frac{\delta}{1+\delta}r^2\right) && r_s^2 < r^2 < 1 \end{aligned} \tag{4.30}$$

where

$$r_s^2 = \left[\frac{\varepsilon(1+\delta)+\delta}{1+2\delta}\right]^{\frac{1}{1+\alpha}} \tag{4.31}$$

The final quantity of interest is the average pressure which, when evaluated, has the following somewhat complex form

$$\langle p\rangle = p_0\left[\frac{(1+2\delta)^2}{2\delta(1+\delta)}\left(r_s^{2+2\alpha} - r_s^4\right) - \frac{\delta}{1+\delta}\frac{1-r_s^4}{2}\right] \tag{4.32}$$

In the interesting physical limit of large quasilinear diffusion, corresponding to $\delta \ll \varepsilon \ll 1$, the expressions become independent of δ and simplify to

$$\begin{aligned} r_s^2 &\approx \varepsilon^{1/2} \\ \langle p\rangle &= \frac{p_0}{2}\left(3\varepsilon - \varepsilon\ln\varepsilon\right) \end{aligned} \tag{4.33}$$

The key point of the model problem is to show how Eq. (4.33) can be obtained by a much simpler calculation by taking the small δ limit at the beginning, rather than the end of the calculation. The simpler procedure consists of solving the classical transport equations for the inner part of the profile and using the marginal stability condition to determine the pressure in the outer part of the profiles. Specifically, we need to solve

$$\begin{aligned} &\frac{1}{r}\frac{d}{dr}\left(rD_C\frac{dp}{dr}\right) + S = 0 && 0 < r^2 < r_s^2 \\ &\frac{dp}{dr} + \frac{2p}{r} = 0 && r_s^2 < r^2 < 1 \end{aligned} \tag{4.34}$$

The boundary conditions are (1) $p'(0) = 0$ and (2) $p(1) = p_w$. The marginal stability point is again determined by requiring that the classical solution satisfy

$\left[p' + 2p/r\right]_{r=r_s^-} = 0$. The main simplification that occurs involves the jump conditions. In this case only one jump condition is required $\left[\!\left[p\right]\!\right]_{r=r_s} = 0$. The problem is now completely specified. The solution is found to be

$$\begin{aligned} p &= p_0(2\varepsilon^{1/2} - r^2) \qquad & 0 < r^2 < \varepsilon^{1/2} \\ p &= p_0\varepsilon / r^2 \qquad & \varepsilon^{1/2} < r^2 < 1 \\ \langle p \rangle &= \frac{p_0}{2}\left(3\varepsilon - \varepsilon \ln \varepsilon\right) \end{aligned} \tag{4.35}$$

We see that the simplified calculation leads to the same value of $\langle p \rangle$ as that obtained from the small δ limit of the full quasilinear solution. A comparison of the radial profiles corresponding to classical transport, the full quasilinear transport, and the simplified quasilinear transport are illustrated in Fig. 4-2 for the case $\varepsilon = 5\times10^{-2}$ and $\delta = 5\times10^{-3}$.

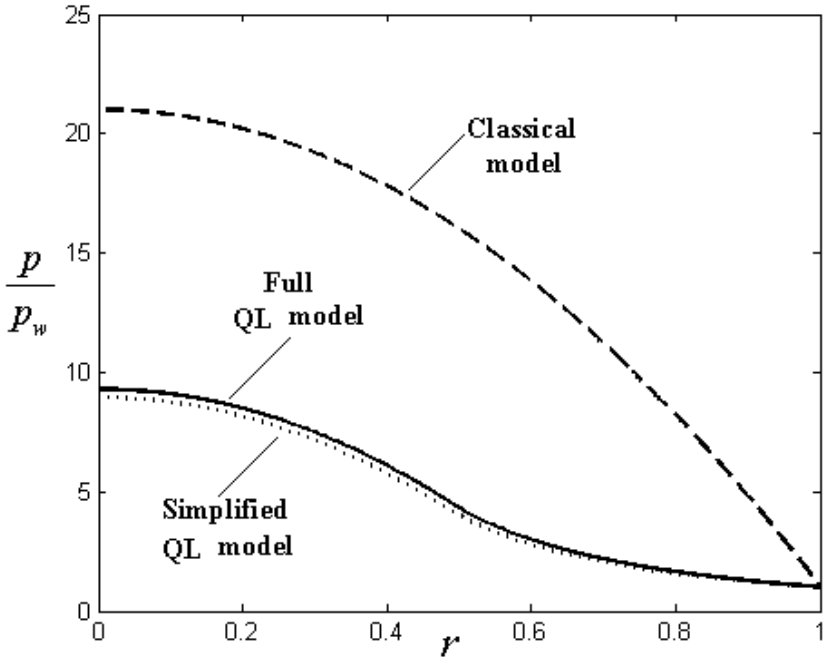

Figure 4-2 Radial pressure profiles for classical, full quasilinear and simplified quasilinear transport models.

Observe the similarity between the simple and full quasilinear profiles and the large reduction in peak pressure with respect to the classical profiles.

4.4.3 Final form of the cylindrical quasilinear calculation

Based on the results from the model problem we can now simplify the formulation for the cylindrical quasilinear analysis. A key result is that in the limit of large quasilinear diffusion the final results are independent of the value of D_Q. There is no need to evaluate the nonlinear saturated amplitudes. The model simplifies as follows.

Classical region:

$$\begin{aligned} &\frac{\partial}{\partial r}\left[rD_C\left(\frac{\partial n}{\partial r}+\frac{n}{4T}\frac{\partial T}{\partial r}\right)\right]=0 && \frac{\partial n(0)}{\partial r}=0 \\ &\frac{\partial}{\partial r}\left(r\chi_C n\frac{\partial T}{\partial r}\right)+r\langle S\rangle=0 && T(0)=0 \end{aligned} \tag{4.36}$$

Quasilinear region:

$$\begin{aligned} &K_p(r)=\frac{r}{p}\frac{dp}{dr}+\frac{2\gamma B_\theta^2}{B_\theta^2+\mu_0\gamma p}=0 && p(a)=p_w \\ &K_n(r)=\frac{r}{n}\frac{dn}{dr}+\frac{2B_\theta^2}{B_\theta^2+\mu_0\gamma p}=0 && n(a)=n_w \end{aligned} \tag{4.37}$$

The specification of the problem is completed by (1) requiring that the classical solutions satisfy the marginal stability criterion at $r=r_s^-$, corresponding to $K_p(r_s^-)=0$ and (2) matching the solutions across the stability interface which requires $[\![n]\!]_{r=r_s}=0$ and $[\![p]\!]_{r=r_s}=0$.

Once the solutions are obtained it is then a straightforward task to evaluate critical experimental parameters such as the average β and the energy confinement time τ_E. This calculation is carried out in detail in the next chapter.

4.5 Quasilinear transport in a toroidal dipole configuration

The analysis of quasilinear transport in a cylinder can be generalized to the toroidal case in a relatively straightforward manner. In a torus two additional features must be taken into account in the analysis, but these are not overly difficult tasks. First, the equilibrium geometry becomes two dimensional because of coupling to the poloidal angle. This difficulty is resolved by introducing flux coordinates. Second, because of the poloidal coupling the definition of an interchange mode is not as transparent as in a cylinder. To address this issue we focus attention on the fastest growing modes, corresponding to $n \to \infty$ where n is the toroidal mode number. These are the interchange modes and in this limit the definition becomes unambiguous.

For mathematical simplicity the analysis is carried out by taking the large D_Q limit at the outset. There are three steps in the procedure: (1) introduce flux coordinates, (2) derive the transport equations in the classical region, and (3) derive the transport equations in the quasilinear region.

4.5.1 Flux coordinates

For a closed line axisymmetric toroidal configuration it is convenient to carry out the analysis in terms of flux coordinates defined by (1) a "radial" coordinate $\psi(R,Z)$

corresponding to the flux, (2) a "poloidal" coordinate $l(R,Z)$ corresponding to arc length, and (3) a "toroidal" coordinate ζ corresponding to the usual polar angle. The coordinates are tied to the slowly varying, background magnetic flux. Clearly, by construction, the coordinates are orthogonal. Also, in the flux coordinate system time is denoted by τ. Thus the coordinate transformation is given by

$$\begin{aligned} \psi &= \psi\left(R,Z,t\right) \\ l &= l\left(R,Z,t\right) \\ \zeta &= -\phi \\ \tau &= t \end{aligned} \tag{4.38}$$

Note that (ψ,l,ζ) is a right-handed system. Next, the flux is defined by again neglecting inertial effects in the momentum equation for the background quantities. The implication is that ψ satisfies the Grad-Shafranov equation

$$R^2\nabla\cdot\left(\frac{\nabla\psi}{R^2}\right) = -\mu_0 R^2\frac{\partial p(\psi,t)}{\partial\psi} \tag{4.39}$$

The magnetic field is related to the flux by the relation

$$\mathbf{B} = \frac{1}{R}\nabla\psi\times\mathbf{e}_\phi \tag{4.40}$$

The poloidal coordinate is chosen to be arc length, defined as

$$\mathbf{B}\cdot\nabla l = B \tag{4.41}$$

Three useful relations for the analysis resulting from these definitions are given by

$$\begin{aligned} R\,dR\,dZ\,d\phi &= \frac{d\psi\,dl\,d\zeta}{B} \\ \nabla\cdot\mathbf{A} &= B\left[\frac{\partial}{\partial\psi}\left(RA_n\right)+\frac{\partial}{\partial l}\left(\frac{A_\parallel}{B}\right)\right]+\frac{1}{R}\frac{\partial A_\zeta}{\partial\zeta} \\ \frac{\partial}{\partial t} &= \frac{\partial}{\partial\tau}+\psi_t\frac{\partial}{\partial\psi}+l_t\frac{\partial}{\partial l} \end{aligned} \tag{4.42}$$

where $A_n = (\nabla\psi \cdot \mathbf{A})/RB$ and $A_{\|} = \mathbf{b}\cdot\mathbf{A}$ with $\mathbf{b} = \mathbf{B}/B$. Lastly, we need an expression for the volume contained within a given flux surface $\mathsf{v}(\psi)$. We define $V = (1/2\pi)\, d\mathsf{v}/d\psi$ from which it follows that

$$\begin{aligned} \mathsf{v}(\psi) &= 2\pi \int_0^{\psi} d\psi' \oint \frac{dl}{B} \\ V(\psi) &= \oint \frac{dl}{B} \end{aligned} \tag{4.43}$$

We are now ready to derive the transport equations.

4.5.2 Classical region

In the classical region the analysis is purely two dimensional (i.e. ψ, l) since by definition no perturbations exist which would introduce ζ dependence. The derivation begins by focusing on the equation for the toroidal flux function. As for the cylindrical case we write $\mathbf{B} = \nabla \times \left[(\psi/R)\mathbf{e}_{\phi} \right]$ and then integrate Faradays law, evaluating the $\mathbf{e}_{\phi}$ component from the resulting integrated expression. This yields

$$\frac{\partial \psi}{\partial t} + \mathbf{v}\cdot\nabla\psi = -\eta R^2 \left(\frac{\partial p}{\partial \psi} - \frac{3n}{2}\frac{\partial T}{\partial \psi} \right) \tag{4.44}$$

Note that $T = T(\psi, t)$. It does not depend on l because of the large parallel thermal conductivity.

Next, we introduce flux coordinates into this relation which yields an explicit expression for the normal component of velocity with respect to the coordinate velocity.

$$v_{\psi} + \frac{\psi_t}{RB} = -\frac{2\eta R T^{3/4}}{B}\frac{\partial}{\partial \psi}\left(n T^{1/4} \right) \tag{4.45}$$

Following the cylindrical analysis, we write the conservation of mass and energy relations in flux coordinates and then average over both ζ and l. After a slightly lengthy but nonetheless well established procedure we obtain two evolutionary equations for the background particle density and entropy density given by

$$\begin{aligned}\frac{\partial}{\partial\tau}\left(nV\right) &= \frac{\partial}{\partial\psi}\left(\overline{D}_C T^{3/4}\frac{\partial nT^{1/4}}{\partial\psi}\right)\\ \frac{\partial}{\partial\tau}\left(sV\right) &= \frac{\gamma-1}{n^{\gamma-1}}\frac{\partial}{\partial\psi}\left(n\overline{\chi}_C\frac{\partial T}{\partial\psi}\right)+\frac{\gamma-1}{n^{\gamma-1}}\left\langle S\right\rangle V\end{aligned} \tag{4.46}$$

where

$$\begin{aligned}\left\langle Q\right\rangle &= \frac{\oint Q\dfrac{dl}{B}}{\oint\dfrac{dl}{B}}\\ \overline{D}_C &= 2\eta nTV\left\langle R^2\right\rangle = V\left\langle R^2B^2D_C\right\rangle\\ \overline{\chi}_C &= V\left\langle R^2B^2\chi_C\right\rangle\end{aligned} \tag{4.47}$$

As for the cylindrical case we have neglected particle diffusion as compared to thermal diffusion in the entropy equation.

4.5.3 Quasilinear region

The analysis in the quasilinear region is in general three dimensional since the unstable perturbations are of the form $\tilde{Q}\left(\psi,l,\zeta,\tau\right)=\tilde{Q}\left(\psi,l\right)\exp\left(-i\omega\tau+in\zeta\right)$. However, previous analysis of the MHD stability of closed line systems [4] has shown that the most unstable modes, in terms of thresholds, are high n interchanges. This recognition, combined with the fact that quasilinear transport drives the profiles close to marginal stability, substantially simplifies the analysis. In this limit we can introduce a small

parameter $\delta = \gamma_n a / v_{Ti} \ll 1$. Here γ_n is the MHD growth rate, which is small since the system hovers near marginal stability. For small δ the form of the MHD perturbations simplifies as follows.

$$\begin{aligned}
\boldsymbol{\xi}(\psi,l) &\approx \boldsymbol{\xi}_\perp(\psi,l) + \delta^2 \boldsymbol{\xi}_\parallel(\psi,l) \\
\tilde{\mathbf{v}}(\psi,l) &\approx \tilde{\mathbf{v}}_\perp(\psi,l) + \delta^2 \tilde{\mathbf{v}}_\parallel(\psi,l) \\
\tilde{n}(\psi,l) &\approx \tilde{n}(\psi) + \delta^2 \tilde{n}_1(\psi,l) \\
\tilde{p}(\psi,l) &\approx \tilde{p}(\psi) + \delta^2 \tilde{p}_1(\psi,l) \\
\tilde{\mathbf{B}}(\psi,l) &\approx \tilde{\mathbf{B}}_\parallel(\psi,l) + \delta^2 \tilde{\mathbf{B}}_\perp(\psi,l)
\end{aligned} \tag{4.48}$$

Furthermore, for an interchange mode in toroidal geometry the "radial" component of the normalized displacement vector is nearly constant along a field line; that is

$$\nabla\psi \cdot \boldsymbol{\xi}(\psi,l) \approx X(\psi) + \delta^2 X_1(\psi,l) \tag{4.49}$$

The next step is to recall that as $D_Q \to \infty$ the perturbations in the quasilinear region satisfy the ideal MHD equations. All transport effects can be neglected because of the fast time scale associated with quasilinear diffusion.

Under this set of assumptions it is straightforward to show, in analogy with Eq. (4.13), that the magnetic field can be expressed in terms of a flux function. This equation, when rewritten in flux coordinates, yields an expression for the relative motion of the background fluid velocity with respect to the background flux coordinate.

$$v_\psi + \frac{1}{RB}\frac{\partial \psi}{\partial t} = -\frac{\tilde{v}_\psi \tilde{B}}{B} \tag{4.50}$$

Here the subscript "ψ" denotes normal component and $\tilde{B} = \left|\tilde{\mathbf{B}}_\parallel\right|$

The quasilinear equations describing the evolution of the background state are now obtained by averaging the density and energy equations over l and ζ, and then substituting Eq. (4.50), yielding

$$\frac{\partial}{\partial\tau}(nV) = -\frac{1}{2\pi}\int_0^{2\pi} d\zeta \oint dl \left\{ \frac{\partial}{\partial\psi}\left[R\tilde{v}_\psi \left(\tilde{n} - \frac{n}{B}\tilde{B} \right) \right] \right\}$$
$$\frac{\partial}{\partial\tau}(sV) = -\frac{1}{2\pi}\int_0^{2\pi} d\zeta \oint dl \left\{ \frac{\partial}{\partial\psi}\left[R\tilde{v}_\psi \left(\tilde{s} - \frac{s}{B}\tilde{B} \right) \right] \right\} \tag{4.51}$$

The final step in the analysis is to eliminate $\tilde{v}_n$, $\tilde{n}$, and $\tilde{s}$ using the linearized equations of ideal MHD stability. Only the conservation of mass and energy relations are required. Consistent with the assumptions made above we find that

$$\tilde{v}_\psi \approx \frac{1}{RB}\frac{\partial X}{\partial\tau} = \frac{1}{RB}\sum_n \gamma_n X_n(\psi)\exp(\gamma_n\tau + in\zeta)$$
$$\tilde{n} \approx -X\frac{\partial n}{\partial\psi} - n\nabla\cdot\boldsymbol{\xi}_\perp \tag{4.52}$$
$$\tilde{s} \approx -X\frac{\partial s}{\partial\psi} - s\nabla\cdot\boldsymbol{\xi}_\perp$$

The quasilinear evolution equations reduce to

$$\frac{\partial}{\partial\tau}(nV) = \frac{\partial}{\partial\psi}\left[\bar{D}_Q \frac{\partial}{\partial\psi}(nV) \right]$$
$$\frac{\partial}{\partial\tau}(sV) = \frac{\partial}{\partial\psi}\left[\bar{D}_Q \frac{\partial}{\partial\psi}(sV) \right] \tag{4.53}$$

where

$$\bar{D}_Q = \sum_n \gamma_n |X_n|^2 \tag{4.54}$$

These are the desired equations. Note that as in the cylindrical case no use has been made of the linearized momentum equation.

4.5.4 Final form of the toroidal quasilinear transport equations

The formulation of the steady state quasilinear transport equations can now be easily obtained by setting $\partial/\partial\tau = 0$ and specifying boundary and jump conditions as outlined in the cylindrical model problem. The results are as follows.

Classical region:

$$\begin{aligned} &\frac{\partial}{\partial\psi}\left(\bar{D}_C T^{3/4}\frac{\partial nT^{1/4}}{\partial\psi}\right) = 0 && \frac{\partial n(\psi_c)}{\partial\psi} = 0 \\ &\frac{\partial}{\partial\psi}\left(n\bar{\chi}_C\frac{\partial T}{\partial\psi}\right) + \langle S\rangle V = 0 && T(\psi_c) = 0 \end{aligned} \tag{4.55}$$

Quasilinear region:

$$\begin{aligned} &\frac{\partial nV}{\partial\psi} = 0 && n(\psi_w) = n_w \\ &\frac{\partial sV}{\partial\psi} = \frac{1}{(nV)^{\gamma-1}}\frac{\partial pV^\gamma}{\partial\psi} = 0 && s(\psi_w) = p_w / n_w^{\gamma-1} \end{aligned} \tag{4.56}$$

Jump conditions:

$$\begin{aligned} [\![n]\!]_{\psi_s} &= 0 \\ [\![p]\!]_{\psi_s} &= 0 \end{aligned} \tag{4.57}$$

Definition of ψ_s:

$$\left.\frac{\partial pV^\gamma}{\partial\psi}\right|_{\psi_s^-} = 0 \tag{4.58}$$

As in the cylindrical case the quasilinear energy equation coincides with the marginal stability criterion for interchange modes: $\partial pV^\gamma/\partial\psi \geq 0$.

Lastly, note that the equations in the quasilinear region can be rewritten in forms more closely analogous to the cylindrical results. A short calculation yields

$$-\frac{1}{\langle \kappa / RB \rangle}\left(\frac{1}{n}\frac{\partial n}{\partial \psi}\right)+\frac{2}{1+\mu_0 \gamma p \langle 1/B^2 \rangle}=0$$
$$-\frac{1}{\langle \kappa / RB \rangle}\left(\frac{1}{p}\frac{\partial p}{\partial \psi}\right)+\frac{2\gamma}{1+\mu_0 \gamma p \langle 1/B^2 \rangle}=0 \qquad (4.59)$$

where $\kappa = \mathbf{n}\cdot(\mathbf{b}\cdot\nabla\mathbf{b})$ is the normal component of the curvature.

The quasilinear toroidal dipole problem is now fully specified. When solved it leads to a prediction of the steady state profiles from which it is then straightforward to calculate macroscopic quantities of interest such as β and τ_E.

4.6 Numerical simulations

To understand the numerical simulations recall that the validity of the quasilinear transport model requires that several assumptions be satisfied. These assumptions can be quantified in terms of four characteristic time scales that appear in the problem. The longest time scale $\tau_C \simeq a^2/\chi_C$ corresponds to classical heat diffusion. Next in the hierarchy is the heating time $\tau_H \simeq p/S$. The assumption is that the plasma is trying to heat up faster than it can lose energy by classical heat conduction. The third time scale $\tau_Q \simeq a^2/D_Q$ is the quasilinear diffusion time. By definition quasilinear diffusion should dominate energy transport, preventing the plasma from reaching the high temperatures that would result from purely classical transport. The fastest time scale $\tau_M \simeq a/v_{Ti}$ corresponds to the characteristic growth rate of MHD instabilities and enters into the expression for D_Q. Thus, for quasilinear theory to be valid we require that

$$\tau_M \ll \tau_Q \ll \tau_H \ll \tau_C \qquad (4.60)$$

An equivalent interpretation in terms of perturbation amplitudes is as follows. The amplitudes of the MHD perturbations and the corresponding growth rates should be large enough so that quasilinear diffusion dominates the particle and energy transport but must be small enough so that the non-linear terms are unimportant.

The numerical simulations described in this Section have two primary objectives: (1) demonstrate that in appropriate parameter regimes experimental interest the quasilinear model accurately predicts plasma transport, and (2) determine the time evolution of the profiles and demonstrate the existence of the self-consistent steady state plasma profiles predicted by the quasilinear model. A key additional point is to assess the validity and accuracy of the numerical codes used for the simulations. This last point, as we shall see, is problematic because of the highly localized structure of the interchange eigenfunctions.

4.6.1 The numerical model

The code used to simulate the evolution of the plasma is a modified version of the earlier one-fluid code developed at University of Maryland [15]. The code solves the following system of equations

$$\begin{aligned}
&\text{Mass:} && \frac{\partial \rho}{\partial t} + \nabla \cdot (\rho \mathbf{v}) = 0 \\
&\text{Ohm's law:} && \frac{\partial \mathbf{B}}{\partial \mathrm{t}} = \nabla \times \left(\mathbf{v} \times \mathbf{B} \right) + \eta \nabla^2 \mathbf{B} \\
&\text{Momentum:} && \rho \left(\frac{\partial \mathbf{v}}{\partial t} + \mathbf{v} \cdot \nabla \mathbf{v} \right) = \mathbf{J} \times \mathbf{B} - \nabla p - \nabla \cdot \left(\mu \rho \nabla \mathbf{v} \right) \\
&\text{Energy:} && \frac{d}{dt} \left(\frac{p}{\rho^{\gamma}} \right) = \frac{2}{3\rho^{\gamma}} \left[S_E + \nabla \cdot \left(\rho \chi_{\perp} \nabla_{\perp} T + \rho \chi_{\parallel} \nabla_{\parallel} T \right) \right]
\end{aligned} \tag{4.61}$$

The geometry corresponds to a 2-D cylindrical hard core Z-pinch. The parameters $\mu, \eta, \chi_{\perp}$ and $\chi_{\parallel}$ are viscosity, resistivity, cross-field and parallel classical conduction coefficients respectively, with $\chi_{\parallel} \gg \chi_{\perp}$. Each of these coefficients is held constant during the simulation. As is characteristic of virtually all MHD fluid codes the transport coefficients are substantially larger than their actual physical values in order to insure good numerical convergence. This convergence requirement, we shall see, is the main feature that makes the interpretation of the numerical results problematic.

In the simulations the plasma is confined in a perfectly conducting cylindrical shell of radius $r_w = 1.1\ m$. The plasma is stabilized by an inner coil (i.e. the hard core) carrying the 10 kA current. The coil radius is $r_c = 0.1\ m$.

All functions are assumed to be periodic in the *z*-direction (i.e axial) with the length of the box $L = 3.0\ m$. Typical simulations were carried out with a grid resolution of $r \times z = 100 \times 300$. The temperature boundary conditions on the wall and coil walls assume that these surfaces are maintained at a constant temperature $T_c = T_w = 0.1\ eV$. The number of particles in the simulated volume is held fixed, so the plasma neither looses nor gains any additional mass. Finally, the energy source is modeled by a relatively broad Gaussian function $S_E \propto \exp\left[-\frac{(r - r_h)^2}{2\Delta r^2}\right]$ located $20\ cm$ away from the coil: $r_h = 0.3\ m$ and $\Delta r \approx 7\ cm$.

4.6.2 Weak heating simulation

The starting point for the simulations corresponds to a cold plasma with a flat density profile and the background temperature equal to the wall temperature $T(t=0)=T_w$. The first numerical experiment involves a low energy heating source that slowly heats the plasma to a level that is just slightly unstable against interchange modes. The *z*-averaged density and pressure profiles for the barely overheated plasma are illustrated in Fig. yy. Observe that the particle density is lowered in the plasma core due to both the frozen-in law, which carries particles within the magnetic flux tubes and slow collisional transport; that is, the finite resistivity creates a slow collisional particle flux, which drives particles into the regions of low temperature $\Gamma^p \propto -D_c \frac{\partial}{\partial r}(nT)$.

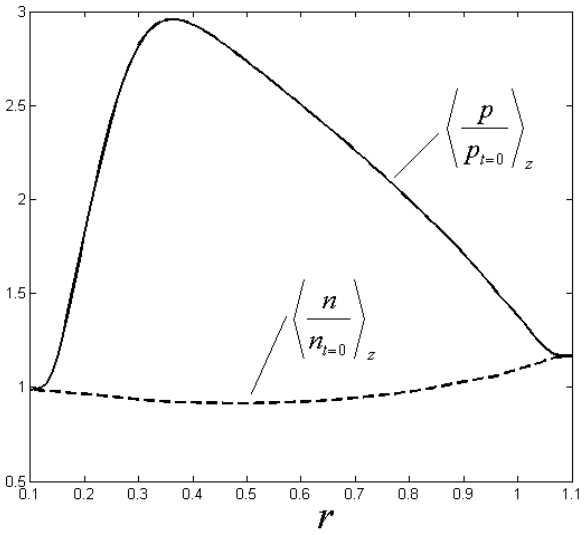

Figure 4-3 The pressure and density profiles of a slowly heated plasma

The stability condition is first violated close to the outer wall causing the plasma to develop a small-scale convective motion as illustrated on Fig. 4.4.

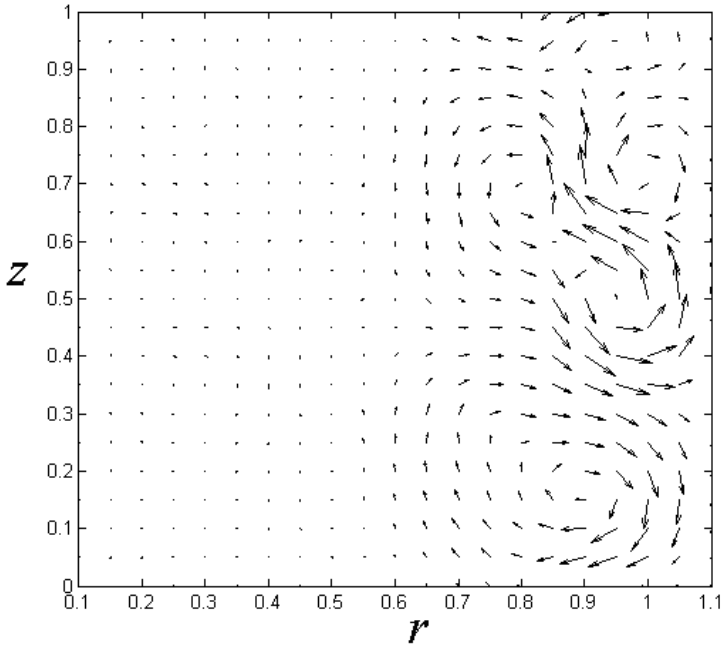

Figure 4-4 Convective cells in a slowly heated plasma. Plasma velocity field.

The amplitudes of the perturbations are quite small implying that quasilinear diffusion should dominate nonlinear effects. However, the growth rates of the modes are also quite small, implying that the quasilinear diffusion coefficient is small. In other words the additional quasilinear transport is weak compared to classical conduction (for the numerical values used in the simulations) and does not noticeably change plasma profiles.

The conclusion is that when the heating source is too small quasilinear transport occurs but is too weak to dominate over classical transport.

4.6.3 Strong heating simulation

The second set of numerical experiments involve a stronger external heating source, which deposits 10 times the maximum energy allowed by classical heat conduction

without violating the MHD stability criterion. As the instabilities develop, the plasma undergoes a macroscopic transformation and leading to the formation of fast moving convective cells. Such behavior can be analyzed only in a non-linear model. The interchange instabilities and corresponding non-linear transport dominate over collisional transport (i.e. only about 10% of the energy flux is due to collisional transport) and leads to an equilibration of the number of particles on any given flux tube.

Several different snapshots in the evolution of the particle density are illustrated in Fig. 4.5.

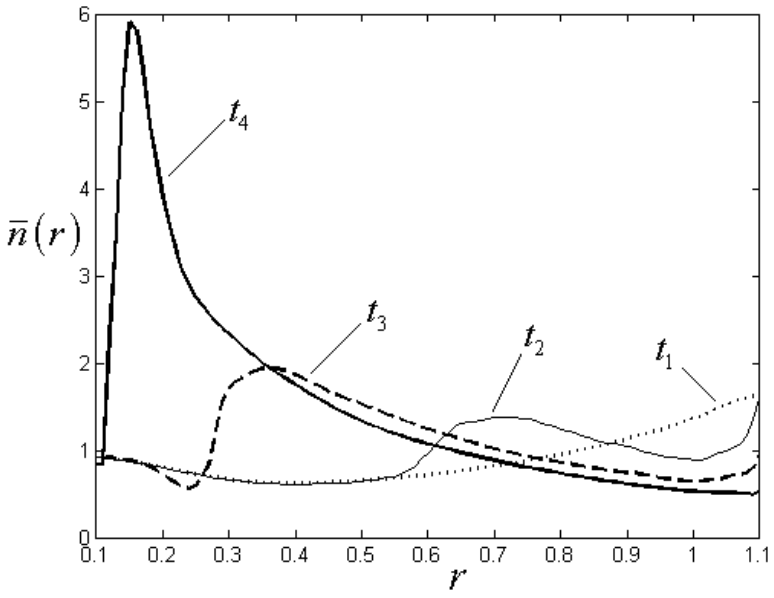

Figure 4-5 The snapshots of the "self-organizations" process. Time t1- before an instability is excited; t2-t4: different stages of self-organization

The eventual density profile is close to $\rho \sim 1/V \sim \left(\oint \frac{dl}{B} \right)^{-1}$ in the MHD unstable region, though it never reaches the exact "target" profile given by Eq. (4.37) due to the presence of collisional transport. The density profile in the MHD stable region is also seen to undergo significant changes on the MHD sound speed time scale due to the small volume of the region and the strong velocity changes in the convective cells, which bring

particles in or out of the inner region of plasma. The comparison of a density and pressure profiles at moment $t = t_4$ and the "target" profiles is illustrate on Fig. 4-6.

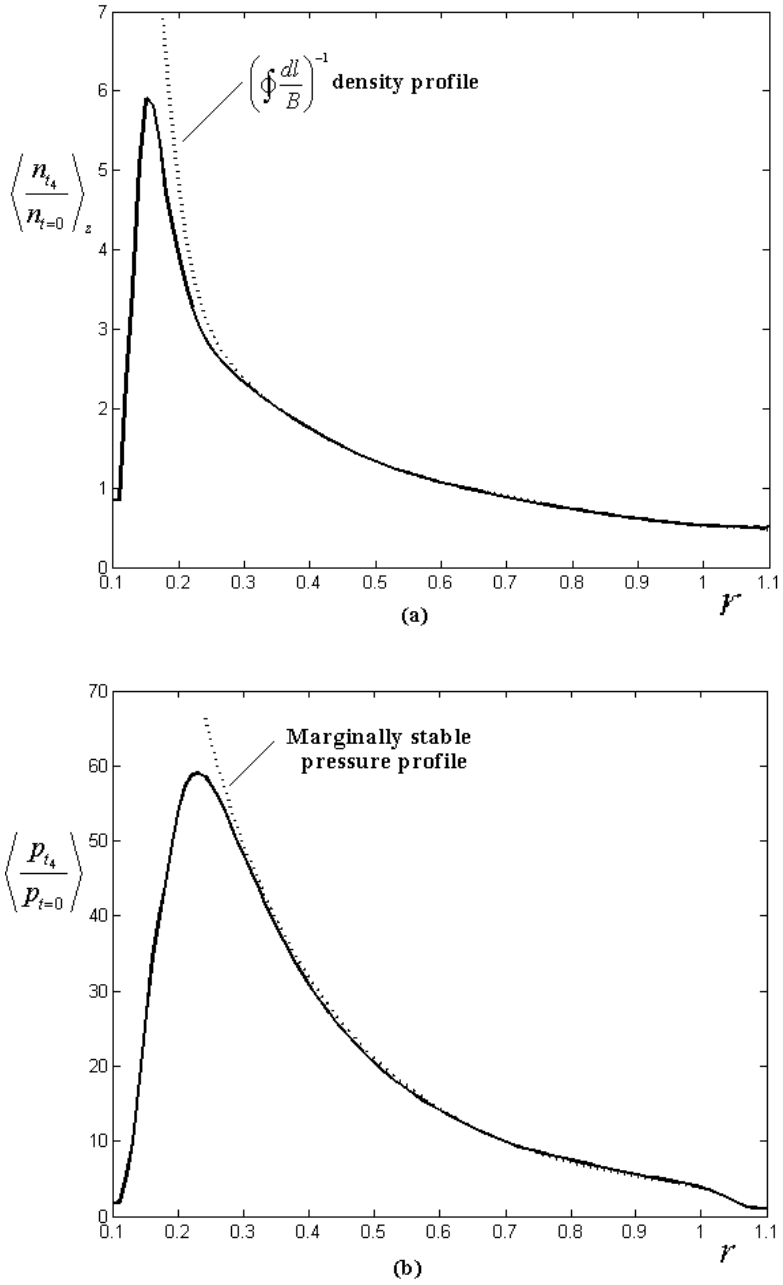

Figure 4-6 Comparison of (a) density and (b) pressure profiles at time t_4 with the quasilinear idealistic profiles given by Eq. (4.37)

The pressure profile evolves to its marginally stable form in the outer region, governed by Eq. (4.37) except in a narrow boundary layer at the outer wall, where viscosity plays

and important role. This type of self-organization and redistribution of plasma profiles to the marginally stable ones has also been reported by V.Makhnin *et.al*. [11].

The major mechanism of energy transfer in present simulations is the large-scale convective cell motion of the plasma, as seen in Fig.4-7.

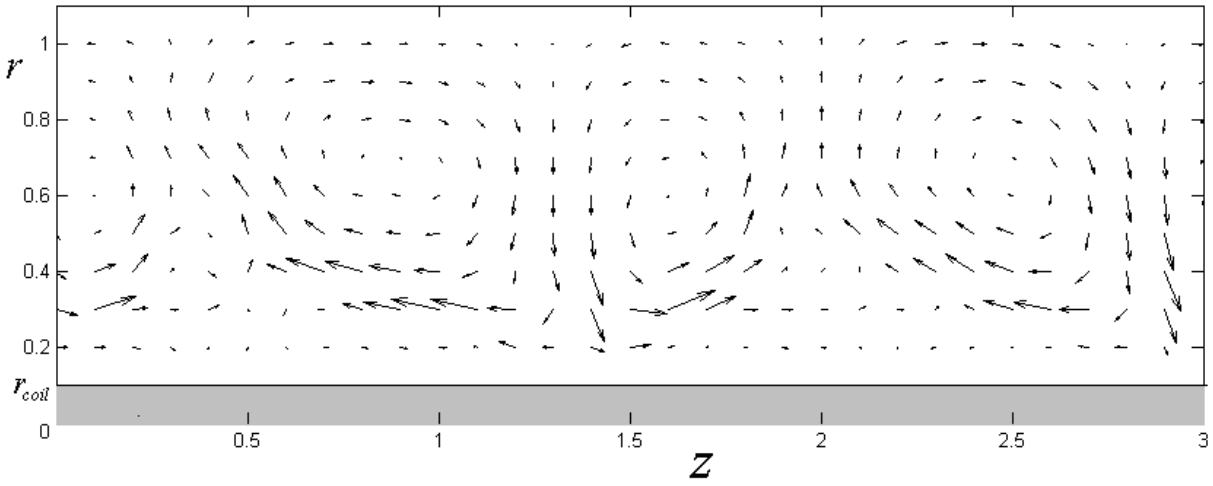

Figure 4-7 Typical velocity field profile in a plasma.

This behavior coincides with that seen by Pastukhov [9-10] in the quasi-stable state, while Makhnin reported smaller scale incoherent turbulence. Also, the development of large-scale convective cells in the non-linear regime is supported by the theoretical analysis done by Yoshizawa *et.al*.[16].

The existence of the global convective cells guards the plasma against disruptions by providing the mechanism to disperse the excessive heat from the plasma core. At the same time, during the formation of the convective cells and reorganization of the plasma profiles, a large radial velocity is observed only a few grid points away from the outer wall. That suggests that the rapid overheating of the plasma and the creation of strong non-linear perturbations may lead to large energy transport into the wall if a less ideal and more realistic boundary condition were used in the simulations.

4.6.4 Summary of simulation results

Quasilinear transport has not been seen to play the dominant role in energy transport in the present numerical studies. It was observable for the case of a weak energy source, but its magnitude was not large enough to dominate classical transport. For the high power heat source, quasilinear transport was present and large but was quickly replaced by the non-linear stage. A similar finding was reported by Pastukhov [9], when the transport in quasilinear stage started to smooth the profiles, but was not strong and had to be replaced by non-linear global plasma motion. We do not have clear evidence to conclude that quasilinear transport is short-lived by its basic nature and therefore is not strong enough to provide significant energy transport.

Alternatively, the absence of quasilinear dominated transport may simply point out the limitations of the numerical codes in describing finer scale perturbations. Specifically, the numerical grid restricts the entire spectra of the unstable perturbations to only the longer scale perturbations with the minimum wavelength equal to 5-7 grid points. This reduces the quasilinear diffusion coefficient to only the few slowest growing modes, thereby probably invalidating some of the assumptions for the validity of the theory. A finer resolution may partially improve the situation by including shorter wavelength modes, but even this may not be sufficient to capture the true micro-structured modes, which may well make the largest contribution to quasilinear transport.

Thus, while it is not clear because of numerical limitations whether or not quasilinear transport plays the decisive role, the fine-scale microturbulence transport remains the most desirable way of safeguarding against disruptions and reorganizing the plasma profiles, when instability is excited.

4.7 Conclusions

It has been analytically shown that the excitation of the interchange mode leads to new type of the energy and particle transport (quasilinear transport). The transport is colissionless with the major contribution coming from the short wavelength perturbations. This microturbulance transport effectively restores pressure profile to marginally stable one and density profile to $\rho \sim \left[\int \frac{dl}{B}\right]^{-1}$. The exact transport equations are derived for a Z-pinch magnetic configuration. Assuming only short-wavelength perturbations, the transport equations are generalized for an axisymmetric closed-field line toroidal geometry. The quasilinear transport analysis has been obtained with the assumption of a weakly unstable plasma profiles. To test the applicability of initial assumption, a set of non-linear numerical simulations has been carried out.

The simulations did not show that the quasilinear transport is strong enough to significantly change plasma profiles. Instead, the major transport mechanism observed in the unstable case was the non-linear global convective cells. The convection reorganized the pressure and density profile to the steady-state target profiles, described by the set of Equations (4.36-4.37).

However, this discrepancy may be explained by the natural limitations of the numerical codes, which cannot adequately describe microturbulences due to finite grid size.

Regardless of the exact transport mechanism, both analytically demonstrated quasilinear and numerically observed non-linear transport lead to the same conclusion that the interchange mode in closed-field line geometry is safeguarded against disruptions. The plasma profiles in the MHD unstable region closely follow the profiles described by the set of derived ideal equations (4.36-4.37). This finding may be used to determine the energy confinement time and other figures of merit for a given magnetic configuration.

Chapter 5

5 Theoretical prediction of β and τ_E in a hardcore Z-pinch

5.1 Introduction

The goal of this analysis is to obtain a theoretical prediction for the energy confinement time τ_E and maximum plasma β in a hardcore Z-pinch configuration, the cylindrical limit of the levitated dipole concept as embodied in the Levitated Dipole Experiment (LDX) [2,3]. These are critical figures of merit for any magnetic fusion concept. Their values depend on the magneto-hydrodynamic (MHD) and micro stability properties of the magnetic geometry as well as on experimentally controlled parameters such as the heating power, particle density, coil current, and plasma-wall interface.

To put the problem in perspective recall that the tokamak community has been working for decades to obtain a first principles understanding of anomalous heat transport, an effort that has only recently come close to fruition. With a much newer and much smaller program one might ask how the LDX community expects to achieve the same end goal in such a short time. The answer is that in some ways the LDX physics, although anomalous, is simpler than that of the tokamak. Specifically, tokamaks typically operate in a regime that is MHD stable and the anomalies are due to the more complicated, nonlinear evolution of weaker instabilities such as the ion temperature gradient mode, the electron temperature gradient mode, and the trapped electron mode [4]. The operation of a tokamak too close to the MHD "Troyon stability limit" is

inherently dangerous due to potential plasma disruptions, which can cause physical damage to the device. The stability of the levitated dipole on the other hand will likely be dominated by the ideal MHD interchange mode. It is believed that violation of the MHD interchange stability limit will result in a "soft-landing", relaxing the pressure to its marginally stable profile [see chapter 4 or reference 1]. If correct, this would give scientists the freedom to conduct experiments very close to the MHD stability limit. Therefore a simpler model, accompanied by a simpler analysis may hopefully lead to a reasonably accurate prediction in a relatively short time.

In terms of comparative physics note that both the levitated dipole and the tokamak can be driven MHD unstable by unfavorable magnetic field line curvature. One specific tokamak instability, the localized interchange mode, is usually easily stabilized by magnetic shear. This effect is absent in a closed line configuration such as LDX. Instead, interchange stability, which is the strictest limitation in LDX, is provided by plasma compressibility.

At present, no direct attempts have been made to predict the energy confinement time and beta in the LDX, although several implicit attempts have been made by the LDX community by calculating expected plasma pressure profiles. It is worthwhile to review these calculations before describing the present calculation. One of the first calculations is due to Garnier *et.al*. [5]. This calculation assumed an interchange stable pressure profile which obeyed the marginal stability condition outside of the energy source and was a polynomial function in the inner region of plasma. This approach is presently used by the LDX experimental team for reconstruction purposes [6].

Ricci, Rogers and Dorland have also recently run the non-linear GS2 code to estimate particle transport in LDX [7]. Other examples of pressure profile calculations involve

analytical equilibrium profile and stability properties in the ideal point dipole geometry, carried out by Krasheninnikov, Catto and Hazeltine [8,9]. Recently, Guazzotto and Freidberg have presented numerical calculations predicting the equilibrium beta limit for the actual LDX geometry with and without flow [10].

Along a different path, a nonlinear numerical simulation has been carried out by Pastukhov and Chudin [11,12]. They use a time dependent, reduced MHD model in a cylindrical geometry to model a hard core Z-pinch. Their results show that a strongly heated plasma transports away all excess energy through chaotic large-scale convective cells. The end result is a quasi-static pressure profile that hovers near the theoretical marginally stable profile.

Each of these calculations sheds valuable insight into the behavior of transport in a levitated dipole. However, none actually derives simple analytic scaling relations showing the dependence of τ_E and β on plasma parameters, similar to the L-mode and H-mode scaling relations for a tokamak. This is the goal of the present work.

The approach taken to achieve this goal is as follows. The plasma profile is separated into two regions. In the first region, near the levitation coil, the plasma is MHD stable. Here, a simple transport model is used to determine the steady state pressure, density, and magnetic field profiles. The transport coefficients correspond to their classical values as derived by Braginskii [13]. Clearly this is an optimistic assumption.

In the second outer region of the plasma beyond the pressure peak, the plasma is susceptible to the $m = 0$ interchange instability. Based on the quasilinear analysis of the interchange instability evolution as described in the accompanying paper [1] we assume the plasma relaxes to its marginal state in accordance with the stability criterion first given by Kadomstev [14]. The transition between the two regions is defined as that point

in which the local pressure gradient resulting from classical transport just matches the critical pressure gradient predicted by Kadomstev.

This procedure leads to explicit expressions for the pressure, density, and magnetic field profiles which can then be easily used to evaluate τ_E and β. It is worth noting that the scaling relations obtained here should be qualitatively valid for the toroidal LDX configuration. However, there may be important quantitative differences because of the tight aspect ratio in the actual LDX experiment. With this in mind our results show that a hardcore Z-pinch model of LDX predicts an energy confinement time $\tau_E = 2.3\times10^{-2}$ seconds and a corresponding average $\beta = 2.3\cdot10^{-3}$ for an input heating power of 30 kW, a levitation coil current of 1.3 MA, an edge temperature of 10eV and an edge density $1.7\times10^{17} m^{-3}$. Time will tell if the experimental performance matches the theoretical predictions.

The chapter is organized as follows: In Section II the MHD-transport model including sources is defined for both the MHD stable and unstable region. Section III contains several simple reference calculations using standard classical and anomalous transport models ignoring the effect of MHD instabilities. In Section IV simple analytic expressions are derived for τ_E and β using a low β, localized heating source approximation. Finally, Section V presents the numerical calculation of τ_E and β, obtained using more realistic profiles from the actual LDX experiment. From these results we compute "empirical" scaling relations for τ_E and β as a function of experimental parameters and geometry, which then can be tested in future LDX experiments

5.2 The MHD-Transport model

5.2.1 The MHD stable region

The starting point for the analysis is the definition of the MHD-Transport model. The geometry of interest is shown in Fig. 1.

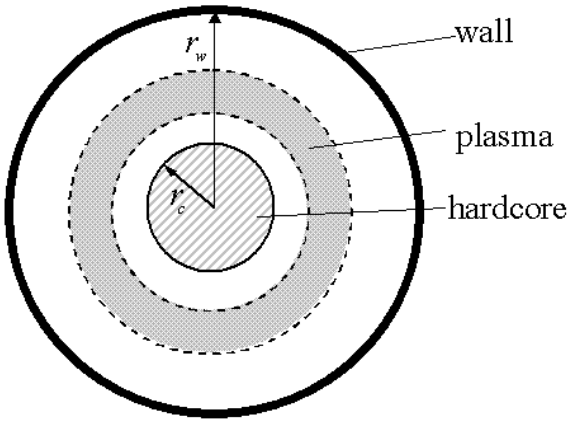

Figure 5-1 Hardcore Z-pinch model of LDX

In the region of the profile that is MHD stable, near the levitation coil, we use a standard single fluid transport model. For simplicity viscosity is neglected and it is assumed that $T_e = T_i \equiv T$. The non-trivial transport coefficients are the perpendicular ion thermal conductivity χ and the ambipolar particle diffusion coefficient D. In the MHD stable region these are given by their classical values as derived by Braginskii [13]. We focus on the steady state behavior of the plasma. Therefore the non-trivial field quantities, $p, n, T, \mathbf{B} = B\mathbf{e}_\theta$ and $\mathbf{u} = u\mathbf{e}_r$, are only functions of r. With these assumptions the plasma behavior in the stable region is described by the Braginskii transport equations

Mass: $$\frac{1}{r}\frac{d}{dr}(rnu)=0$$

Ohm's law: $$nu=-D\left(\frac{dn}{dr}+\frac{n}{4T}\frac{dT}{dr}\right)$$
$$\approx -D\frac{dn}{dr}$$

Momentum: $$\frac{B}{\mu_0 r}\frac{d}{dr}(rB)+\frac{dp}{dr}=-\rho u\frac{du}{dr} \qquad (5.1)$$
$$\approx 0$$

Energy: $$\frac{1}{r}\frac{d}{dr}\left(rn\chi\frac{dT}{dr}\right)+S_E=\frac{3}{2}u\frac{dp}{dr}+\frac{5}{2}\frac{p}{r}\frac{d}{dr}(ru)-\eta_\perp J_\perp^2$$
$$\approx 0$$

where

$$\chi=\frac{r_{Li}^2}{\tau_i}$$
$$D=\left(\frac{m_e}{2m_i}\right)^{1/2}\chi \qquad (5.2)$$
$$r_{Li}^2=\frac{2m_iT}{e^2B^2}$$
$$\tau_i=12\pi^{3/2}\frac{\varepsilon_0^2 m_i^{1/2}T^{3/2}}{ne^4\ln\Lambda}$$

Note that several approximations have been made which can be justified as follows. In the expression for the particle flux we neglect the $(n/4T)(dT/dr)$ contribution. This term essentially forces $n\sim 1/T^{1/4}$ and leads to un-physically large values of the density near the coil and the wall where the temperature is low. In these regions other physics (i.e. ionization and recombination) becomes important resulting in much smoother profiles. Neglecting the $(n/4T)(dT/dr)$ term from the outset avoids this difficulty and results in density profiles much closer to practical experimental situations.

The next approximation involves the momentum equation. Here, we neglect inertia because of the slow transport time scale. Lastly, in the energy equation there are two approximations. First, ohmic heating is neglected since it is usually small compared to the external heating power (i.e. $\eta_\perp J_\perp^2 \ll S_E$) in a levitated dipole. Second, we neglect compression, convection, and electron thermal conduction losses, which for most plasmas are small compared to the ion thermal conduction losses (i.e. $D \sim \chi_e \ll \chi_i$)

Combining these approximations and eliminating the radial velocity u leads to the desired set of fluid transport equations in the MHD stable region.

$$\begin{aligned} &\frac{1}{r}\frac{d}{dr}\left(rD\frac{dn}{dr}\right)=0 && \text{(mass)} \\ &\frac{B}{\mu_0 r}\frac{d}{dr}(rB)+\frac{dp}{dr}=0 && \text{(momentum)} \\ &\frac{1}{r}\frac{d}{dr}\left(rn\chi\frac{dT}{dr}\right)+S_E=0 && \text{(energy)} \end{aligned} \tag{5.3}$$

For boundary conditions we assume that at the surface of the levitation coil, $r = r_c$, there is complete recycling of the particle flux. In terms of maximizing the total number of particles in the plasma this is an optimistic assumption. The corresponding boundary condition is given by

$$\left.\frac{dn}{dr}\right|_{r_c} = 0 \tag{5.4}$$

For simplicity, the boundary condition on T at the levitation coil is modeled by a perfect heat sink.

$$T\big|_{r_c} = 0 \tag{5.5}$$

There is also a boundary condition on the magnetic field. On the surface of the levitation coil Ampere's law requires that

$$B\big|_{r_c} = \frac{\mu_0 I_c}{2\pi r_c} \tag{5.6}$$

Here, I_c is the current flowing in the levitation coil. The quantity I_c is an input parameter that appears in the scaling relations.

We also require jump conditions across the stable-unstable boundary in the plasma. These are discussed shortly, after the discussion of the model for the MHD-unstable region.

5.2.2 The MHD unstable region

The model used in the MHD unstable region, beyond the peak pressure, is based on the quasilinear analysis of the interchange instability. For background, recall that a linear Z-pinch is potentially unstable to two ideal MHD modes [14]: (1) the $m = 0$ interchange mode and (2) the $m = 1$ helical mode. The presence of the hardcore has a strong stabilizing effect on the $m = 1$ mode so that in general its critical β for instability is higher than that of the $m = 0$ mode.

Furthermore, resistivity does not alter the $m = 0$ stability condition. There is no shear stabilization to be mitigated by resistivity. Also, resistive modes for $m \neq 0$ are excited only when the interchange mode is already unstable, as has been shown by Simakov and Catto [15]. Lastly, for simplicity, all electrostatic and kinetic modes are neglected in this study, which is an optimistic assumption.

The conclusion is that the ideal MHD $m = 0$ interchange instability is the most dangerous mode in a levitated dipole and the analysis therefore focuses on this mode.

The quasilinear theory of the interchange mode shows that as the plasma is gradually heated from a cold initial state, its pressure profile evolves in such a way that it hovers around the marginally stable boundary. The marginal stability condition for interchange modes was first derived by Kadomstev [14] and is given below. In addition, the quasilinear theory predicts that in this marginally stable region the density profile evolves to a state in which the number of particles confined in any given flux tube is independent of radius, as first conjectured by Pastukhov and Chudin [11,12]. These two results from quasilinear theory, combined with the MHD pressure balance relation represent the profile model for the MHD unstable region.

$$\begin{aligned} &\frac{r}{p}\frac{dp}{dr} + \frac{2\gamma B^2}{B^2 + \mu_0 \gamma p} = 0 && \text{(Kadomstev criterion)} \\ &\frac{r}{n}\frac{dn}{dr} + \frac{2B^2}{B^2 + \mu_0 \gamma p} = 0 && \text{(density-flux tube relation)} \\ &\frac{B}{\mu_0 r}\frac{d}{dr}(rB) + \frac{dp}{dr} = 0 && \text{(pressure balance)} \end{aligned} \qquad (5.7)$$

In deriving these results it has been assumed that the quasilinear diffusion coefficient

$$D_Q = \sum_n \omega_i(k_n)\left|\xi_n\right|^2 \qquad \text{(sum over unstable modes)} \qquad (5.8)$$

satisfies two inequalities. First, it must be large enough so that anomalous transport dominates classical transport: $D_Q \gg \chi$. Second, it must be small enough so that nonlinear mode coupling can be neglected.

The boundary conditions assume that a source injects particles at the outer edge of the plasma establishing any desired plasma density. This is equivalent to specifying

$$n\big|_{r_w} = n_w \qquad (5.9)$$

The quantity n_w is an input parameter. Note that there is a maximum value for n_w determined by the requirement that the maximum density within the plasma must satisfy the condition $\omega_{pe}^2 \le \omega_{ce}^2$ in order for electron cyclotron heating to be effective.

The edge temperature condition is set by the wall properties for a limiter type plasma-wall interaction or by the scrape-off layer properties when a divertor is used. In either case, the boundary condition can be written as

$$T\big|_{r_w} = T_w \tag{5.10}$$

where T_w is an input parameter. Its value will be low for a limiter and higher for a divertor.

Lastly, Ampere's law imposes a boundary condition on the edge magnetic field that can be written as

$$B\big|_{r_w} = \frac{\mu_0 (I_c + I_p)}{2\pi r_w} \tag{5.11}$$

where I_p is the plasma current.

To complete the model we now need to specify the jump conditions across the stable-unstable boundary.

5.2.3 The jump conditions

The quasilinear analysis shows, not unexpectedly, that across the stable-unstable boundary, defined as $r = r_s$, the density, pressure, and magnetic field must be continuous.

$$\begin{aligned} [\![n]\!]_{r_s} &= 0 \\ [\![p]\!]_{r_s} &= 0 \\ [\![B]\!]_{r_s} &= 0 \end{aligned} \tag{5.12}$$

The situation with respect to the continuity of the fluxes is slightly complicated. The actual quasilinear diffusion equations are second order differential equations, which then require that the fluxes be continuous across the boundary. Even so, the quasilinear analysis also shows that when $D_Q \gg \chi$ the fluxes change rapidly within a narrow transition layer at the stability-instability boundary. The consequence is that an accurate approximation to the profiles is obtained by ignoring to leading order in χ / D_Q the flux contributions from the stable region. This allows us to integrate the corresponding transport equations in the unstable region one time, resulting in the two first order differential equations appearing in Eq. (5.7). These are the only conditions required for the complete solution. This important point is explicitly demonstrated in the accompanying paper describing the quasilinear analysis.

There is one last condition required to close the system, one that determines the location of the stability-instability boundary. The boundary location corresponds to the point where the pressure gradient in the classical region just equals the critical marginal stability value in the unstable region. Mathematically, the value of r_s is determined by requiring that

$$\left[\frac{r}{p}\frac{dp}{dr} + \frac{2\gamma B^2}{B^2 + 2\mu_0 \gamma p} \right]_{r_s^-} = 0 \tag{5.13}$$

This condition implies that in the region $r_c \le r \le r_s$ the plasma is stable against the interchange mode and classical transport should apply. In the region $r_s \le r \le r_w$ the classical transport profiles would violate the MHD stability condition. Here, the profiles relax to their marginal stability profiles as determined by quasilinear theory. The actual situation is somewhat more complicated and is discussed in more detail as the calculation

progresses. Looking ahead, the end result is that Eq. (5.13) is indeed correct but that there is a subsidiary constraint on the minimum heating power that must be satisfied. For practical situations this is usually accomplished quite easily.

5.3 The reference cases

In this section τ_E and β are calculated for two reference cases that serve as a basis for comparison with the quasilinear transport model. The two cases correspond to (1) classical transport over the entire plasma and (2) Bohm transport over the entire plasma. To make calculations analytically tractable, the localized energy source in all reference cases is approximated by a delta function.

5.3.1 Classical transport

Consider the case of classical transport. For analytic simplicity we focus on the low β regime where the magnetic field can be accurately approximated by

$$B_\theta(r) \approx \frac{\mu_0 I_c}{2\pi r} \tag{5.14}$$

Here, I_c is the current flowing in the levitation coil. The relevant equations and boundary conditions are given by

$$\begin{aligned} &\frac{1}{r}\frac{d}{dr}\left(rD_C\frac{dn}{dr}\right)=0 && \frac{dn(r_c)}{dr}=0,\ \ n(r_w)=n_w \\ &\frac{1}{r}\frac{d}{dr}\left(rn\chi_C\frac{dT}{dr}\right)=-S_0\delta(r-r_h) && T(r_c)=T(r_w)=0 \end{aligned} \tag{5.15}$$

The solution to the density equation is easily found:

$$n(r) = n_w = const. \tag{5.16}$$

The density is uniform across the plasma.

The energy equation can be simplified as follows. First note that the wall edge temperature appearing in the boundary conditions has been set to zero: $T_w = 0$. Even for very modest heating powers the profiles are only weakly dependent on this parameter. Thus, it can be set to zero with a negligible error. Next, the source amplitude S_0 is related to the total input power P by the relation

$$S_0 = \frac{P}{4\pi^2 R_0 r_h} \tag{5.17}$$

The Braginskii thermal diffusivity coefficient has already been specified in Eq. (5.2).

Lastly, we normalize the radius to the coil radius: $x = r / r_c$. A short calculation then yields a simplified form for the energy equation.

$$\begin{aligned} &\frac{1}{x}\frac{d}{dx}\left(\frac{x^3}{T_V^{1/2}}\frac{dT_V}{dx}\right) = -\alpha_C \delta(x - x_h) \\ &\alpha_C = 3.0\times 10^4 \frac{P_K I_M^2}{R_0 r_h r_c n_{\max}^2} \end{aligned} \tag{5.18}$$

Here, we have converted to practical units as follows: $T_V\,(eV), I_M\,(MA), P_K\,(kW)$, and $n_{\max}\,(10^{17} m^{-3})$.

The solution to Eq. (5.18) is easily found. Simple analytic expressions are obtained if we consider the reasonably realistic geometric regime $1 \ll x_h \ll x_w$. In this regime the solution can be expressed as

$$\begin{aligned} T_V &\approx \left(\frac{\alpha_C}{4x_h}\right)^2 \left(1 - \frac{1}{x^2}\right)^2 \qquad 1 \le x \le x_h \\ T_V &\approx \left(\frac{\alpha_C x_h}{4}\right)^2 \left(\frac{1}{x^2} - \frac{1}{x_w^2}\right)^2 \qquad x_h \le x \le x_w \end{aligned} \tag{5.19}$$

From the solution, three interesting, experimentally relevant quantities can be evaluated: (1) the energy confinement time τ_E, (2) the average plasma beta $\bar{\beta}$, and (3) the maximum temperature $T_{\max}$. These are defined and given by

$$\begin{aligned}
\tau_E &\equiv \frac{3\int nTd\mathbf{r}}{P} = 1.1\times 10^5 \frac{P_K I_M^4}{R_0 r_h^2 n_{\max}^3} \quad \text{sec} \\
\bar{\beta} &\equiv \frac{2\mu_0 \langle p \rangle}{B_\theta^2(r_w)} = 2.3\times 10^2 \frac{P_K^2 I_M^2}{R_0^2 r_h^2 n_{\max}^3} \\
T_{\max} &= 5.6\times 10^7 \frac{P_K^2 I_M^4}{R_0^2 r_h^4 n_{\max}^4} \quad \text{eV}
\end{aligned} \tag{5.20}$$

Observe, as expected, the very favorable scaling with power and current resulting from classical transport. For the anticipated LDX parameters listed in Table 1,

$r_c(m)$	$r_h(m)$	$r_w(m)$	$R_0(m)$	$n_{wall}\left(10^{17}m^{-3}\right)$	$P_K(kW)$	$I_M(MA)$	$T_w(eV)$
0.15	0.30	1.95	0.38	1.73	30	1.3	10

Table 5-1 Anticipated LDX parameters

we find that $\tau_E = 5.3\times 10^7$ seconds. This is an enormously optimistic value. In fact the confinement is so good that $\bar{\beta} > 1$, clearly violating the original low β approximation. The approximation is only valid for sufficiently low heating powers satisfying $P \le 10W$. At higher values of the heating power, both the low β approximation fails and the interchange mode is excited. Clearly, this region of validity is uninteresting from the experimental standpoint. At critical heating power $P \approx 10W$ the energy confinement time can be as large as 1.8×10^4 seconds. Even so, the result serves as a useful reference point for measuring how much reduction occurs in τ_E when classical confinement is replaced by quasilinear transport due to the interchange mode.

5.3.2 Bohm diffusion

As another point of reference we can redo the calculation assuming Bohm rather than classical diffusion. There is no justification for using Bohm diffusion. It simply serves as a second reference point. For Bohm diffusion the only change is to replace the classical value of χ_C with the Bohm value as follows [16].

$$\chi_B = \frac{1}{16}\frac{T}{eB_\theta} \tag{5.21}$$

The modified equation for the temperature reduces to

$$\begin{aligned} &\frac{1}{x}\frac{d}{dx}\left(x^2 T_V \frac{dT_V}{dx}\right) = -\alpha_B \delta(x - x_h) \\ &\alpha_B = 5.1\times 10^3 \frac{P_K I_M}{R_0 r_h n_{\max}} \end{aligned} \tag{5.22}$$

The solution is again easily found and in the limit $1 \ll x_h \ll x_w$ can be written as

$$\begin{aligned} T_V &= \left[2\alpha_B\left(1-\frac{1}{x}\right)\right]^{1/2} && 1 \le x \le x_h \\ T_V &= \left[2\alpha_B x_h\left(\frac{1}{x}-\frac{1}{x_w}\right)\right]^{1/2} && x_h \le x \le x_w \end{aligned} \tag{5.23}$$

For this case the experimental parameters of interest are given by

$$\begin{aligned} \tau_E &= 7.5\times 10^{-2}\left(\frac{R_0 r_w^3 I_M n_{\max}}{P_K}\right)^{1/2} \quad \text{sec} \\ \overline{\beta} &= 1.6\times 10^{-4}\left(\frac{r_w^3 n_{\max} P_K}{R_0 I_M^3}\right)^{1/2} \\ T_{\max} &= 1.0\times 10^2\left(\frac{P_K I_M}{R_0 r_h n_{\max}}\right)^{1/2} \quad \text{eV} \end{aligned} \tag{5.24}$$

For the LDX parameters given in Table 1 we find that $\tau_E = 3.4\times10^{-2}$ seconds, $\overline{\beta} = 3.4\times10^{-3}$, and $T_{\max} = 1.4$ keV. As expected, Bohm diffusion leads to a large reduction in confinement as compared to classical transport. Note also that the scaling with the applied power P_K is qualitatively different. Confinement improves with increasing power for classical transport while degrading with Bohm diffusion.

5.4 Quasilinear transport

With the reference cases established we next turn to the more interesting model that takes into account quasilinear transport due to interchange modes. The configuration of interest is illustrated in Fig. 2.

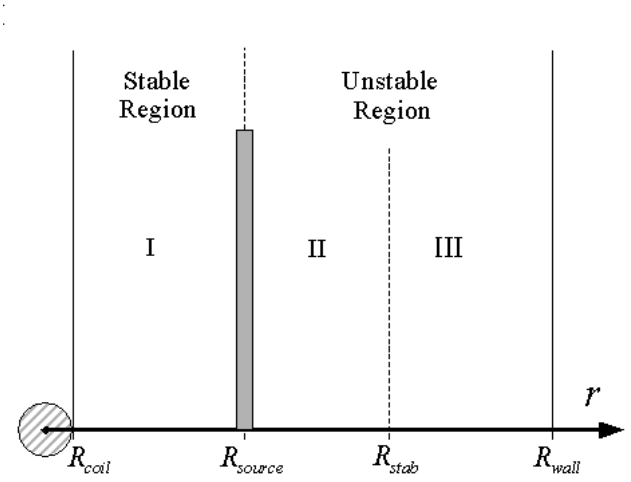

Figure 5-2 Regions of different stability properties

Note that from a mathematical point of view this is a three, possibly four, region problem. We now solve the problem region by region, starting from the levitation coil and working our way out to the surrounding wall. In the first region near the coil, $r_c < r < r_h$, we

assume classical transport and as for the reference cases we require $T(r_c) = 0$ and $dn(r_c)/dr = 0$.

As before, the solution to the particle diffusion equation satisfying the boundary condition at $r = r_c$ implies that the density is uniform across the region.

$$n_1(x) = n_{\max} \qquad 1 < x < x_h \tag{5.25}$$

Here $n_{\max}$ = const. is the maximum value of the density across the entire profile. Its value in LDX is usually determined by the accessibility requirement associated with electron cyclotron heating, $\omega_{pe}^2 \le \omega_{ce}^2$. At the limit, this condition can be expressed as

$$n_{\max} = \frac{\varepsilon_0 B_\theta^2(r_h)}{m_e} = 3.9\frac{I_M^2}{r_h^2} \qquad 10^{17} m^{-3} \tag{5.26}$$

The temperature in region 1 satisfies the classical diffusion equation:

$$\frac{1}{x}\frac{d}{dx}\left(\frac{x^3}{T_V^{1/2}}\frac{dT_V}{dx}\right) = -\alpha_C \delta(x - x_h) \tag{5.27}$$

where α_C is given in Eq. (5.18). The solutions satisfying the boundary at $r = r_c$ is given by

$$T_1(x) = \left[\frac{\alpha_C x_h}{4}\lambda\left(1 - \frac{1}{x^2}\right)\right]^2 \qquad \text{eV} \qquad 1 \le x \le x_h \tag{5.28}$$

In this expression λ is an as yet undetermined positive, dimensionless, free integration constant. Its value is ultimately found by matching onto the quasilinear solutions.

The second region, $r_h < r < r_s$, between the heating source and the quasilinear region,is also characterized by classical transport. The solution here is connected to the first region by the jump conditions

$$\begin{aligned} [\![n]\!]_{r_h} &= 0, \qquad [\![D_C(dn/dr)]\!]_{r_h=0} = 0 \\ [\![T]\!]_{r_h} &= 0, \qquad [\![n\chi_C(dT/dr)]\!]_{r_h} = -S_0 \end{aligned} \tag{5.29}$$

The solutions for the density and temperature are easily found and can be written as

$$\begin{aligned} n_2(x) &= n_{\max} \\ T_2(x) &= \left[\frac{\alpha_C x_h}{4}\left(\frac{1-\lambda}{x^2} - \frac{1-\lambda x_h^2}{x_h^2}\right)\right]^2 \quad \text{eV} \qquad x_h \le x \le x_s \end{aligned} \tag{5.30}$$

The solution in region 2 is valid as long as the interchange stability condition is not violated[3]. Mathematically, the solution is valid when $K(x) > 0$, where $K(x)$ is the Kadomstev stability function. Specifically, stability requires that

$$K(x) \equiv \frac{2\gamma B_\theta^2}{B_\theta^2 + \mu_0 p} + \frac{r}{p}\frac{dp}{dr} \approx 2\left[\gamma - \frac{2(1-\lambda)x_h^2}{\lambda x_h^2(x^2-1) - (x^2 - x_h^2)}\right] > 0 \tag{5.31}$$

The approximate relation is valid in the low β limit. A detailed analysis of this relation combined with the quasilinear solutions in region 3 indicates that there is a wide range of possibilities for the existence of multiple classical and quasilinear regions in the pressure profile. To simplify the analysis we focus on the regime that is of most interest experimentally, corresponding to modest-to-high heating powers. It is shown shortly that in this regime $\lambda \ll 1$. The analysis is further simplified by the reasonable approximation $x_h^2 \gg 1$ and assuming that $\lambda x_h^2 \sim 1$ for a maximal ordering. Under these conditions we see that instability occurs just past the location of the heating source (i.e. $x \to x_h$) when

$$K(x) \approx 2\left[\gamma - \frac{2}{\lambda x^2}\right] < 0 \qquad x \to x_h \tag{5.32}$$

or

[3] Note that the solution in region 1 automatically satisfies the stability criterion since $dp_1/dr > 0$

$$\lambda x_h^2 < \frac{2}{\gamma} \tag{5.33}$$

Hereafter, we assume the plasma is operating in a regime in which Eq. (5.33) is satisfied. The implication is that region 2 becomes vanishingly thin and the solution for $x > x_h^+$ (i.e. region 3) must satisfy the quasilinear diffusion equations. As shown in the accompanying paper the quasilinear solutions are connected to the classical solutions in region 2 by the following jump conditions.

$$[\![n]\!]_{r_h} = 0, \qquad [\![T]\!]_{r_h} = 0 \tag{5.34}$$

The results of the quasilinear analysis predict that the solutions in region 3 should hover around the marginal stability boundary. Thus, when taking into account the jump conditions we se that these profiles can be written as

$$\begin{aligned} n_3(x) &= n_{\max}\left(\frac{x_h}{x}\right)^2 \\ T_3(x) &= T_{\max}\left(\frac{x_h}{x}\right)^{2(\gamma-1)} \end{aligned} \tag{5.35}$$

where

$$T_{\max} = \left[\left(\frac{\alpha_C x_h \lambda}{4}\right)\left(1-\frac{1}{x_h^2}\right)\right]^2 \approx \left(\frac{\alpha_C x_h \lambda}{4}\right)^2 \qquad \text{eV} \tag{5.36}$$

The region of validity of the region 3 solutions is determined as follows. At any arbitrary point $x > x_h$ we must attempt to connect the region 3 solution to an additional region 4 classical solution and then re-evaluate the interchange stability criterion. If the stability condition is satisfied, then the region 4 solution is the one that must be used. If, on the other hand, the stability criterion is violated for all x in the range $x_h < x < x_w$ then no region 4 solution exists and the quasilinear solution is valid from the heating source out

to the wall. This last situation is the one that is of experimental interest and occurs even for quite modest heating powers.

The next step in the analysis is to explicitly calculate the condition for no region 4 to exist. To do this we assume the opposite. A region 4 solution exists starting at a radius $x = x_s$ with $x_h < x_s < x_w$. In this region the density and temperature would be given by

$$\begin{aligned} n_4(x) &= n_{\max}\left(\frac{x_h}{x_s}\right)^2 = \text{ const.} \\ T_4(x) &= T_w\left[k_0\left(\frac{1}{x^2}-\frac{1}{x_w^2}\right)+1\right]^2 \end{aligned} \tag{5.37}$$

where T_w is the known wall temperature and from the jump condition $[\![T]\!]_{x_s} = 0$ the constant k_0 can be written as

$$k_0 = \left[\left(\frac{T_{\max}}{T_w}\right)^{1/2}\left(\frac{x_h}{x_s}\right)^{\gamma-1} - 1\right]\left(\frac{x_s^2 x_w^2}{x_w^2 - x_s^2}\right) \tag{5.38}$$

The condition for the plasma to be interchange stable in region 4 can be easily evaluated. We find

$$K(x) = 2\left[\gamma - \frac{2k_0 x_w^2}{k_0(x_w^2 - x^2) + x_w^2 x^2}\right] \geq 0 \tag{5.39}$$

The quantity $K(x)$ must be positive over the whole region with equality holding at the transition point: $K(x_s) = 0$.

The next step is to substitute k_0 from Eq. (5.38) into Eq. (5.39) evaluated at $x = x_s$. A short calculation then shows that a stable region 4 can exist only if

$$\left(\frac{T_{\max}}{T_h}\right)^{1/2}\left(\frac{x_h}{x_w}\right)^{\gamma-1} \le \frac{2\xi^{\gamma-1}}{2-\gamma+\gamma\xi^2}$$
$$\xi \equiv \frac{x_s}{x_w} \tag{5.40}$$

Observe that the right hand side of Eq. (5.40) has a maximum when

$$\xi^2 = \frac{(\gamma-1)(2-\gamma)}{\gamma(3-\gamma)} = \frac{1}{10} \tag{5.41}$$

with the numerical value corresponding to $\gamma = 5/3$. It therefore follows that a sufficient condition for there *not* to exist a classical region 4 is that

$$\left(\frac{T_{\max}}{T_w}\right)^{1/2}\left(\frac{x_h}{x_w}\right)^{\gamma-1} > 4\left(\frac{1}{10}\right)^{2/3} \approx 0.86 \tag{5.42}$$

Assuming that Eq. (5.42) is satisfied, we can now investigate the consequences of the quasilinear transport model. The main conclusion is that for all practical purposes the profiles represent a two region solution to the transport problem. The inner region from the coil up to the heating surface has classical transport. The outer region, from the heating region to the wall has quasilinear transport. There is a vanishingly thin classical region just beyond the heating surface up to the quasilinear region but the dimensions of this region are so small as to have no effect on the experimental quantities of interest.

The simplified forms of the profiles are summarized below.

$$\begin{aligned}
&\text{Region 1 } (r_c < r < r_h): \quad n = n_{\max} \qquad T \approx T_{\max}\left[\left(\frac{r_h^2}{r^2}\right)\left(\frac{r^2-r_c^2}{r_h^2-r_c^2}\right)\right]^2 \\
&\text{Region 3 } (r_h < r < r_w): \quad n = n_{\max}\left(\frac{r_h}{r}\right)^2 \qquad T = T_{\max}\left(\frac{r_h}{r}\right)^{2(\gamma-1)}
\end{aligned} \tag{5.43}$$

These profiles are illustrated in Fig. 3. The solutions are characterized by the following properties.

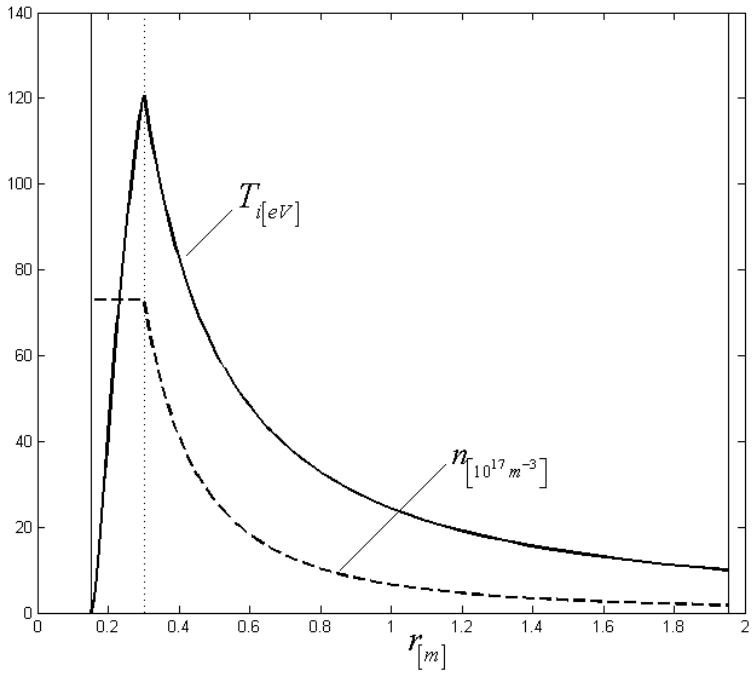

Figure 5-3 The base case in a low beta plasma with the quasilinear diffusion: particle density and ion temperature profiles

(1) The wall density n_w must be adjusted such that the maximum density $n_{\max}$ satisfies the electron cyclotron heating constraint.

$$n_w = n_{\max}\left(\frac{x_h}{x_w}\right)^2 = 3.9\frac{I_M^2}{r_w^2} = 1.73\times 10^{17} m^{-3} \tag{5.44}$$

Here and below all numerical values correspond to the anticipated LDX parameters given in Table 1.

(2) With quasilinear transport the maximum temperature is completely determined by the wall temperature and the geometry. It does not depend directly on the values of the classical transport coefficient, the magnitude of the external heating power, or the coil current.

$$T_{\max} = T_w \left(\frac{r_w}{r_h} \right)^{2(\gamma-1)} = 121 \qquad \text{eV} \tag{5.45}$$

(3) We next check the "large power" assumptions made in the analysis to verify that the power levels involved are indeed reasonable. There are two assumptions to check. First note that the quasilinear analysis implies that the dimensionless parameter λ is given by

$$\begin{aligned} \lambda_{[30kW]} &= \frac{4}{\alpha_C x_h} \left(T_{\max} \right)^{1/2} \\ &= 1.3 \times 10^{-4} \frac{R_0 r_c^2 n_{\max}^2 T_w^{1/2}}{P_K I_M^2} \left(\frac{r_w}{r_h} \right)^{\gamma-1} \\ &= 2.0 \times 10^{-3} \frac{R_0 r_c^2 T_w^{1/2} I_M^2}{P_K r_h^4} \left(\frac{r_w}{r_h} \right)^{\gamma-1} \\ &= 1.4 \times 10^{-3} \end{aligned} \tag{5.46}$$

We see that even if we lower the heating power to only $P_K = 1$ kW the value of λ is quite small: $\lambda_{[1kW]} = 4.0 \times 10^{-2}$. Thus, the inequality assumption given by Eq. (5.33) is well satisfied:

$$\lambda_{[30kW]} \left(\frac{r_h}{r_c} \right)^2 = 5.3 \times 10^{-3} \ll \frac{\gamma}{2} \tag{5.47}$$

The second "large power" assumption associated with Eq. (5.42) is automatically satisfied by virtue of the relationship between $T_{\max}$ and T_w given by Eq. (5.45).

(4) The critical experimental parameter, the energy confinement time, can be easily evaluated from the profiles. We obtain

$$\begin{aligned} \tau_E (\text{sec}) &\approx 9.5 \times 10^{-4} \left(\frac{\gamma}{\gamma - 1} \right) \frac{R_0 r_h^2 n_{\max} T_{\max}}{P_K} \\ &= 9.3 \times 10^{-3} \left(\frac{r_w}{r_h} \right)^{4/3} \frac{R_0 I_M^2 T_w}{P_K} \\ &= 2.4 \times 10^{-2} s \end{aligned} \tag{5.48}$$

Observe that the confinement time scaling relation is qualitatively similar to that of Bohm diffusion in the sense that the same parameters appear in the numerators and denominators of both expressions. However, the quasilinear interchange scaling has a stronger dependence on the parameters. The comparable magnitude of τ_E in the quasilinear case is explained by the favorable behavior of the particle density in the plasma core. The particle density in the Bohm's diffusion remains flat over the entire profile while the quasilinear equations force particle density to peak near the coil. A calculation with a fixed total number of particles in the chamber would result in a noticeably smaller value of τ_E in the quasilinear model.

(5) The last parameter of interest is the volume averaged beta. Another short calculation leads to

$$\begin{aligned}\overline{\beta} &= 2.1\times10^{-6}\left(\frac{\gamma}{\gamma-1}\right)\frac{r_h^2 n_{\max} T_{\max}}{I_M^2} \\ &= 1.9\times10^{-5}\left(\frac{r_w}{r_h}\right)^{4/3} T_w \\ &= 2.4\times10^{-3}\end{aligned} \tag{5.49}$$

Interestingly, when the density is set to its maximum value consistent with electron cyclotron heating, the value of $\overline{\beta}$ is independent of both power and current. It depends primarily on the geometry and the value of the edge temperature. Its value is relatively low thereby providing justification for the low β approximation used in much of the analysis. We can interpret the absence of a P_K dependence as follows. When the heating power is sufficiently large, the enhanced transport due to the interchange mode is so strong that any additional power supplied to the plasma is immediately lost by quasilinear

heat diffusion. In other words increasing the power input does not increase the plasma pressure.

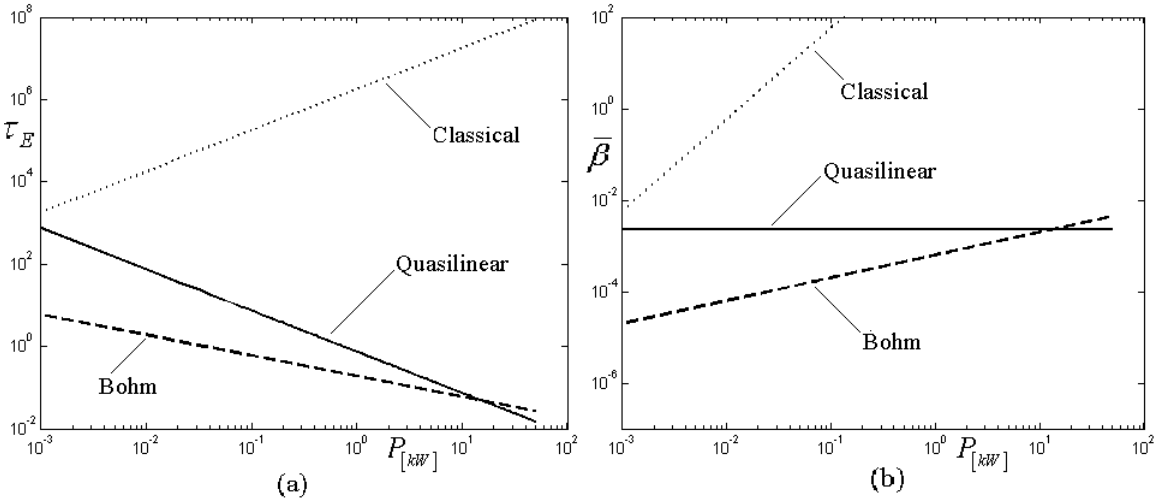

Figure 5-4 Analytical predictions of figures of merits for low beta plasmas with the classical, Bohm's and quasilinear diffusion: (a) Energy confinement time τ_E, (b) Average $\overline{\beta}$

The results of the analysis are conveniently summarized in Fig. 4. Plotted here are curves of τ_E and $\overline{\beta}$ versus P_K. Also shown for comparison are the corresponding curves for classical and Bohm transport. The interchange mode does indeed have a dramatic impact on confinement.

5.5 Numerical results

A more accurate evaluation of the critical plasma scaling relations has been obtained by solving the MHD-Transport model numerically. Three main improvements are introduced with respect to the simple analytic model: (1) finite β is allowed, although this leads to only a small correction, (2) a more realistic distributed heating source is included, and (3) no assumptions are made with respect to the geometric dimensions of the system (i.e. we do not assume $r_c \ll r_h \ll r_w$).

The parameters for the base case correspond to those given in Table 1 and close to the anticipated values for LDX when operation starts with the coil fully levitated [3]. We have also eased the restriction on the maximum particle density in the plasma core, allowing $\omega_{pe}^2 \le 2\omega_{ce}^2$ reflecting the possibility of using the extraordinary wave to heat the plasma. The coil temperature is taken to be $T_c = 0.1\text{eV}$. The localized heating source used is modeled as a shifted Maxwellian that can be written as

$$S_E(r) = \frac{P}{4\pi^{5/2} R_0 r_h \Delta r} \exp\left[-\left(\frac{r - r_h}{\Delta r} \right)^2 \right] \tag{5.50}$$

All parameters have already been specified except for the profile width, which is assumed to be $\Delta r = 3cm$.

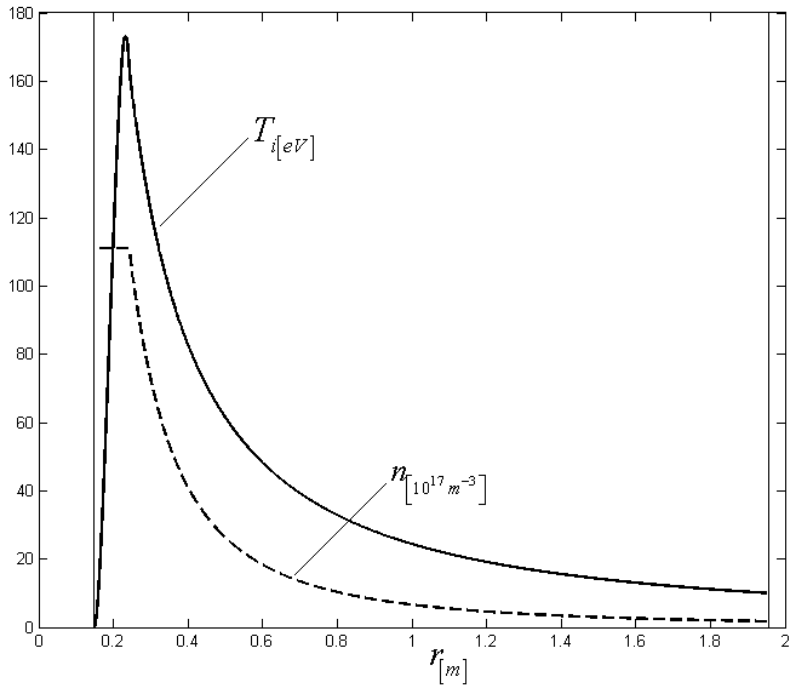

Figure 5-5 The base case: particle density and ion temperature profiles predicted by the numerical model

The numerical solutions are obtained using a straightforward iterative procedure. The density and temperature profiles for the base case are illustrated in Fig. 5. They are quite

similar in appearance to the simple analytic profiles illustrated in Fig. 3. The critical figures of merits for this case are as follows,

$$\begin{aligned} \tau_E &= 2.3\times10^{-2}\, s \\ \overline{\beta} &= 2.3\times10^{-3} \\ T_{\max} &= 172 eV \end{aligned} \tag{5.51}$$

The values obtained from the simple analytic model are quite similar to the numerical values. The numerical model predicts a higher core temperature due to the finite width of the energy source. A strong energy source deposits enough power in the inner region, just beyond the pressure peak, to cause the onset of instability at $r \approx .25m$. This creates a more favorable temperature and higher particle density in the plasma core. These changes, however only marginally influence τ_E and $\overline{\beta}$ due to low volume of the affected plasma.

Variation of the input parameters around the base point leads to a set of "empirical" scaling relations for the critical plasma parameters. These represent one of the main results of the paper and are given by

$$\begin{aligned} \tau_{[\sec]} &= 2.61\times10^{-4}\times P^{-0.96} R_c^{-0.45} R_w^{3.21} R_h^{-1.08} T_c^{0.001} T_w^{0.98} n_w^{0.92} I_c^{0.08} \\ \overline{\beta} &= 1.53\times10^{-6}\times P^{0.04} R_c^{-0.43} R_w^{3.19} R_h^{-1.08} T_c^{0.001} T_w^{0.98} n_w^{0.92} I_c^{-1.91} \\ T_{\max} &= 1.07\times P^{0.05} R_c^{-0.18} R_w^{1.13} R_h^{-1.31} T_c^{0.001} T_w^{0.99} n_w^{-0.09} I_c^{0.07} \end{aligned} \tag{5.52}$$

Similar to the tokamak scaling relation, the "natural" units are used. The power P is expressed in kilowatts (kW), all distances are in meters (m), the temperatures are in electron-volts (eV), a coil current is in mega-Amperes (MA) and the particle density is expressed in the units of $10^{17} m^{-3}$. With the fixed geometrical parameters of the machine, the key drivers of figures of merits are given below:

$$\tau \sim \frac{T_w^{0.98} n_w^{0.92}}{P^{0.96}} R_h^{-1.08}$$
$$\bar{\beta} \sim \frac{T_w^{0.98} n_w^{0.92}}{I^{1.91}} R_h^{-1.08} \qquad (5.53)$$
$$T_{\max} \sim \frac{T_w^{0.98}}{R_h^{1.31}}$$

To test robustness of the scaling relation, a large number of numerical simulations have been carried out by varying the parameters about the base case. In particular, each parameter has been independently varied over the following ranges,

$$\begin{aligned}
&3kW < P < 90kW \\
&1eV < T_w < 50eV \\
&0.01eV < T_c < 1eV \\
&1.7 \cdot 10^{16} < n_{\max} < 1.7 \cdot 10^{18} \\
&0.65MA < I_{coil} < 6.5MA \\
&10cm < r_c < 20cm \\
&r_c + 10cm < r_h < r_c + 60cm \\
&1m < r_w < 3m
\end{aligned} \qquad (5.53)$$

The graph of the calculated τ_E versus the predicted value from the scaling relation given by Eq. (52) is shown in Fig. 6. The empirical fits to the numerical data are accurate to within 8%.

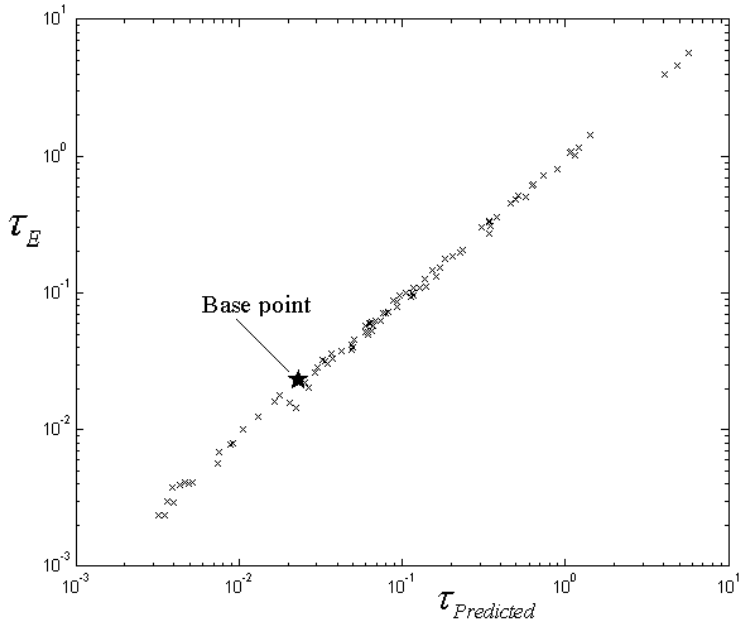

Figure 5-6 Numerically calculated τ_E vs. predicted by the "empirical" scaling relation

Hopefully these results will serve as useful guidelines for the future operation of LDX.

5.6 Conclusions

We have introduced an MHD-Transport model to predict the basic parameters of experimental interest for a hard-core Z-pinch, which is the cylindrical limit of the toroidal dipole concept as manifested in LDX. The model separates the transport essentially into two regions, an inner region near the coil, which is characterized by classical transport, and an outer region beyond the pressure peak characterized by quasilinear transport arising from the interchange mode. The analysis has led to the following conclusions.

1) The interchange mode dominates transport leading to relatively small values of τ_E, $\overline{\beta}$, and $T_{\max}$, comparable to Bohm transport.

2) Beyond a certain heating power ($P \approx 1kW$ for LDX) the model predicts that further increases will not lead to noticeable increases in the particle pressure. The anomalous

transport due to the interchange mode is so strong that all excess energy is immediately lost from the system.

3) Within the model with a localized heating source, there are two strategies for improving performance, besides the obvious one of making the device larger. First, by increasing the coil current, the maximum achievable density consistent with ECH is raised and this leads to improved performance. The second strategy is to raise the edge temperature by improvements in the divertor design. How to do this is somewhat nebulous at present but all performance parameters improve linearly with edge temperature.

4) A more subtle possibility to improve machine performance arises in the toroidal LDX geometry, where the mod-B surfaces cross the field lines and broaden ECRH heating profile. With multiple frequency energy sources, the LDX team can potentially create a tailored low power heating profile that causes the pressure profile to be just below its marginal shape as determined by the simple localized heating source. This causes the energy confinement time to increase to its classical value since by definition the profile is everywhere stable to the interchange mode: there is a large increase in τ_E. Even so the peak temperature and average beta remain unchanged since their values are primarily determined by the edge conditions and the geometry, and not the magnitude of the heating power. Also, note that the system will not experience an inward particle diffusion. Therefore, in order to raise the particle density and the pressure in a plasma core, use should be made of volume particle sources, such as pellet injectors. Lastly, an ultimately successful ignition of the plasma will produce a strong localized heating source, thereby strongly limiting the possibility of external control of the heating profile.

Overall, even with these limitations, the MHD-Transport model predicts that LDX should achieve reasonable performance once the coil is levitated if an edge temperature of $T_w = 10$ eV is achievable.

Chapter 6

6 Summary and Conclusions

This thesis has presented an analysis that theoretically predicts both τ_E and $\overline{\beta}$ for a hard core Z-pinch magnetic configuration. The work has been motivated by a novel experiment jointly operated by Columbia University and MIT – the Levitated Dipole Experiment. LDX is scheduled to start levitated experiments in the spring of 2007. In the levitated phase,the F-coil will be levitated and the coil support losses will be eliminated.

The energy confinement time τ_E and $\overline{\beta}$ will arguably become the most important critical figures of merit for the LDX magnetic configuration. Our goal here has been to make theortical predictions for τ_E and $\overline{\beta}$ based on the quasilinear transport model. To simplify the analysis, we have studied a hard core Z-pinch magnetic configuration, which can be considered to be the large aspect ratio approximation to LDX. We have proposed a self-consistent model of the plasma dividing the plasma into two distinctive regions. A purely classical transport model was used in the interchange stable region of the plasma. For the interchange mode unstable region we have developed a new quasilinear MHD transport model. Analytical and numerical calculations led to explicit scaling relations for τ_E and β which can be tested in future LDX experiments.

In Chapter 3 we have analyzed the impact of axial flows on the stability of an interchange mode. The axial flow is a hard core Z-pinch equivalent of the LDX toroidal flows expected to develop due to the natural electrostatic bias of the floating coil or an non-ambipolar transport in the plasma core. Specifically, the goal has been to learn whether the axial flow improves, is neutral or worsen the stability of the interchange

mode. The flow destroys the self-adjointness of the mathematical problem and the solution of the full eigenmode equation is required to determine the stability boundary. Clearly, the solution of the full eigenmode equation with an arbitrary flow velocity profile can be found only numerically.

To generate intuition, we have considered a slab geometry approximation and analytically derived stability criteria for several idealized velocity profiles. It was shown that there is no straightforward answer to the question of the effect of sheared flow on plasma stabilization. The velocity shear inhibits the formation of interchange perturbations and improves stability although specific velocity profiles can also excite the Kelvin-Helmholtz instability and lead to plasma destabilization.

This intuition was tested with numerical calculations in cylindrical geometry. It was found that flow shear decreases the growth rate of highly unstable perturbations, confirming earlier findings of several other authors. The numerical results of marginal stability calculations supported the analytical slab results, though the changes were more modest than in slab geometry.

It was shown that substantial changes to the marginal stability boundary could be produced only by supersonic flows with the specific flow profile peaking close to pressure maximum. Since the expected LDX flows are subsonic, peaking in the outer portion of the plasma, it was concluded that the effect of flow on the stability of the LDX plasma would be small and therefore could be neglected in all subsequent analyses.

Chapter 4 presents the derivation of the quasilinear MHD transport model, an interesting new contribution to plasma physics research. The violation of the MHD stability boundary leads to a fast growth of the unstable perturbations. A full numerical simulation of the MHD instabilities often requires significant computational recourses

since the instability processes happens on the sound speed time scale. The calculations presented in this chapter analytically demonstrated that the excitation of the MHD perturbations lead to additional transport of energy and particles. The transport starts with the linear growth of the perturbations and is evident in the quasilinear approximation.

The quasilinear diffusion transport equations were analytically derived for the interchange mode in a hard core Z-pinch. Assuming that short wavelength perturbations dominate, the equations were also generalized to a generic toroidal geometry. It was found that the quasilinear transport relaxed a weakly unstable pressure profile back to marginal stability and forced the particle density to be inversely proportional to $\oint d\ell / B$.

The transport equations have a form of the diffusion equations with the diffusion coefficient $D_q = \sum_{\mathrm{mod}\, i} \Gamma_i \left|\xi_r\right|_i^2$, where Γ_i is the growthrate of the i-mode. While the quasilinear approach does not permit explicit calculations of the diffusion coefficient without non-linear numerical simulations, it does point to several important conclusions:

1. If excited, the quasilinear and non-linear transport involve modes growing on the sound speed time scale
2. The microturbulence plays the decisive role in the quasilinear transport since the short wavelength perturbations have the largest growth rate, thus defining the diffusion coefficient and imposing the strictest time-constraint for the quasilinear approximation to be valid.

Quasilinear diffusion transports away all excess energy in the plasma core and restores the profiles back to marginally stablility without macroscopic motion of the plasma. That mechanism should prevent plasma disruptions and creates a “soft-landing” for the profile whose form is limited by the hard MHD stability constraint.

The nonlinear numerical simulations of a plasma in a hard core Z-pinch geometry did not convincingly support or rule out the importance of quasilinear transport. We conjecture that any numerical code is inherently handicapped when trying to model the microturbulent transport because of the finite numerical grid size and the need for a substantial numerical viscosity. These features impose a limit on the shortest allowable wavelength of the perturbations. Thus, any numerical code is able to model only the long wavelength part of the microturbulence, the part that by definition does not contain much of the quasilinear transport.

Even so, quasilinear transport was clearly observed for a low power energy source, but the overall transport was still dominated by classical effects. For a high power source non-linear transport becomes dominant, although as stated the quasilinear effects may be numerically suppressed. At present this is an unresolved issue.

The simulations, however, did show that non-linear transport leads to the identical predictions as the quasilinear theory: the pressure profile is clamped at close to the critical gradient imposed by MHD stability criterion and particle density scales as $n \sim \left[\oint d\ell / B\right]^{-1}$ profile. Together with the analytically derived quasilinear transport equations, the non-linear simulations demonstrate that the LDX should be safeguarded against disruptions regardless of the exact transport mechanism. It is not clear which of the two transport mechanisms will dominate a given plasma. It might be argued that the quasilinear transport mechanism is the more desirable one due to absence of macroscopic motions of the plasma.

A further point worth noting is that the interchange instability imposes a “soft limit” on the maximum achievable pressure profile and dictates the density profile in the unstable region. Absent the danger of disruptions, the LDX should be able to operate with

a high power heating source to achieve the maximum core temperature and plasma pressure. That condition puts an emphasis on the energy confinement time of the LDX magnetic configuration. To be considered a viable fusion concept, the magnetic configuration should satisfy Lawson parameter, which depends on the temperature in the plasma and the energy confinement time τ_E. The calculation of τ_E and $\overline{\beta}$ for a high aspect ratio LDX has been presented in Chapter 5.

The model makes the optimistic assumption that transport is purely classical in the region of the profile that is MHD stable against interchange modes. In the interchange-unstable region use is made of the quasi-linear calculation described in the chapter 4. Analytic and numerical calculations lead to explicit scaling relations for τ_E and β. It is found that the scaling relations are accurate over a wide range of values of the experimentally controlled parameters and geometrical machine constants. The explicit scaling relations for τ_E and β plus the model used in calculations constitute some of the main new results of the thesis.

The scaling relations show reasonably good performance of the large aspect ratio LDX at the expected experimental parameters with particular emphasis on achieving a high edge temperature greater than $10\ eV$. The predictions should be further improved by the finite aspect ratio in the real experiment. On the other side, the quasilinear diffusion model raises the question of the effective use of the input power and the sustainability of ECRH heating. The model predicts that most of the power above 1-3kW will not contribute to any increase in the plasma pressure and any excess of energy will be lost by rapid quasilinear transport, degrading the confinement time τ_E. The build up of

density in the plasma core, caused by MHD transport can make the major resonance for the ECRH heating inaccessible to the incoming waves.

We hope that the results will be useful for the LDX experimental team and will help them in identifying ways to improve the machine performance.

7 References

References of Chapter 1

1. J.Kesner, L.Bromberg, D.Garnier and M. Mauel, 17th IAEA Conference of Plasma Physics and Controlled Nuclear Fusion, Yokohama, Japan 1998, (IAEA Vienna 1999) paper IAEA-F1-CN-69/ICP/09
2. J. Wesson "*Tokomaks*", pp. 392-408, second edition Clarendon press, Oxford (1997).
3. V.P. Pastukhov and N.V.Chudin, Plasma Physics Reports, **27** #11, 907 (2001)
4. V.Makhnin *et. al*., Phys. Plasmas **12**, 042312 (2005)

References of Chapter 2

1. A. Hasegawa, Comm Pl Phys & Cont Fus, **1**, (1987) 147.
2. A. Hasegawa, L. Chen and M. Mauel, Nuclear Fus. **30**, (1990) 2405.
3. A. Hasegawa, L. Chen, M. Mauel, H. Warren, S. Murakami, Fusion Technology **22** (1992) 27.
4. J. Kesner, D.T. Garnier, A. Hansen, M. Mauel, L. Bromberg, Nuclear Fusion **44** (2004) 193.
5. J. Dawson, Private communication in E. Teller, A. Glass, T.K. Fowler et al., Fusion Technology **22**, (1992) 82.
6. Smith, B., et. al. Design, Fabrication and Test of the React and Wind, Nb3Sn, LDX Floating Coil, Applied Superconductivity Conference, Virginia Beach, VA, September, 2000, IEEE Transactions on Applied Superconductivity, March 2001, Vol. 11, No 1.

7. A. Zhukovsky, D.T. Garnier, A. Radovinsky, Thermal Performance of the LDX Floating Coil, Cryogenic Engineering Conference 2005, Keystone, Colorado, August 29 - September 2, 2005, (2005) paper R1-M
8. A. Hansen, D. Garnier, J. Kesner, M. Mauel and A. Ram, "ECRH in the Levitated Dipole Experiment", AIP Conf. Proc. **595**, 362 (2001)
9. A. Hansen *et al*., "Varying ECRH to Modify Confinement in LDX", poster P1.031, ICC Meeting, University of Texas, Austin, February 13-16 (2006)
10. "A Whitepaper" reference
11. D. Garnier, J. Kesner and M. Mauel, Phys. Plasmas **6**, 3431 (1999)
12. J. Kesner, J. Phys. Plasmas, **7** (2000) 3837.
13. J. Kesner and R. Hastie, Phys. Plasmas **9**, 395 (2002)
14. J. Kesner, Phys. Plasmas **4** (1997) 419
15. S. Krasheninniov, P. Catto and R. Hazeltine, Phys. Rev. Lett. **82**, 2689 (1999)
16. S. Krasheninniov, P. Catto and R. Hazeltine, Phys. Plasmas **7**, 1831 (2000)
17. A. Simakov, P. Catto, S. Krasheninniov and J. Ramos, Phys. Plasmas **7**, 2526 (2000)
18. A. Simakov, P. Catto and R. Hastie, Phys. Plasmas **8**, 4414 (2001)
19. A. Simakov, P. Catto, J. Ramos and R. Hastie, Phys. Plasmas **9**, 4985 (2002)
20. V.P. Pastukhov and N.V.Chudin, Plasma Physics Reports, **27** #11, 907 (2001)
21. J. Kesner, Phys. Plasmas **10**, 908 (2003)
22. N. Krasheninnikova and P. Catto, Phys. Plasmas **13**, 052503 (2006)
23. D. Garnier, *et. al*., Phys. Plasmas **13**, 056111 (2006)

References of Chapter 3

1. J. Kesner, L. Bromberg, D. Garnier, M. Mauel, 17th IAEA Conference of Plasma Physics and Controlled Nuclear Fusion, Yokohama, Japan 1998, (IAEA, Vienna 1999), paper IAEA-F1-CN-69/ICP/09
2. D. Garnier, A. Hansen, J. Kesner *et al.*, *"The Superconducting Levitated Dipole Experiment (LDX)",* 15th Intl. Toki Conference, Toki, Japan 12/2006, submitted to Fusion Engineering and Design (2006).
3. Kadomtsev B. B., in *"Reviews of Plasma Physics"*, edited by M. A. Leontovich, Consultants Bureau, New York, Vol. II. (1966)
4. I.B. Bernstein, E. Frieman, M. Kruskal and R. Kulsrud, Proc. Roy. Soc. A**, 244**, 17, (1958)
5. J. Taylor, J. Nuclear Energy, Pt. C, **4**, 406 (1962)
6. J.P. Freidberg and J.A. Wesson, Phys. Fluids **13**, 1117, (1970)
7. A. Bondeson, R. Iacono and A. Bhattacharjee, Phys. Fluids, **30**, 2167, (1987)
8. E. Hameri, Ph.D. thesis, New York University, 1976
9. E. Hameri and P. Laurence, J. Math. Phys. **25**, 396 (1984)
10. D. Garnier, J. Kesner and M. Mauel, Phys. Plasmas, **6**, 3431, (1999)
11. A.N. Simakov, P. Catto, J. Ramos and R. Hastie, Phys. Plasmas, **9**, 4985 (2002).
12. V. Sotnikov, I. Paraschiv, V. Makhnin, B. Bauer, J. Leboeuf and J. Dawson, Phys. Plasmas, **9,** 913, (2002)
13. Y. Zhang and N. Ding, Phys. Plasmas **13**, (2006)
14. S. DeSouza-Machado, A. Hassam and R. Sina, Phys. Plasmas, **7,** 4632, (2000)
15. H. Kuo, Phys. of Fluids, **6**, 195 (1963)
16. P. Guzdar, P. Satyanarayana, J. Huba and S. Ossakow, Geophys. Research Let., **9**, 547 (1982)

17. A. Hassam, Phys Fluids B **4**, 485 (1992)

18. A. Hassam, Phys. Plasmas, 3772 (1999)

19. Malagoli, G.Bodo and R. Rosner, The Astronomical Journal, **456**, 708 (1996)

20. F. Brochard, E. Gravier and G. Bonhomme, Phys. Plasmas, **12**, 062104 (2005)

21. E. Frieman and M. Rotenberg, Reviews of Modern Physics, **32**, 898 (1960)

22. V.P. Pastukhov and N.V.Chudin, Plasma Physics Reports, **27** #11, 907 (2001)

23. V. P. Pastukhov and N. V. Chudin, 19th IAEA Fusion Energy Conference, Lyon, France 2003, paper IAEA-TH/2-5

References of Chapter 4

1. Kesner, J., Bromberg, L., Garnier, D., Mauel, M., presented at 17th IAEA Conference of Plasma Physics and Controlled Nuclear Fusion, Yokohama, Japan 1998, paper IAEA-F1-CN-69/
2. D.T. Garnier, et al *"The Superconducting Levitated Dipole Experiment (LDX)", 15th Intl Toki Conference*, 12/2006, to be published in Fusion Engineering and Design (2007).
3. D. Garnier, J. Kesner and M. Mauel, Phys. Plasmas, vol. **6**, (1999) pp.3431-3434
4. Simakov A., P. Catto, J. Ramos and R. Hastie, Phys. Plasmas, **9**, 4985 (2002).
5. Simakov A., P. Catto and R. Hastie, Phys. Plasmas, **8**, #10, p. 4414 (2001)
6. N. Krasheninnikova and P. Catto, Phys. Plasmas, **13,** 052503 (2006)
7. Glasser A. H. *et al*., Plasma Phys. Controlled Fusion, **41**, A747 (1999)
8. D.Ryutov, B.Cohen, R. Cohen, E. Hooper and C. Sovinec, Phys. Plasmas **12**, 084504 (2005)

9. V.P. Pastukhov and N.V.Chudin, Plasma Physics Reports, Vol. **27**, #11 (2001) pp. 907-921
10. V. P. Pastukhov and N. V. Chudin, 19th IAEA Fusion Energy Conf. Paper IAEA-TH/2-5, Lyon, France, 2003
11. V.Makhnin *et. al*, Phys. Plasmas **12**, 042312 (2005)
12. D. Adler and A. Hassam, Phys. Plasmas, **12**, 062506 (2005)
13. T. H. Stix, "Waves in plasmas", Springer, New-York, (1992), pp. 445-515
14. Kadomtsev B. B., in *"Reviews of Plasma Physics"*, edited by M. A. Leontovich, Consultants Bureau, New York, Vol. II. (1966)
15. P. N. Guzdar, J. F. Drake, D. McCarty, A. Hassam and C. Liu, Phys. Fluids B **5**, 3712 (1993)
16. Yoshizawa A., S. Itoh, K. Itoh and N. Yokoi, Plasma Phys. Cont. Fusion, **43** (2001), R22

References of Chapter 5

1 Kouznetsov, J. Freidberg and J. Kesner, "Quasilinear MHD transport in the axisymmetric closed-field line configurations", submitted to Physics of Plasmas

2 J.Kesner, L.Bromberg, D.Garnier and M. Mauel, 17th IAEA Conference of Plasma Physics and Controlled Nuclear Fusion, Yokohama, Japan 1998, (IAEA Vienna 1999) paper IAEA-F1-CN-69/ICP/09

3 D. T. Garnier *et.al*., Phys. Plasmas **13** (2006) 056111

4 J. Wesson "*Tokomaks*", pp. 392-408, second edition Clarendon press, Oxford (1997).

5 D. Garnier, J. Kesner and M. Mauel, Phys. Plasmas **6**, 3431 (1999)

6 I. Karim, Ph.D. thesis, Massachusetts Institute of Technology (2006)

7 P. Ricci, B. Rogers and W. Dorland, Phys. Rev. Letters, **97**, 245001 (2006)

8 S Krasheninnikov, P. Catto and R. Hazeltine, Phys. Rev. Lett. **82**, 2689 (1999)

9 S Krasheninnikov, P. Catto and R. Hazeltine, Phys. Plasmas **7**, 1831 (2000)

10 L. Guazzotto and J. Freidberg (paper on equilibrium beta limits)

11 V.P. Pastukhov and N.V.Chudin, Plasma Physics Reports, **27** #11, 907 (2001)

12 V. P. Pastukhov and N. V. Chudin, 19th IAEA Fusion Energy Conference, Lyon, France 2003, paper IAEA-TH/2-5

13 S. I. Braginskii, in "*Reviews of plasma Physics*", edited by M.A. Leontovich, New York, Vol I, pp. 213-219 (1965)

14 Kadomtsev B. B., in *"Reviews of Plasma Physics"*, edited by M. A. Leontovich, Consultants Bureau, New York, Vol. II. (1966)

15 A.N. Simakov, P. Catto, J. Ramos and R. Hastie, Phys. Plasmas, **9**, 4985 (2002).

16 F. Chen, "*Introduction to plasma physics and controlled fusion*", p.190, second edition, Springer Science, Vol. I (2006)

8 Appendices

8.1 Appendix A. Constant flow shear model- analytical calculations of the marginal stability

This appendix presents the details of marginal stability calculations for a constant flow shear model. The dispersion relation (3.12) is easily solvable for half-integer parameters ν. The Bessel functions at $\nu = 1/2$ may be represented as a combination of exponentials and algebraic terms

$$\begin{aligned} K_{3/2} &\propto \frac{1}{\sqrt{z}} e^{-z}\left(1+\frac{1}{z}\right) \\ I_{3/2} &\propto \frac{1}{\sqrt{z}}\left[e^{z}\left(1-\frac{1}{z}\right)+e^{-z}\left(1+\frac{1}{z}\right)\right] \end{aligned} \tag{A1}$$

and the dispersion relation is reduced to a quadratic equation. Trivial calculations lead to an explicit form of the growthrate ω:

$$\frac{\omega}{\omega_S} = i\left[\kappa\coth(2\kappa)-\frac{\kappa^2+1}{2}\right]^{1/2}\left(-K_{\min}\right)^{1/2} \tag{A2}$$

where $\kappa = kL$.

The next step is a numerical tracing of the solution to dispersion relation using (A2) as an initial starting point. Namely, the dispersion relation (3.12) is numerically solved for each fixed wavenumber $\kappa = kL$ while the index ν is being gradually decreased. The exact growthrate, given by (A2) serves as a starting guess to ensure that the code locks on the most unstable solution. By tracing the most unstable solution, the index of a Bessel function is gradually decreased until the instability disappears. Our numerical solution shows that as ν decreases towards the value unity (corresponding to $K_{\min}$ increasing

from the negative direction) the region of unstable wave numbers shrinks to zero; that is $k_{\max} \to 0$ as $\nu \to 1$. This behavior is illustrated on Fig.8-1.

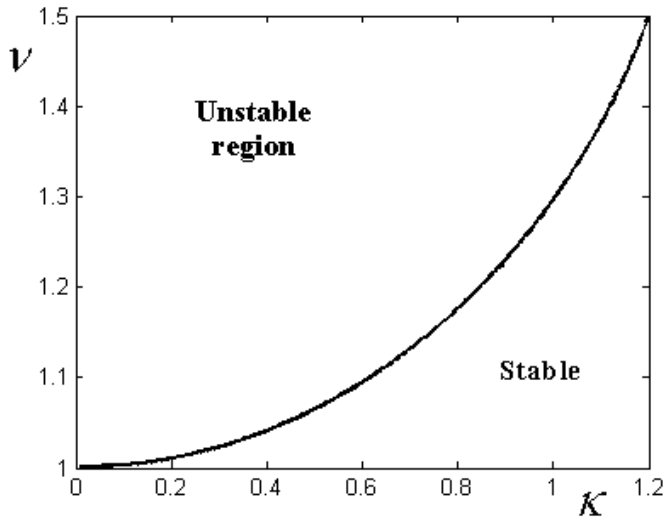

Figure 8-1 Dependence of marginally stable on the wavenumber

The marginal stability boundary can be then found analytically by focusing attention on the behavior of the dispersion relation for small kL. Specifically, we write $\omega = \omega_r + i\omega_i$, expand $\nu = 1 + \delta\nu$, and assume the following ordering scheme:

$$\begin{aligned} &\omega_i / V' \ll kL \ll 1 \\ &\kappa \ll \delta\nu \le \kappa \ll 1 \end{aligned} \tag{A3}$$

Also $\omega_r = 0$ by symmetry. Since $K_\nu = \frac{1}{2}\pi\left[\frac{I_{-\nu} - I_\nu}{\sin(\nu\pi)}\right]$ for all non-integers ν and the convergence to integer index ν is uniform, it is convenient to rewrite the dispersion relation in the following form:

$$\det\begin{bmatrix} I_\nu(z_R); K_\nu(z_R) \\ I_\nu(z_L); K_\nu(z_L) \end{bmatrix} = \det\begin{bmatrix} I_\nu(z_R); I_{-\nu}(z_R) \\ I_\nu(z_L); I_{-\nu}(z_L) \end{bmatrix} = 0 \tag{A4}$$

A small argument expansion of the Bessel functions:

$$I_{+\nu}(z)=\left(\frac{z}{2}\right)^{\nu}\left[1+\frac{z^2}{4(\nu+1)}\right]+O\left(z^{4+\nu}\right)$$
$$I_{-\nu}(z)=\left(\frac{z}{2}\right)^{-\nu}\cdot\frac{1}{\Gamma(1-\nu)}\left[1+\frac{z^2}{4}\frac{\Gamma(1-\nu)}{\Gamma(2-\nu)}\right]+O\left(z^{4-\nu}\right) \quad \text{(A5)}$$

Taking advantage of the well-known mathematical limit $\delta\nu\cdot\Gamma(\delta\nu)\simeq 1$, it is straightforward to show that it is sufficient to consider only the leading term in expansion (A5). The solution to dispersion relation (A4):

$$\frac{\omega}{V'}=-\frac{\delta\nu\kappa}{2}\left[\ln\left(-\kappa-\frac{\omega}{V'}\right)-\ln\left(\kappa-\frac{\omega}{V'}\right)\right] \quad \text{(A6)}$$

An unstable root must have $\mathrm{Im}(\omega)>0$ which happens only for $\delta\nu>0$

$$\frac{\omega}{|V'|}=\frac{i\pi\delta\nu\cdot sign(\kappa)\kappa}{2}=\frac{i\pi\delta\nu|\kappa|}{2} \quad \text{(A7)}$$

Rewriting V' in terms of the Kadomtsev function value and using the definition of $\nu=\sqrt{\frac{1}{4}-\frac{\omega_S^2 K_{\min}}{V'^2}}$, it is easy to find the final form of the growthrate near marginality:

$$\omega=\frac{i\pi}{2}\left(-\frac{K_{\min}}{K''_{\min}}\right)^{1/2}kV'(\nu-1) \quad \text{(A8)}$$

That concludes the proof that $\nu=1$ is the marginal stability point for the constant flow shear model. An analytical proof of a marginal stability point for the no-slip velocity profile is performed analogously.

8.2 Appendix B. Marginal stability in the cylindrical geometry-numerical algorithm

An analysis of the full eigenmode equation in a cylindrical geometry requires numerical solutions. We employed a shooting method to solve the eigenmode equation for a

particular wavenumber k and the velocity profile $V_z(r)$. The code is given eigenfunction value $\psi(r_{wall}) = 0$ at the outer boundary and takes initial guess of a complex eigenfrequency. Then, an absolute value of the eigenfunction on the coil surface is minimized by varying real and imaginary parts of the eigenfrequency. The resulting eigenfunction is checked for absence of nodes to ensure the obtained solution is the most unstable. The algorithm described above works very effectively for low velocities and static plasma. It quickly converges to correct eigenfrequency from a wide of initial guesses. However, as the speed of the background flows is increased, the requirement for initial guess becomes more stringent. One explanation of this fact may be found by qualitatively analyzing a structure of the eigenmode equation in a slab geometry. The solution of an eigenmode equation is a modified Bessel function if Kadomtsev function K is a constant and a Whittaker function for parabolic K. Both Bessel and Whittaker functions oscillate rapidly when their arguments have simultaneously large real and imaginary parts. As the flow speed is increased, the argument $z = kx - \frac{\omega}{V'}$ at the coil has indeed very large real and imaginary parts for any ω except the exact eigenfrequency.

The shooting method, which is trying to minimize the absolute value of the eigenfunction at the coil boundary, may converge to local minimum and will not find correct eigenvalue. Thus, only an initial guess located close to the eigenfrequency value will permit the code to lock on the global minimum and find correct eigenfrequency.

In order to produce the correct initial guess, we had to track the solution as illustrated on Fig. 8-2. For references purposes, the dotted curve represents an analytically derived marginal stability α for a slab geometry.

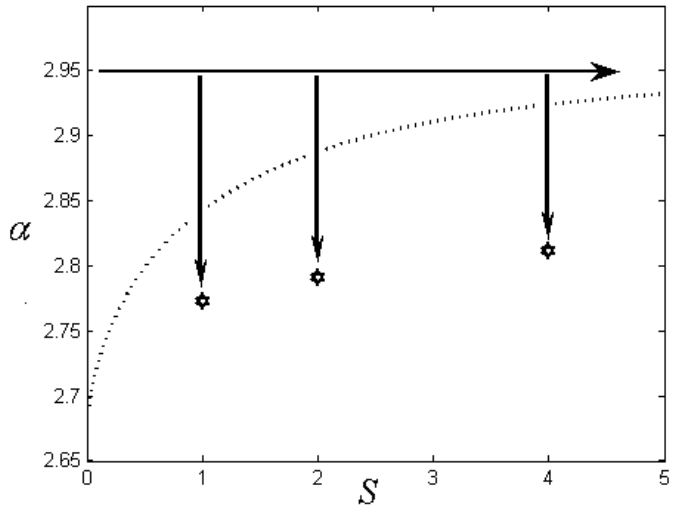

Figure 8-2 Tracking path along the found solutions. The dotted curve represents analytically found marginal stability curve for a slab geometry.

We started the tracking path by determining an eigenfrequency for a static plasma at highly unstable $\alpha = 2.95$ and specific wavenumber k. Then the flow speed was gradually increased. At each step, the eigenfrequency initial guess for a next step was determined by linear extrapolation. The obtained curve of growthrate vs. the Mach number clearly demonstrated that the flow decreases the growth rate of highly unstable perturbations.

To find the marginal stability for a given flow velocity, the pressure parameter α was slowly decreased. Again, the linear extrapolation of the eigenfrequency provided an initial guess for a next step. We were typically able to track the unstable solution up to the level when the growthrate was from 10^{-4} to 10^{-5} of its value at $\alpha = 2.95$. At that stage, the extrapolation was used to define the marginally stable α. The described procedure has been repeated for different values of wavenumber k.

8.3 Appendix C. Derivation of the quasilinear transport equations for a hard-core Z-pinch in the R-Z coordinates

This appendix presents an alternative way to derive quasilinear transport equations in the physical R-Z coordinates of a Z-pinch. The method shown here has an advantage of directly estimating the relative ordering of different terms though it is less transparent than the flux coordinate derivations presented in Chapter 4. We start with the initial quasilinear equation for density:

$$\left\langle \frac{\partial \rho}{\partial t} \right\rangle = -\left\langle \nabla \cdot \sum_{\mathrm{mod}\,es} \left(\rho_1^* \mathbf{v}_1 \right) \right\rangle \tag{C1}$$

where ρ_1 and $\mathbf{v}_1$ are the linearized perturbed density and velocity. Equations for the entropy related function $s = p/\rho^{\gamma-1}$ and magnetic field are easily found by averaging Maxwell and adiabatic equations.

$$\begin{aligned} \left\langle \frac{\partial s}{\partial t} \right\rangle &= \left\langle \nabla \cdot \sum_{\mathrm{mod}\,es} \left(\mathbf{v}_1^* \cdot s \right) \right\rangle \\ \left\langle \frac{\partial \mathbf{B}}{\partial t} \right\rangle &= \left\langle \nabla \times \sum_{\mathrm{mod}\,es} \left(\mathbf{v}_1^* \times \mathbf{B}_1 \right) \right\rangle \end{aligned} \tag{C2}$$

For simplicity the "zero" subscript is hereafter suppressed on all equilibrium quantities. Following the regular MHD approach, all perturbed linearized quantities ρ_1, p_1 and velocity $\mathbf{v}_1$ are rewritten in terms of a displacement vector $\boldsymbol{\xi}$:

$$\begin{aligned} \rho_1 &= -\nabla \cdot \left(\rho \boldsymbol{\xi} \right) \\ p_1 &= -\boldsymbol{\xi} \cdot \nabla p - \gamma p \left(\nabla \cdot \boldsymbol{\xi} \right) \\ s_1 &= -\nabla \cdot \left(s \boldsymbol{\xi} \right) \\ \mathbf{B}_1 &= \nabla \times \boldsymbol{\xi} \times \mathbf{B} \\ \mathbf{v}_1 &= -i\omega \boldsymbol{\xi} \end{aligned} \tag{C3}$$

The system of quasilinear equations (C1-C2) rewritten in the form of displacement vector $\boldsymbol{\xi}$ has the form:

$$\begin{aligned}
\left\langle \frac{\partial \rho}{\partial t} \right\rangle &= \left\langle \nabla \cdot \left(\Gamma \boldsymbol{\xi}^* \nabla \cdot \left(\rho \boldsymbol{\xi} \right) \right) \right\rangle \\
\left\langle \frac{\partial s}{\partial t} \right\rangle &= \left\langle \nabla \cdot \left(\Gamma \boldsymbol{\xi}^* \nabla \cdot \left(s \boldsymbol{\xi} \right) \right) \right\rangle \\
\left\langle \frac{\partial \mathbf{B}}{\partial t} \right\rangle &= \left\langle \nabla \times \left[\Gamma \boldsymbol{\xi}^* \times \nabla \times \left(\boldsymbol{\xi} \times \mathbf{B} \right) \right] \right\rangle
\end{aligned} \tag{C4}$$

We suppressed the sign of summation over unstable modes and introduced a notation for a growthrate of an unstable mode $\Gamma = -i\omega$. Following the usual stability analysis procedure, the components of a displacement vector $\boldsymbol{\xi}$ are expressed in terms of the radial component $\xi = \mathbf{e}_r \cdot \boldsymbol{\xi}$. Straightforward but slightly tedious calculation shows that all three equations in the system (C4) follow the same order pattern:

$$\left\langle \frac{\partial f}{\partial t} \right\rangle \sim \frac{V_p^2}{V_A^2} \left[\left(\left| \xi' \right|^2 - \left| \xi \xi'' \right| \right) + \left| \xi' \right|^2 \cdot O\left(\frac{V_p^2}{V_A^2} \right) \right] + \left| \xi' \xi \right| \cdot O\left(\frac{V_p^2}{V_A^2} \right) + \left| \xi \right|^2 \left(O(1) + O\left(\frac{V_p^2}{V_A^2} \right) \right) \tag{C5}$$

where $V_p = \dfrac{\omega}{k}$ is a plasma phase velocity and $V_A^2 = \dfrac{B^2}{\mu_0 \rho}$ is an Alfven speed. The dash ' denotes radial derivatives. A localized mode means $\left| \xi' \right| \gg \dfrac{\left| \xi \right|}{L}$, where L is a characteristic geometrical size of the system.

To make an equation (C5) transparent and separate the leading term, it is necessary to introduce ordering and evaluate terms $\left| \dfrac{\xi'}{\xi r} \dfrac{V_p}{V_A} \right|^2$. Two specific cases should be considered. The first one deals with highly localized eigenmodes and the other case considers global modes. We will start with a highly localized case, as this case covers the most dangerous short wavelength perturbations.

The localized unstable mode appears near the local minima of the Kadomtsev function $K_p = \left[\frac{rp'}{p} + \frac{2\gamma V_A^2}{\left(V_A^2 + V_S^2\right)} \right]$. Exploiting the fact of high mode localization, it is convenient to approximate Kadomtsev function around a local minimum by parabolic function: $K(r) = K_{\min} + \frac{K''}{2}\left(r - r_{\min}\right)^2$. A violation of the stability criterion $K_{\min} \geq 0$ results in the excitation of an unstable perturbation centered at $r_{\min}$. Analytical solution of the eigenmode equation for parabolic Kadomtsev function is easily found to be Hermitian polinoms[1]. An explicit estimation of a growth rate and radial derivatives shows the following

$$\left|\frac{\xi'}{\xi r}\right|^2 \cdot \left|\frac{V_p}{V_A}\right|^2 \sim \frac{r^2\left|K''\right|}{2e^2\left|K_{\min}\right|} \cdot \frac{4K_{\min}^2}{r_{\min}^2\left|K''\right|}\frac{V_s^2}{V_A^2} = 2\frac{r^2}{r_{\min}^2}e^{-2}\left|K_{\min}\right|\frac{V_s^2}{V_A^2} \qquad \text{(C6)}$$

where $V_S^2 = \frac{\gamma p}{\rho}$ is the sound speed. The low beta plasma assumption (i.e. $\beta \propto \frac{V_S^2}{V_A^2} \ll 1$) would force the following ordering condition for the radial derivatives of the perturbations

$$\left|\frac{\xi'}{\xi r}\frac{V_p}{V_A}\right|^2 \ll 1 \qquad \text{(C7)}$$

However, the ordering condition (C7) holds true for arbitrary β plasmas. Recall that the quasilinear approximation is valid only for weakly unstable plasma profiles (i.e $K_{\min} \ll 1$), which automatically makes the condition (C7) valid for arbitrary β plasmas.

[1] J .P. Freidberg, " Plasma Physics and Fusion Energy", Cambridge University Press (2007)

Naturally, when the displacement vector ξ is not localized in space and approximation of the Kadomtsev function by parabolic function is questionable, the condition (C7) is satisfied automatically.

The conclusion is that the terms proportional to ξ' and ξ'' do not contribute to the quasilinear transport described by Eq. (C4) since these terms are always multiplied by small coefficient $\frac{V_p^2}{V_A^2}$. By neglecting all terms proportional to radial derivatives of ξ $\left|\xi\right|^2$ it is easy to find that

$$\begin{aligned}\nabla\cdot\left(\rho\boldsymbol{\xi}\right) &= 2\frac{\xi\rho}{r}\frac{V_A^2}{\left(V_A^2+V_S^2\right)}+\xi\rho'+f\left(\xi'\right)\\ \nabla\cdot\left(s\boldsymbol{\xi}\right) &= 2\frac{\xi s}{r}\frac{V_A^2}{\left(V_A^2+V_S^2\right)}+\xi s'+f\left(\xi'\right)\end{aligned} \tag{C8}$$

Substituting Eq. (C8) into (C4) and retaining only the leading terms (i.e. proportional to $\left|\xi\right|^2$), it is straightforward to calculate the final form of the quasilinear transport equations:

$$\begin{aligned}\left\langle\frac{\partial n}{\partial t}\right\rangle &= \frac{1}{r}\frac{\partial}{\partial r}\left[\sum_{k=0}^{\infty}\Gamma\frac{\left|\xi\right|^2}{r}\left[\frac{\partial}{\partial r}\left(nr^2\right)-2\frac{V_S^2}{\left(V_A^2+V_S^2\right)}nr\right]\right]\\ \left\langle\frac{\partial s}{\partial t}\right\rangle &= \frac{1}{r}\frac{\partial}{\partial r}\left[\sum_{k=0}^{\infty}\Gamma\frac{\left|\xi\right|^2}{r}\left[\frac{\partial}{\partial r}\left(sr^2\right)-2\frac{V_S^2}{\left(V_A^2+V_S^2\right)}ns\right]\right]\\ \left\langle\frac{\partial B_0}{\partial t}\right\rangle &= -\vec{e}_\theta\sum_{k=0}^{\infty}\Gamma\left[\frac{\left|\xi\right|^2}{r}\left(\frac{3V_A^2+V_S^2}{V_A^2+V_S^2}\right)+\xi^*\frac{\partial}{\partial r}\xi\right]\left(\frac{\left(rB\right)'}{r}-\frac{B}{r}\frac{2V_S^2}{V_A^2+V_S^2}\right)\end{aligned} \tag{C9}$$

Equation (C9) may be rewritten in a form that closely shows a diffusion nature of the quasilinear transport by introducing a quasilinear "diffusion" coefficient $D_Q=\sum_{k=0}^{\infty}\Gamma\left|\xi\right|^2$ and several profile functions:

$$K_n(r) = \frac{n'r}{n} + \frac{2V_A^2}{\left(V_A^2 + V_S^2\right)}$$
$$K_p(r) = \frac{rp'}{p} + \frac{2\gamma V_A^2}{\left(V_A^2 + V_S^2\right)} \qquad \text{(C10)}$$

Notice, that the condition $K_p = 0$ is the marginal stability criterion, first derived by Kadomtsev[2]. The density condition $K_n = 0$ corresponds to intuitively well-known density profile $n \propto \left[\oint \frac{dl}{B}\right]^{-1}$ that has equal number of particles in each flux tube. Using these notations, the system (C9) may be recast in a compact form:

$$\left\langle \frac{\partial n}{\partial t} \right\rangle = \frac{1}{r}\frac{\partial}{\partial r}\left[D_Q n K_n \right]$$
$$\left\langle \frac{\partial s}{\partial t} \right\rangle = \frac{1}{r}\frac{\partial}{\partial r}\left[D_Q s r \left[K_n - (\gamma - 1) K_n \right] \right] \qquad \text{(C11)}$$
$$\left\langle \frac{\partial B_0}{\partial t} \right\rangle = -\vec{e}_\theta \left[D_Q \left(\frac{3V_A^2 + V_S^2}{V_A^2 + V_S^2} \right) + \Gamma \xi^* \frac{\partial}{\partial r} \xi \right] \left(K_p \frac{V_S^2}{r\gamma V_A^2} \right)$$

The system of equations (C11) governs an evolution of a pressure, density and magnetic field, calculated in a quasilinear approximation. As the MHD instability is excited, the quasilinear transport relaxes pressure profile back to the marginally stable one and works to reorganize density profile to $\rho \propto \left[\oint \frac{dl}{B}\right]^{-1}$ "target" profile. A magnetic field does not have specific "target" profile and the quasilinear diffusion of a magnetic field happens on a slower time scale. The latter statement may be proved by observing that the magnetic

[2] Kadomtsev B. B., in *"Reviews of Plasma Physics"*, edited by M. A. Leontovich, Consultants Bureau, New York, Vol. II. (1966)

diffusion equation has K_p as a profile coefficient, which is small in a weakly unstable plasma.

8.4 Appendix D. Solutions of the self-consistent plasma profiles- numerical algorithm

A task of finding a self-consistent pressure and density profiles in a finite beta plasma requires simultaneous solution of three first order differential equations: the momentum, energy and continuity equations. The resulting self-consistent differential equation for pressure is a third order non-linear differential equation in the MHD unstable region and second order one in the classical region. The stability-instability boundary depends on the pressure profile itself and further complicates calculations.

The high current in the coil and localization of the heat source prompted to use different approach to solve the problem. An iterative approach is used to find self-consistent plasma profiles. At any iteration, the code solved the density equation separately from the energy-momentum pair.

The use was made of the relatively low beta of the plasma, which allowed separation of the density into zero-beta part and finite beta correction. The full density profile equations are given by:

$$\begin{aligned} & n = const && r \le R_{stab} \\ & \frac{r}{n}\frac{dn}{dr} + \frac{2B^2}{B^2 + \mu_0 \gamma p} = 0 && r \ge R_{stab} \end{aligned} \qquad \text{(E1)}$$

where R_{stab} is a stability-instability boundary. The density in the MHD unstable region is represented as $n = n_0 + n_1$, where $n_0 = n_{wall}\left(\frac{r_{wall}}{r}\right)^2$ is a zero $\overline{\beta}$ part and the n_1 is found from the finite $\overline{\beta}$ correction:

$$\frac{\partial}{\partial r}\left(n_1 r^2\right) = \frac{2V_S^2}{V_A^2 + V_S^2} n_0 \qquad \text{(E2)}$$
$$n_1\left(r_{wall}\right) = 0$$

The overall numerical algorithm is the following:

1. When the code is started, the program makes initial guess of the stability-instability boundary $R_{stab} = r_h$. An initial guess for density profile is calculated for zero $\overline{\beta}$ plasma and $R_{stab} = r_h$ using equation (E1). Then the main iteration cycle is started.

----------Start of iteration cycle----------

2. The pressure and temperature profiles are calculated using a shooting method.
    a. Using an initial guess for temperature gradient on the coil surface, the code steps forward to solve energy equation.
    b. On each step the magnetic field is calculated using momentum equation.
    c. On every step code checks for violation of interchange of m=1 mode marginal stability condition. As the marginal stability condition is violated, the code switches to quasilinear transport equations (4.37) and simultaneously calculates magnetic field and pressure profile.
    d. The temperature at the outer wall is checked against known boundary condition. System return to a. until correct temperature gradient is found

3. Given the corrected value for stability-instability boundary R_{stab} and profiles for magnetic field and pressure, the code reevaluates particle density profile.
    a. Zero $\overline{\beta}$ term n_0 is found.
    b. Finite $\overline{\beta}$ correction n_1 is calculated by solving Eq (E2).
4. The code evaluates the difference between the current pressure profile and pressure profile obtained in the previous iteration. If the difference is not small enough, the code returns to step 2.

----------End of iteration cycle----------

5. The last step. The code outputs an energy confinement time τ_E and average $\overline{\beta}$.

The code normally converges within 30-40 iterations. The convergence becomes worse for lower powers of a heating source. As the deposited heating power becomes close to the one a completely MHD stable plasma can tolerate, the convergence suffers. The explanation lies in the fact that the instability creates strong particle density diffusion inward. The higher density increases classical conduction and the code finds the profile to be MHD stable. At the next iteration the particle density is decreased and classical conduction cannot maintain energy balance, thus leading to “discovered” instability region. The theoretical explanation of this phenomenon lies in the assumptions of the quasilinear profiles. The quasilinear profile, used in numerical calculations, assumes dominance of the MHD transport compared to its classical counterpart. At low powers of a heating source the MHD transport and classical conduction becomes comparable and the system of quasilinear profiles (4.36-4.37) is no longer valid.